8-14-2013 12:00 AM

The Continuum Linear Polarization Signature of Classical Be Stars

Robbie J. Halonen
The University of Western Ontario

Supervisor
Dr. Carol E. Jones
The University of Western Ontario

Graduate Program in Astronomy
A thesis submitted in partial fulfillment of the requirements for the degree in Doctor of Philosophy

THE CONTINUUM LINEAR POLARIZATION SIGNATURE OF CLASSICAL BE STARS

(Thesis format: Integrated Article)

by

Robbie Halonen

Graduate Program in Astronomy

A thesis submitted in partial fulfillment
of the requirements for the degree of
Doctor of Philosophy

The School of Graduate and Postdoctoral Studies
The University of Western Ontario
London, Ontario, Canada

Abstract

Classical Be stars are rapidly-rotating, massive stars that exhibit distinct observational characteristics due to the presence of enveloping, equatorial disks of gas. While diligent observation of these objects has established a reliable description of their geometric and kinematic properties, our understanding of classical Be stars remains distressingly limited on the dynamical front. Principally, we lack a satisfactory characterization of the physical process(es) through which the gaseous disks form and dissipate. In order to understand the mechanisms that govern the development of these enigmatic stars, we use computational codes to produce theoretical models of these objects and their environments. We compare the predicted observables to astronomical observations of classical Be stars. By interpreting the results of these comparisons, we can place important constraints on the parameters of the models, and thus determine fundamental properties of the circumstellar disks.

The intrinsic continuum linear polarization signature is a distinguishing feature of classical Be stars. Arising from electron scattering in the non-spherically symmetric distribution of gas, this signature provides a unique means for directly probing the physical and geometric properties of the circumstellar environment. In this thesis, we assess the potential role of polarimetry in investigating the dynamical nature of classical Be star disks. We present our implementation of a Monte Carlo computation of the Stokes intensities using the self-consistent thermal solution of a non-LTE radiative transfer code. We highlight the relative importance of multiple-scattering and disk temperature in predicting the fraction of linearly polarized light emerging from classical Be stars. We also demonstrate that gas metallicity has a minimal effect in the determination of the degree of linear polarization. Finally, by demonstrating that the principal features of the polarimetric signature originate from different parts of the disk, we illustrate how these properties can have an important role in characterizing both the geometric nature and the evolution of the disk. This work establishes a critical understanding of how the continuum linear polarization signature forms and how we can interpret it in the context of the dynamics of classical Be star disks.

Keywords: methods: numerical — polarization — scattering — circumstellar matter — stars: emission-line, Be

Poets say science takes away from the beauty of the stars —
mere globs of gas atoms.
Nothing is ”mere”.
I too can see the stars on a desert night, and feel them.
But do I see less or more?

Richard Feynman
The Feynman Lectures on Physics

Acknowledgements

To my supervisor — thank you for a rewarding collaboration that has culminated in a thesis of which I am tremendously proud. You allowed me to envision a plan for this endeavour on my own and you supported me wholeheartedly with guidance and encouragement. You funded my travel across the world (over 80 000 km!) so that I could learn from our colleagues in the research community and develop a greater appreciation for the scientific value of our work. Your enthusiasm for teaching and your excitement for science fortified those passions in myself. I am indebted to you for bettering me as a scientist, a teacher and an individual.

Thank you, Carol.

To my friends — thank you for being an integral part of this journey. You have been dependable Cylon co-conspirators and worthy rivals for the Iron Throne. You have been ideal golfing partners and terrific euchre adversaries. You have been loyal companions for sushi lunches, movie soirees and camp (not cottage) nights. You have been the people with whom I have debated religion, politics, science and philosophy, and with whom I have shared many of the most unforgettable moments of the last six years. Your friendship has strengthened me in a manner which I can never truly describe and for which I can never be sufficiently appreciative.

Thank you, Lynn, Roger, Michel and Renee.
Thank you, Ryan & Lindsay and Jeffrey & Nicole.
Thank you, Draco, Steph, Megan, Andrea, Alex, Allison, Frances and Jeff.

To my family — thank you for everything. Thank you for your unconditional love. Thank you for your unwavering support. Thank you for your unparalleled inspiration. You have been an indispensable part of my life for nearly twenty-nine years, and you will continue to be for many years to come.

Thank you, Mom & Dad.
Thank you, Tania & Cecil, Jason & Tracy, Stacy & Shelley and Angie.
Thank you, Shanda, Bradley, Ethan and Bryan.

Dedication

To my Mom and Dad
To whom I owe all that I am and all that I have accomplished

Contents

List of Figures

List of Tables

Reference List of Symbols

Symbol	Description (value and/or units)
A	scattering matrix coefficient
E_0	photon packet energy (erg)
E_ν	initial photon packet energy (erg)
$E_{\nu'}$	re-emitted photon packet energy (erg)
G	gravitational constant (6.674×10^8 cm^3 g^{-1} s^{-2})
H	vertical scale height (cm)
I	total Stokes intensity
I_ν	specific intensity (erg cm^{-2} Hz^{-1} s^{-1} sr^{-1})
$I_{\nu,0}$	unattenuated specific intensity (erg cm^{-2} Hz^{-1} s^{-1} sr^{-1})
$I_{\nu,L}$	attenuated specific intensity (erg cm^{-2} Hz^{-1} s^{-1} sr^{-1})
L	photon travel distance (cm)
$\mathbf{L}$	Mueller matrix
L_*	star and circumstellar disk total luminosity (erg s^{-1})
$L_\odot$	Solar luminosity (3.839×10^{33} erg s^{-1})
M_{disk}	total disk mass (g)
M_*	stellar mass (g)
$M_\odot$	Solar mass (1.989×10^{33} g)
N	number of photon packets
P	probability distribution function
P	polarization level or degree of polarization (%)
P_{ij}	scattering matrix elements
P_{max}	probability distribution function maximum
Q, U	linear Stokes intensities
R	radial cylindrical coordinate
$\mathbf{R}$	scattering matrix
R_e	stellar equatorial radius (cm)

R_*	stellar radius (cm)
$R_\odot$	Solar radius (6.957×10^{10} cm)
$\mathbf{S}$	initial Stokes vector
$\mathbf{S}'$	scattered Stokes vector
$T_{\rm eff}$	stellar effective temperature (K)
T_p	density-weighted temperature (K)
T_0	isothermal temperature (K)
V	circular Stokes intensity
V_{disk}	total disk volume ($\rm cm^{-3}$)
Z	vertical cylindrical coordinate
Z_{MW}	metallicity of Milky Way
Z_{SMC}	metallicity of Small Magellanic Cloud
g	radial gravitational acceleration ($\rm cm\ s^{-2}$)
h	Planck constant (6.626×10^{-27} erg s)
i	inclination angle
i_1, i_2	scattering angles
k	Boltzmann constant (1.380×10^{-16} erg $\rm K^{-1}$)
l	photon path length (cm)
m_H	mass of atomic hydrogen (1.674×10^{-24} g)
n	power-law exponent
n_d	particle number volume density ($\rm cm^{-3}$)
n_e	electron number volume density ($\rm cm^{-3}$)
p	normalized polarization level or normalized degree of polarization (%)
p_{BJ}	polarization change across the Balmer Jump (%)
p_{max}	maximum polarization (%)
p_V	polarization in the V-band (%)
q, u	normalized linear Stokes intensities
Δt	simulation time (s)
v	surface-averaged rotational velocity
v_{crit}	critical rotational velocity

v_{eq}	equatorial rotational velocity
v_r	radial velocity of gas in disk
v_ϕ	rotational velocity of gas in disk
x_0	random variate
Θ	angle between the incident and scattered radiation
Φ	azimuthal cylindrical coordinate
β	ellipticity
γ	envelope shape parameter
η	Mueller matrix rotation angle
θ	polar direction angle of the incident photon
θ'	polar direction angle of the scattered photon
θ_*	polar angle on the surface of the star
κ	total opacity
$\kappa_{a,\nu}$	mass absorption coefficient
κ_s	mass scattering coefficient
λ	wavelength (cm)
μ	substitution for $cos\ \theta$ (cosine of the polar angle)
μ_0	cosine of the incident zenith angle
μ_m	mean molecular weight (g)
ν	frequency (s^{-1})
ν'	re-emitted frequency (s^{-1})
ξ	random number sampled uniformly from 0 to 1
ρ	mass density (g cm^{-3})
ρ_0	mass density of the disk at the stellar surface (g cm^{-3})
σ	interaction cross-section (cm^2)
σ_T	Thomson scattering cross-section (6.65×10^{-25} cm^2)
τ	optical depth
τ_{eq}	equatorial optical depth
τ_{es}	electron scattering optical depth

τ_{pp}	plane-parallel slab optical depth
$\overline{\tau_{es}}$	mean electron scattering optical depth
τ_ν	optical depth at frequency ν
ϕ	azimuthal direction angle of the incident photon
ϕ'	azimuthal direction angle of the scattered photon
ϕ_p	azimuthal disk phase parameter
ϕ_*	azimuthal angle on the surface of the star
χ	polarization angle
ψ	cumulative probability distribution function

Reference List of Abbreviations

Abbreviation	Definition
BJ	Balmer Jump
BJV	Balmer Jump vs. V-band
BOA	Bottom of Atmosphere
IR	Infrared
LMC	Large Magellanic Cloud
LPV	Line Profile Variability
LTE	Local Thermodynamic Equilibrium
MM	Millar & Marlborough
MW	Milky Way
PM	Poeckert & Marlborough
SMC	Small Magellanic Cloud
TOA	Top of Atmosphere
UV	Ultraviolet
V/R	Violet-to-Red

Chapter 1

Introduction

1.1 Overview

From the essential molecules that foster life to the complex materials that sustain our expanding civilization, the basic elements that constitute the Earth originated within the life cycle of massive stars. Through the nuclear reactions that fuel them and in the energetic supernovae that characterize their spectacular deaths, massive stars provide the atomic matter from which new celestial bodies are born. Massive stars also sculpt their surroundings through the output of strong winds and intense radiation that shape and ionize the interstellar medium. In the wake of these processes, successive generations of stars emerge, with a few stars massive enough to continue the fundamental cycle. Massive stars are the dynamical and chemical architects of their local environments, and a driving force for galactic evolution in the present Universe.

While observed as no more than points of light in the Earth's night sky, massive stars played a critical role in the formation of our planet and are fundamental to the evolution of the Milky Way. In our pursuit of uncovering the mysteries of the Universe, the study of massive stars presents a valuable tool for comprehending important astrophysical phenomena within our galaxy. Stellar astronomy incorporates observational and theoretical approaches aimed at achieving a comprehensive understanding of all aspects of the lives of stars. As astronomers, we observe stars, we study them, and we model them. We endeavour to perfect our knowledge of these celestial bodies and their pivotal role in the Universe.

Massive stars that exhibit peculiar or variable properties often present unique means for understanding specific aspects of stellar astrophysics. A prime example of these are massive stars whose stellar spectra exhibit emission lines. Multi-wavelength observations of these objects expose a variety of distinct circumstellar environments that characterize different types of massive, emission-line stars. The research in this thesis focuses on one particular type of massive, emission-line star: the classical Be star. These rapidly-rotating B-type stars are surrounded by geometrically-thin, equatorial disks of gas orbiting in Keplerian fashion. While several decades of study have contributed to our understanding of the physical and kinematical nature of these systems, several crucial problems remain in our understanding of the dynamics of their circumstellar environment.

As theorists intent on solving the enigmas associated with classical Be stars, we develop realistic computational models of the circumstellar envelopes that surround these objects. From these models, we can produce synthetic observables that we can compare directly to observations. These models are crucial in deciphering the physical properties of these objects and determining the mechanics involved in their evolution. The knowledge gained from studying emission-line stars can contribute to several branches of astrophysics. For example, classical Be stars may hold important insight into the effects of stellar rotation, pulsation and mass-loss. In addition, the theoretical methods that we develop can have applications to the computation of radiative transfer in other astronomical phenomena.

In this thesis, we establish a framework for using the continuous linear polarization signature of classical Be stars to study the properties of their circumstellar disks. We have developed a new computational routine that implements Monte Carlo methods for simulating the transmission of photons through a circumstellar environment. From this treatment of the radiative transfer problem, we can compute the Stokes intensities that result from the scattering of light and predict the continuous linear polarization properties of classical Be stars. From these predictions, we can study the physical implications of the distinct polarization signature of these objects.

In Chapter 1 of this thesis, we provide the reader with the background that will enable a full appreciation of the research presented in later chapters. In Section 1.2, we present an overview of our current understanding of classical Be stars. Then, in

Section 1.3, we review the basics of polarization and the Stokes parameters. As this thesis is presented in an integrated article format, some of the introductory material presented this chapter is repeated in the introduction of the articles that comprise the third, fourth and fifth chapters.

1.2 Classical Be Stars

In the early half of the nineteenth century, the discovery of dark lines in the solar continuum spectrum and the subsequent chemical analysis and interpretation of these lines initiated the revolutionary field of stellar spectroscopy. These absorption lines represent an essential astronomical tool for identifying the chemical composition of stars and for determining numerous other important stellar properties. In 1866, Padre Angelo Secchi, a pioneer in the era of spectroscopic observations of stars, described his discovery of a peculiarity in a star in the constellation Cassiopeia, γ Cas. He detailed his finding as follows:

> "Dans ma dernière je vous annonçais la grande facilité d'observer les spectres stellaires avec la nouvelle construction de spectroscope que j'ai réussi a combiner. Bientôt j'espère de pouvoir vous envoyer une liste des objets examinés, mais pour le moment je ne pourrais différer davantage à vous signaler une particularité curieuse de l'étoile γ Cassiopée, unique jusqu'à présent. Celle-ci est que pendant que la grande majorité des étoiles blanches montre la raie f très-nette et large, et comme α Lyre, Sirius, etc., γ Cassiopée a à sa place une ligne lumineuse très-belle et bien plus brilliante que tout le reste du spectre. La place de cette raie est, autant que j'en ai pu prendre des mesures, exactement coïncidente avec celle de f ..." (Secchi, 1866)

In essence, Secchi described his discovery as a line brighter than the rest of the spectrum at a wavelength where similar stars exhibit substantial dimming. The astronomer's unexpected detection of a strong, hydrogen emission line in place of an expected absorption line in the spectrum of γ Cas is one of the first reported findings of such a feature and is the first record of a peculiar observation in an object that is now recog-

nized to be a *classical Be star*.

1.2.1 A Working Definition

Collins (1987) provided the following working definition of a *Be star*: "a non-supergiant B star whose spectrum has or had at some time, one or more Balmer lines in emission". This broad phenomenological definition encompasses numerous different types of objects, most of whose origin for line emission can be described in distinct physical terms. For example, non-supergiant emission-line B-type stars include objects such as Herbig Ae/Be stars, Algol-type binaries and σ Ori E type stars. Herbig Ae/Be stars are pre-main sequence stars with natal disks of accreting material. Line emission in these young systems arises from the dusty remnants of the objects' proto-stellar environments. Algol-type systems possess interacting binaries peculiarized by the exchange of mass between the two companions. The line emission materializes in the accretion region produced via the transfer of mass from star to another. Lastly, the class of objects exemplified by the star σ Ori E are chemically peculiar stars associated with strong magnetic fields and fast rotation. The emission lines arise from clouds of circumstellar gas held rigidly in place by a rotating magnetosphere (Townsend et al., 2005). While all of these objects fit Collins' definition of a Be star, they are not considered as part of the group of objects that is the focus of this thesis.

The non-supergiant emission-line B-type stars relevant to this investigation are objects designated as *classical Be stars* to distinguish them from other types of *Be stars*. Differentiating a classical Be star from a Be star requires some analysis of observations, as the defining characteristics of the classical Be phenomenon are ideally described in physical terms. A classical Be star is a rapidly-rotating star that possesses, or has possessed at some point in time, a geometrically thin, equatorial, decretion disk of gas that orbits the star in Keplerian fashion (Porter & Rivinius, 2003). The uncertainty in the status of the disk is crucial; it is understood that the circumstellar material responsible for the emission-line feature in these objects may disappear for a period of time and later reappear.

The classical Be phenomenon affects primarily B-type stars in luminosity classes III through V (Jaschek et al., 1981), although there exist some late O-type and early A-

type stars that satisfy the classification criteria. For some perspective, we summarize the typical attributes of main sequence B-type stars here. Approximately, the masses of these stars range between 3 and 20 $M_\odot$ while their radii range between 2.5 and 8 $R_\odot$ (Cox, 2000). Their effective temperatures range between 1×10^4 and 3×10^4 K. The characteristic spectra of B-type stars feature principally absorption lines of neutral helium (particularly in early B-type stars) and hydrogen (particularly in late B-type stars).

1.2.2 Stellar Rotation

Any discussion on classical Be stars is incomplete without consideration of stellar rotation. That these objects possess high projected rotational velocities has long been established (Struve, 1931). However, the exact distribution of the stellar rotational velocities remains unsettled, underlying a question of crucial importance: how close to the critical limit do classical Be stars rotate? The critical rotational velocity, v_{crit}, is the velocity at which the forces on the rotating stellar gas are balanced, that is to say when the inward gravitational force is equal to the outward centrifugal force. For a star of equatorial radius R_e and mass M_*,

$$v_{crit} = \sqrt{\frac{GM_*}{R_e}}. \tag{1.1}$$

As the rotational velocity of the gas is greatest at the stellar equator, the measure of how close the star is rotating with respect to the critical limit is expressed as the ratio of the equatorial rotational velocity to the critical rotation velocity, or v_{eq}/v_{crit}.

Rotational velocities are typically obtained via measurement of Doppler broadening in photospheric absorption lines. The line-width velocity measurements are recorded as $v\sin i$ values, where v is the surface-averaged rotational velocity of the star and i is the angle of inclination of the star's rotational axis with respect to the observer's line-of-sight. Obtaining a distribution of rotational velocities from measured $v\sin i$ values is problematic because of the need to disentangle the rotational velocity from the inclination angle. Statistical methods can be used for a large number of observed objects. For classical Be stars, such studies suggest that v_{eq}/v_{crit} ranges between 0.5 and 0.8 (Slettebak, 1982; Porter, 1996; Yudin, 2001), with the ratio increasing

for later spectral types. While this estimate of the value of v_{eq}/v_{crit} for classical Be stars exceeds the mean value for normal B-type stars, it is substantially lower than the near-critical expectation of $v_{eq}/v_{crit} \geq 0.95$.

However, the method for determining rotational velocities from broadening in photospheric absorption lines is not without flaws, especially for rapidly-rotating objects (Stoeckley, 1968). One problem with the method is that it assumes that the observed star is perfectly spherical. However, the shape of a rapidly-rotating star is distorted because of the increase in the centrifugal force at the stellar equator. The radius of the object is larger at the equator than it is at the poles (i.e. its shape is that of an oblate spheroid). As such, a rapidly-rotating star is subject to the effects of gravity darkening (Zeipel, 1924; Collins, 1963). The effective gravity acting on the gas at the equator is reduced, as are the local surface temperature and brightness consequentially. Hence, the region of the stellar surface where the rotation is greatest has weaker emission than at the poles, and is weighted less strongly in the absorption profiles, resulting in narrower spectral lines (Collins & Truax, 1995). Townsend et al. (2004) showed that, for rapidly-rotating stars, the widths of absorption lines eventually become insensitive to further increases in rotation. Hence, owing to gravitational darkening effects, the measured $v\sin i$ values for classical Be stars may systematically underestimate the actual projected equatorial velocities of these objects.

The claim that the rotational velocities of classical Be stars are underestimated has tremendous implications for theories concerning the formation of the circumstellar disks. The notion that rotation plays a pivotal role in the mass-loss processes from which the circumstellar gas originates arises regularly in discussions of the Be phenomenon. However, if rotational velocities are well below the critical value, many processes for ejecting photospheric matter into orbit must be deemed nonviable (Owocki, 2006). We will return to this point in Section 1.2.5 when we outline the possible mechanisms for generating a circumstellar disk.

1.2.3 Observational Characteristics

The observational features of classical Be stars reflect the nature of their circumstellar environment. In this section, we discuss the characteristics exhibited by a prototypical

classical Be star and the physical properties that are inferred from these features. We note that these features are those that characterize stars in their active Be phase. As previously mentioned, the distinguishing observational features of classical Be stars are often variable. This variability can usually be characterized on multiple timescales. Long-term and gradual variations that exist on timescales of weeks to years suggest global evolution of the gaseous disk, while more rapid variability, on timescales of minutes to days, suggest photospheric effects. Stars for which the circumstellar disk has disappeared exhibit the standard properties of regular B-type stars.

Emission Lines

The spectrum of a classical Be star exhibits rotationally-broadened photospheric absorption lines with superimposed emission lines which arise from bound-bound transitions in the circumstellar disk. Common atomic species found in emission belong to HI, HeI, FeII, SiII and MgII (Jaschek & Jaschek, 1987) with the most prominent lines being those from the hydrogen series, as illustrated by the representative classical Be star mid-IR spectrum shown in Figure 1.1. The equivalent width and the shape of the line can vary with time, and numerous different line morphologies have been observed (Hanuschik et al., 1996).

One of the determining factors for the shape of the emission-line profile is the inclination of the system. Classical Be stars observed close to pole-on ($i = 0°$) exhibit strong, narrow, single-peaked emission lines. Stars that are inclined with respect to the viewing line-of-sight possess emission lines that are typically double-peaked and symmetric about the centre of the line, with a peak separation in correlating to the observed photospheric absorption line width (Hanuschik, 1996). Classical Be stars in which the central dip between the peaks drops below the continuum flux emerging from stellar photosphere are designated *shell-line Be stars*. These objects have the highest measured photospheric line widths, the highest peak separation and the highest values of $v\sin i$ (Porter & Rivinius, 2003). As such, shell-line Be stars are understood to be objects observed close to edge-on ($i = 90°$). While this explanation for the three broadly-described profile types relies solely on differences in inclination, Silaj et al. (2010) found that the density distribution of the gas can also play an important role in shaping line profiles. Thus, there is some ambiguity to the conventional paradigm.

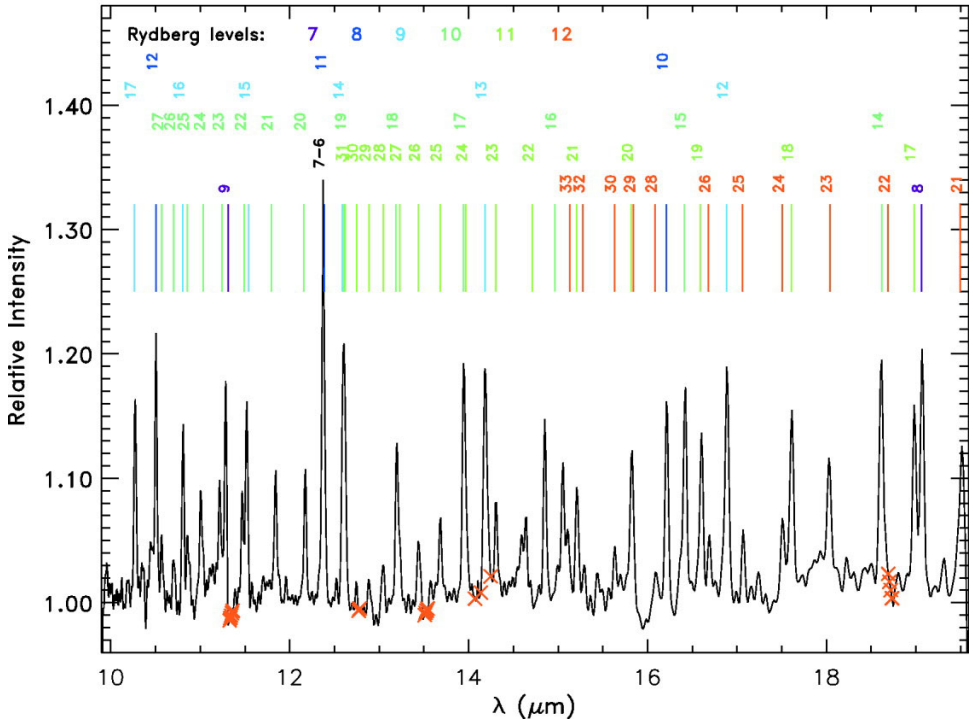

Figure 1.1: Continuum-normalized IR spectrum of the classical Be star γ Cas dominated by hydrogen recombination lines. This spectrum was obtained as part of the wavelength calibration of the short-wavelength, high-resolution module aboard the Spitzer Space Telescope. Image taken from Figure 2 of Houck et al. (2004).

Double-peaked emission lines are commonly observed in classical Be stars. The two components of the profile represent the approaching and the receding parts of the rotating disk; the line emission is Doppler shifted according to the velocity of the emitting gas from either side of the disk. The blue- and red-shifted components are labelled the V (violet) and R (red) components, respectively. The ratio of these two components is designated the violet-to-red (V/R) ratio. While the heights of the V and R components are typically equivalent, the V/R ratio is variable in approximately one-third of all classical Be stars (Hanuschik, 1996). The periods of the quasi-cyclic variability in Hα emission lines range from a few years to roughly one decade (Okazaki, 1997), which is approximately 100 times as long as the rotation period of the gas at the outer radius of the Hα emitting region (Okazaki, 2007). In some classical Be stars, the asymmetry in the V/R ratio appears after a period of symmetry, or disappears after a period of variability (Hanuschik et al., 1996), or changes period abruptly (Mennickent et al., 1997). We discuss the physical implications of the V/R variability in Section

1.2.4.

Linear Polarization

Nearly all classical Be stars emit some fraction of linearly polarized continuous light. Among the earliest reports to indicate a non-zero linear polarization level in a classical Be star were the polarimetric measurements of ζ Tau by Hall & Mikesell (1950) and γ Cas by Behr (1959). From an analysis of the intrinsic polarization distribution for a sample of 495 objects, Yudin (2001) concluded that 95% of classical Be stars exhibit polarization on a level of $0\% < p < 1.5\%$. The polarization signature originates from electron scattering of stellar radiation in the non-spherically symmetric envelope of gas (Coyne & Kruszewski, 1969; Zellner & Serkowski, 1972). The distinct wavelength-dependence of the polarization spectrum can be attributed to the absorption of pre- and post-scattered light by hydrogen (Wood et al., 1997). Ghosh et al. (1999) examined the relationship between linear polarization and Hα emission and found a positive correlation in the strength of the two observables. This correlation fits the paradigm of a flattened, circumstellar disk with sufficient gas density for electron scattering and line emission. As the linear polarization signature of classical Be stars is the focus of this thesis, the characteristics of this signature will be discussed in greater detail later in this chapter.

Continuum Excesses

A notable difference in the spectral energy distribution of classical Be stars from regular B-type stars arises in the visual and near-IR and increases towards longer wavelengths. Photometric observations of classical Be stars reveal that these objects emit considerably more continuum radiation in the aforementioned spectral region than is expected from photospheric emission alone. The origin of this excess emission is free-free and free-bound emission from the circumstellar disk (Gehrz et al., 1974). Ashok et al. (1984) found a positive correlation between the excess in infrared emission and strength of Hα emission, a further affirmation of the presence of an emitting envelope of gas.

Non-Radial Pulsations

Short-period line-profile variability (LPV) occurs on timescales of hours to days and has been detected in most early-type classical Be stars (Rivinius et al., 2003). These spectroscopic variations are exhibited as rapidly-changing bumps or dips travelling through spectral line profiles. While these variations have been attributed speculatively to stellar spots (Balona, 1990) and corotating clouds (Balona, 1995), the evidence of multiperiodicity in the LPV lends conclusive support to the association of the feature with non-radial pulsations (Rivinius et al., 1998). The general characteristics of non-radial pulsations in classical Be stars are described by Kogure & Leung (2007) as follows: (1) the oscillation period varies from 0.1 to 3 days, (2) the velocity amplitudes range from 3 to 20 $km\ s^{-1}$, (3) the amplitude of radial motion varies within $\pm$ 0.02 stellar radii, and (4) the local surface temperatures due to the pulsations differ by $\pm$ 2000 to 3000 K. Rivinius et al. (2003) showed that the LPV in at least 16 classical Be stars is well-explained by non-radial pulsations with modes $l = m = 2$. There is sufficient evidence to suggest that non-radial pulsations and the mechanism responsible for the classical Be phenomenon may be causally related. The apparent lack of similar observations in late-type stars either contradicts such a correlation or indicates that the disk formation process is different in early- and late-type classical Be stars (Rivinius et al., 2003).

1.2.4 Circumstellar Properties

We now expand on the physical description of the circumstellar environment from which the distinguishing observational properties arise.

Geometric Properties

The material enveloping classical Be stars constitutes two distinct components. The first component, a low-density, high-velocity wind emanating from the polar regions of the stellar surface, is well described by the standard line-driven wind theory (Castor et al., 1975; Abbott, 1982) that is applied to normal B-type stars (Slettebak, 1994). Physically characterizing the second component has been more difficult. However, the geometry of this circumstellar gas has become clearer over the past two decades,

beginning with confirmation of the spatial emission distribution by modern interferometric studies. Using radio interferometry, Dougherty & Taylor (1992) showed that the classical Be star ψ Per is surrounded by a flattened, disk-like geometrical distribution of the gas with the radial extent of the emitting region approximately 400 times larger than the radius of the star. Quirrenbach et al. (1994), Stee et al. (1995) and Tycner et al. (2004), among others, confirmed this description of the emitting region for other objects using optical interferometry. Furthermore, Quirrenbach et al. (1997) showed that the observed polarization position angle in several stars is oriented perpendicular to the interferometric major axis of the envelope. As the polarization position angle represents the average orientation of the vibrations of the incident polarized light, it lies perpendicular to the dominant scattering plane. The orthogonality of the polarization position angle to the interferometric major axis of the disk further attests to a flattened geometry for the emitting medium.

With the shape of the circumstellar gas established, we now address the geometric thickness of the disk. The opening angle of the disk provides a measure of the vertical height of the gas above and below the equatorial midplane. Analysis of the interferometric and spectropolarimetric observations of Quirrenbach et al. (1997) establish an upper limit of 20°, while statistical methods estimate the average opening angle around 5° (Porter, 1996) and 13° (Hanuschik, 1996). Hanuschik proposed that the opening angle increases with distance from the star (i.e. the disk flares outward). Therefore, the opening angle determinations are far from homogeneous because the size of the emitting region, and thus the opening angle of the disk, depends on the wavelength of observation used in the analysis. Given this consideration, the opening angle determinations strongly suggest that the disks are geometrically-thin (Porter & Rivinius, 2003).

Kinematic Properties

The velocity structure of the gas is a fundamental property which characterizes the physical nature of the equatorial disk to a considerable degree. As will be underscored in Section 1.2.5, the kinematic description of the disk is critical in the development of models of disk formation. In general, the rotational velocity of the gas should follow

one of three radial dependencies:

$$v_\phi(r) \propto \begin{cases} r^{-1} & \text{for angular momentum conserving outflow,} \\ r & \text{for rigid rotation,} \\ r^{-1/2} & \text{for Keplerian rotation.} \end{cases} \tag{1.2}$$

Each of these three cases would have important implications for the nature circumstellar gas. For example, if $v_\phi(r) \propto r^{-1}$, the outward flow of gas from the stellar surface could be sustained by radiatively-driven stellar winds. If $v_\phi(r) \propto r$, the orbiting gas could be held in place by a rigidly-rotating magnetosphere. And, if $v_\phi(r) \propto r^{-1/2}$, the gas would require continuous injection of angular momentum to maintain a steady Keplerian orbit for an extended period of time.

The velocity structure of the disk can be investigated via Doppler shifts in emission line profiles. As shown above, the azimuthal velocity law in the disk is parametrized by $v_\phi(r) \propto r^{-j}$. Studies attempt to determine the rotational parameter j. Using optically thick lines, Hummel & Vrancken (2000) found that their best-fitting models had an average rotational parameter $j < 0.65$ which is consistent with Keplerian rotation, but not definitive. The radial velocity component, v_r, can be studied from the line profiles of highly-inclined stars. Waters & Marlborough (1994) argued that the lines in Be stars viewed edge-on would exhibit P Cygni profiles, which they do not, if the radial outflow was high. Furthermore, Hanuschik (2000) found no evidence for radial outflow in his examination of optically thin lines in shell stars.

While the evidence from line profiles suggests that the kinematic structure of the disk is dominated by rotation, definitive evidence for a Keplerian disk is provided by spectroastrometry, a technique which can yield spatial information on the velocity structure of the disk with high precision. Modelling the spectroastrometric signature of β CMi, Wheelwright et al. (2012) showed that only a model with Keplerian rotation could satisfy the data. Hence, there is now a general consensus that the disks around classical Be stars are Keplerian.

Dynamical Properties

At present, the only theory that describes the dynamical evolution of the circumstellar gas while satisfying the particular geometric and kinematic requirements that we have just discussed is the outflowing viscous disk model (Lee et al., 1991; Papaloizou et al., 1992; Okazaki, 2001). This model, developed extensively in the context of accretion disks (see, for example, Shakura & Sunyaev, 1973; Pringle, 1981), proposes that gas and angular momentum are injected into the base of the disk at the stellar equator and transported outward under the action of turbulent viscosity (Porter, 1999). In other words, gas viscosity is the mechanism which regulates the angular momentum distribution in the disk such that the centrifugal force balances gravity at all radii (Carciofi, 2011). Of course, the most significant obstacle for the viscous disk model is identifying a process capable of supplying sufficient angular momentum and gas for producing a tenable Keplerian disk.

Notwithstanding the lack of a viable angular momentum input mechanism, viscous decretion disk models have been remarkably successful in satisfying the essential requirements of classical Be stars. On the geometric side, Porter (1999, 2003) confirmed that the viscous disk model can account for the gas density required to produce the observed excess continuum emission. On the kinematic side, Okazaki (2001) demonstrated that an isothermal, viscous decretion disk has a near-Keplerian rotational velocity in the inner region of the disk where the radial velocity is highly-subsonic. The use of non-LTE radiative transfer codes to model classical Be stars have further bolstered the case for viscous outflow. Carciofi et al. (2009) employed a steady-state viscous disk model to perform detailed modelling of the star ζ Tau using a comprehensive set of observations and reported excellent fits of the global, time-averaged properties of the system.

Furthermore, the viscous disk model naturally accommodates the presence of one-armed density oscillations in the disk which can reproduce the previously-discussed V/R variations (Okazaki, 1991). One-armed oscillation modes are the only allowable global modes in Keplerian disks (Kato, 1983). According to Okazaki's application of this theory to dynamical models of circumstellar disks, the perturbation materializes when particles acquire slightly elliptical orbits due to small deviations in the Keplerian velocity distribution. A local density enhancement arises in the circumstellar disk

as the viscosity between individual particles aligns the elliptical orbits. The pattern in the disk precesses, possibly under the influence of a gravitational field containing a quadrupole component created by the non-spherical rotating star (Papaloizou et al., 1992) or due to the radiative force of optically thick lines (Gayley et al., 2001). The direction of the precession is expected to be prograde (Telting et al., 1994). Interferometric observations have yielded evidence of one-armed oscillations precessing in the prograde direction around the classical Be stars ζ Tau (Vakili et al., 1998) and γ Cas (Berio et al., 1999).

The presence of these density waves explains the observed unequal intensities in the V and R components of double-peaked emission lines (Okazaki, 1996). The perturbation pattern comprises overdense and underdense regions which produce local excesses and deficits of line emission. As the density wave precesses about the central star, the overdense and underdense regions oscillate between approaching and receding with respect to the observer, and the excess and deficit in line emission are Doppler shifted accordingly. Plainly, if the overdense region is approaching and the underdense region is receding, then V $>$ R. If the overdense region is receding and the underdense region is approaching, then V $<$ R. The one-armed oscillation paradigm is consistent with observed timescales of periodic V/R variability in classical Be stars, which exist on timescales of a few years to roughly one decade (Hanuschik et al., 1995; Okazaki, 1997). Phase differences occasionally occur in the V/R ratios of individual lines (Slettebak, 1982; Kogure & Suzuki, 1984). In some stars, asymmetrical IR lines exhibit completely inverted V/R ratios from the optical Balmer lines (Clark & Steele, 2000; Wisniewski et al., 2007a). As these lines originate from different regions of the disk, the morphology of line-emitting regions may differ for each line. This hypothesis was substantiated by Carciofi et al. (2009) who employed a global one-armed oscillation model with a spiral perturbation pattern to successfully reproduce the phase differences in V/R variable Hα and Brγ lines in ζ Tau.

1.2.5 Disk Formation

The formation of the circumstellar disk presents one of the most pressing problems to our current understanding of classical Be stars. The gaseous disks are not remnants

of the objects' protostellar environments, nor are they formed through the accretion of material (Porter & Rivinius, 2003). On the contrary, the equatorial gas consists of a decretion disk formed from material which originates from the central star. How that material is ejected into the equatorial plane and how sufficient angular momentum is transferred to the disk to maintain Keplerian rotation are among the primary unresolved questions currently driving classical Be star research.

A number of empirical models have been devised to explain the means of generating a circumstellar envelope consistent with observations of classical Be stars. The first viable approach, proposed by Struve (1931), theorized that the formation of an equatorial disk could be achieved through direct centrifugal mass ejection from a critically rotating stellar atmosphere. As we have previously discussed, the closeness of the rotation velocities of classical Be stars to the critical limit remains uncertain. If classical Be stars rotate at substantially subcritical velocities, then the energy costs of forming a Keplerian disk require a strong ejection mechanism. If the central stars rotate close to critical velocities, roughly within a sound speed of the critical values (Owocki, 2006), then the options for disk formation include mechanisms which require considerably less energy. Whatever the case, the processes involved in the formation of the disk likely comprise a more intricate scenario then the straightforward method advanced by Struve.

Kříž & Harmanec (1975) proposed that Be stars were the result of mass-transfer in binary systems. While the observational evidence does not support the hypothesis of accretion of gas originating from a companion, binary systems may nevertheless play some important role in the Be phenomenon. For example, McSwain & Gies (2005) suggest that classical Be stars may be spun-up to near-critical velocities by mass-transfer from their companions. However, it should be noted that current census studies suggest that the frequency of binarity in Be stars does not exceed one-third (Porter & Rivinius, 2003). Hence, if binarity does have a role in the classical Be phenomenon, a separate channel for the formation of these objects must exist for single stars. Furthermore, Oudmaijer & Parr (2010) demonstrated convincing similarity in the binary parameters of Be and normal B-type binaries, suggesting that the Be phenomenon is not the result of a fundamentally different star formation mechanism.

Among the first dynamical approaches, Bjorkman & Cassinelli (1993) hypothe-

sized that radiatively-driven stellar winds could channel the flow of gas towards the circumstellar midplane to produce a *wind-compressed disk*. In this model, the wind streamlines from the opposing hemispheres intercept each other at the equator resulting in a dense region of gas confined to the midplane by wind pressure on either side. While initially a promising approach supported by dynamical simulations (Owocki et al., 1994), the model fails to produce a disk when nonradial line driving forces are considered (Owocki et al., 1996). Furthermore, radiatively-driven winds cannot account for the steady input of angular momentum required to produce a Keplerian disk. As such, the model fails to maintain gas densities sufficient for reproducing the emission features of the disk (Porter, 1997).

It has long been envisioned that magnetic fields could play an important role in producing the circumstellar disks of classical Be stars. For example, the wind-compressed model can be modified to include the presence of a magnetic field that channels the wind flow to produce a *magnetically-torqued disk* (Cassinelli et al., 2002). In this model, closed magnetic fields loops near the equator direct the streamlines of gaseous flow towards the equatorial plane from both hemispheres. The magnetic field torques the material up to orbital speeds required to overcome gravity. Magnetohydrodynamic simulations determined that these models become dominated by radial inflows or outflows such that no Keplerian disk forms (Owocki, 2006). While magnetic fields can be used in other ways to channel material into the equatorial plane, it has now been shown that classical Be stars in general do not possess large-scale magnetic fields (Grunhut et al., 2012).

If rotational velocities are nearly critical, then non-radial pulsations are a prime candidate for driving mass-loss from the stellar surface. Osaki (1986) proposed that the dissipation of non-radial pulsations in the stellar atmosphere could supply the gas with the necessary angular momentum to achieve orbit. In the case of specific stars, such as μ Cen, time-dependent observations of the line-emission intensity and the multiperiodic pattern of the pulsations suggest that the interval of mass ejection is coinciding with the beat period of the pulsation (Rivinius et al., 1997, 1999, 2001). However, estimates of mass-loss rates from non-radial pulsations do not seem to be able to account for the amount of gas required to reproduce the observational properties.

Hence, the nature of the physical mechanisms that inject gas and angular momentum into the midplane of classical Be stars remains undetermined. Certainly, any viable model for disk formation requires specific elements: a means for ejecting gas into orbit with a mass-loss rate that can exceed the viscous dissipation timescales and a means for supplying sufficient angular momentum to maintain Keplerian rotation. The solution may inevitably depend on arriving at a definitive answer to the question of how close to critical do classical Be stars rotate.

Whatever processes contribute to the transfer of mass and angular momentum to the circumstellar environment, the dissipation of the disk likely occurs when those processes become dormant or significantly weaker than the dissipative effects at work on the circumstellar gas. Dissipation is thought to occur through ablation of the disk from radiatively-driven winds (Gayley et al., 1999) or entrainment of the gas in Kelvin-Helmholtz instabilities in the shear layer between the disk and the fast stellar wind (Bjorkman, 2000a). Furthermore, gas in the inner region must be viscously reaccreting back onto the star, although observations have been unable to ascertain whether or not this occurs (Hanuschik, 1995).

1.2.6 Evolutionary Status

As with the disk formation mechanism, considerable uncertainty pervades any discussion of the evolutionary status of classical Be stars. The origin of the classical Be phenomenon may be associated with the inherent evolutionary characteristics of the stars that constitute this group. Numerous studies have aimed at determining the fraction of Be to B-type stars in the galaxy. Merrill & Burwell (1933) provided a first estimate of the Be star fraction of 10 to 15% for early B-type stars. The mean frequency of Be stars counting all spectral types and luminosity classes seems to have risen as the fraction of undetected Be stars decreases with each update to the sample of stars: from a value of 12% provided by Jaschek & Jaschek (1983) to 15% by Coté & van Kerkwijk (1993) to 17% by Zorec & Briot (1997). Despite the differences among the studies, the general trend shows an increase from B0 to B1-B2 (Zorec & Briot (1997) found a peak of 34% in B1 stars) followed by a decrease towards later spectral types. The problem remains that as Be stars are variable, a star that would normally be identified as a Be

star might be observed during a disk-less period and be recorded as a regular B-type star. Hence, attempts to determine the fraction of the Be stars within a particular sample likely only provide a lower limit (Porter & Rivinius, 2003). Furthermore, these census studies do not distinguish between classical Be stars and other Be stars.

On the question of evolutionary age in the Be phenomenon, there are conflicting results. Fabregat & Torrejón (2000) and Keller et al. (2000) suggest that the phenomenon occurs largely in the later half of a typical B-type star's main sequence lifetime (i.e. that Be stars only appear in clusters older than 10 Myr). Mathew et al. (2008) and Wisniewski & Bjorkman (2006) counter with results that suggest that the phenomenon is present throughout the entire main sequence, although Wisniewski & Bjorkman (2006) acknowledge that an enhanced fraction seems to exist in older clusters. The frequency of the Be phenomenon does not depend on luminosity class (Slettebak, 1982). Furthermore, Zorec & Briot (1997) showed that the frequency distribution is consistent across luminosity classes II-V. These results demonstrate the difficulty in attributing any particular evolutionary state to Be stars. The apparent even distribution of Be stars across all luminosity classes may suggest instead that the Be phenomenon depends on conditions of star formation. Whatever the case may be, the evolutionary status of Be stars remains an unresolved question in the current understanding of Be stars.

Assessments of the fractional Be star populations in Milky Way (MW), Small Magellanic Cloud (SMC) and Large Magellanic Cloud (LMC) clusters suggest that the fraction of Be stars is higher in low-metallicity environments (Maeder et al., 1999). This result has important implications for the nature of classical Be stars as metallicity may have an important effect on whether or not stars can attain critical rotational velocities (Maeder & Maynet, 2001). As radiatively-driven mass-loss increases with metallicity (Vink et al., 2001), stars in higher-metallicity environments may have a more difficult time attaining critical velocities. As a result, these stars may account for the enhanced fraction of Be stars in older clusters. Furthermore, to account for the higher fraction of Be stars in low metallicity environments, Ekström et al. (2008) suggest that these stars are born with higher values of v_{eq}/v_{crit}.

1.3 Polarization

Previously introduced as one of the principal observational characteristics of classical Be stars, the distinct linear polarization signature is the main focus of this thesis. Since the first reports of intrinsic polarization in Be stars by Hall & Mikesell (1950) and Behr (1959), this phenomenon has been the subject of many investigations. The polarigenic mechanism responsible for the intrinsic polarization is now known to be the scattering of radiation in a flattened envelope of gas (see, for example, Coyne & Kruszewski, 1969; Zellner & Serkowski, 1972). In this section, we present a brief review of the key concepts relevant to our theoretical investigation of the linear polarization in classical Be stars.

1.3.1 The Stokes Parameters

As light generally becomes polarized upon being scattered, the treatment of the scattering problem requires the inclusion of the state of polarization in the description of the radiation field. Therefore, such a description must consist of four independent parameters characterizing the intensity of the radiation, the degree of polarization, the polarization position angle and the ellipticity. To express these quantities that describe an elliptically polarized beam of light, we use the convenient representation first introduced by Stokes (1852). This formulation requires four parameters that are collectively labelled the *Stokes parameters* and are expressed, using Chandrasekhar's familiar notation, with the letters I, Q, U and V. These parameters represent the total intensity of the light (I), the linear polarization of the light (Q and U) and the circular polarization of the light (V).

When there is no coherence in the oscillations of the electric field, then

$$Q = U = V = 0. \tag{1.3}$$

and the light is considered *unpolarized*. Conversely, the light is said to be *perfectly polarized* when the Stokes parameters satisfy the relationship

$$I^2 = Q^2 + U^2 + V^2. \tag{1.4}$$

When the light is partially polarized, the total intensity of the light satisfies

$$I^2 \geq Q^2 + U^2 + V^2. \tag{1.5}$$

We can easily relate the Stokes parameters to the previously mentioned set of four mathematical descriptors of the light. The intensity of the beam of radiation is already expressed by the I Stokes parameter. The degree of polarization is expressed as

$$P = \frac{(Q^2 + U^2 + V^2)^{1/2}}{I} \tag{1.6}$$

or normalized as

$$p = (q^2 + u^2 + v^2)^{1/2} \tag{1.7}$$

where $q = Q/I$, $u = U/I$ and $v = V/I$. The polarization angle χ, or the direction of vibration of the polarization, and ellipticity β are expressed in terms of the Stokes parameters as

$$\tan 2\chi = \frac{u}{q} \tag{1.8}$$

and

$$\sin 2\beta = v. \tag{1.9}$$

The practicality of the Stokes parameters arises from the simplicity in measuring these quantities. Physically, the Stokes parameters represent the sums or differences in intensity between components of the radiation field measured along the defining axes, as illustrated in Figure 1.2. The I parameter is simply the total intensity of the beam of light. If one measures the intensity along an axis using a filter which transmits a single direction of vibration and also measures the intensity along the perpendicular axis by rotating the polarizer by 90°, then the difference between the two intensities yields the value of one of the two linear polarization parameters, either Q or U. The value of the second linear polarization parameters can be determined from the pair of orthogonal axes fixed at 45° from the initial set of orthogonal axes. The circular polarization parameter V can be measured in similar fashion by inserting a quarter-wave plate in the beam to convert the circular polarization into linear form. For the remainder of this text, we will not discuss V as it is not affected by the polarigenic

mechanism considered in this work, electron scattering.

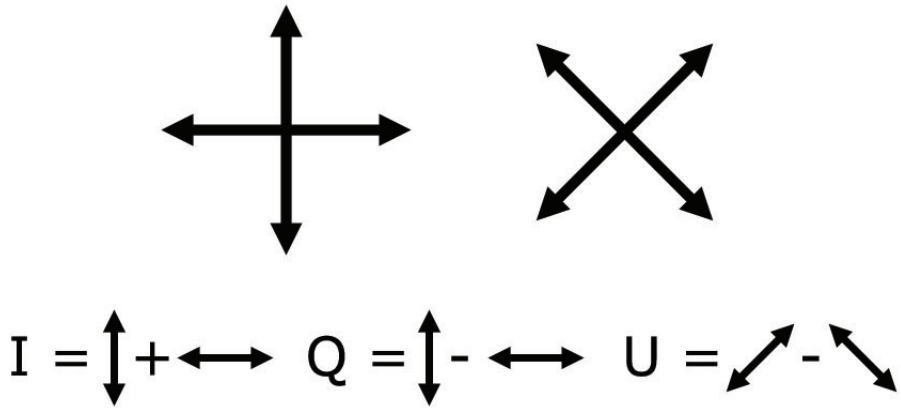

Figure 1.2: Schematic representation of the polarization vectors that comprise the total intensity of the radiation field I and the two linear polarization parameters Q and U. Geometrically, Q represents the difference in intensity between components of the electric field vector along two orthogonal axes, U represents the difference in intensity between components of the electric field vector along two orthogonal axes rotated 45° from the Q directions.

We now define two orthogonal directions in the plane transverse to the direction of propagation of the light observed from a star (i.e. on the plane of the sky). We label these arbitrarily-chosen directions the NS (North-South) and the EW (East-West) directions. In Figure 1.3, we illustrate the representation of these directions as defined in this thesis in the context of a star surrounded by a circumstellar disk. Finally, we can express the I, Q and U Stokes parameters in terms of the intensity of the light measured along axes defined by the two directions as

$$I = I_{NS} + I_{EW}, \tag{1.10}$$

$$Q = I_{NS} - I_{EW}, \tag{1.11}$$

and

$$U = I_{NS+\frac{\pi}{4}} - I_{EW+\frac{\pi}{4}}. \tag{1.12}$$

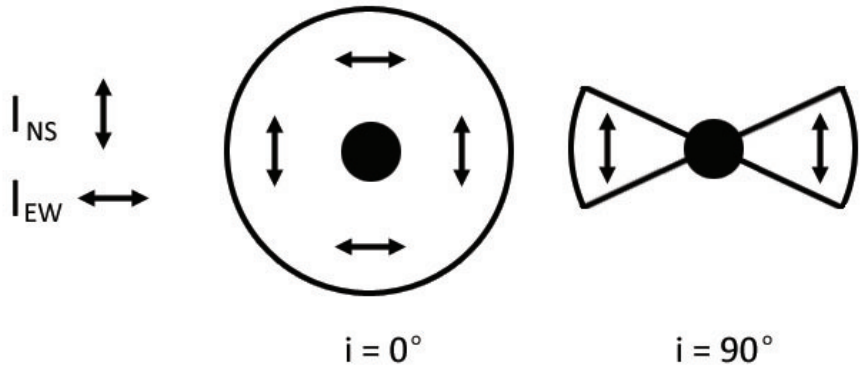

Figure 1.3: Schematic representation of the polarization vectors that comprise the total intensity of the radiation field I in the context of a circumstellar disk projected onto the plane of the sky. This representation allows us to express the Stokes parameters in terms of the intensity of light measured along two predefined axes (see text).

1.3.2 Polarization from Axisymmetric Disks

When unpolarized light undergoes scattering by free electrons, it becomes linearly polarized perpendicular to the plane containing the incident and scattered radiation. While the electric vector perpendicular to the scattering plane is unaffected by the scattering, the vector parallel to the plane is reduced by the cosine of the scattering angle. When this process occurs in a source that appears spherically symmetric on the plane of the sky, the distribution of polarizing planes is uniform, resulting in a complete cancellation of vibrations from orthogonal directions, or $Q = 0$ and $U = 0$. The projection of the circumstellar disk is spherically symmetric when the stellar rotational axis aligns with the observer's line-of-sight. Thus, classical Be stars should exhibit zero net polarization when viewed pole-on.

When the rotational axis of the system is inclined with respect to the direction of an observer, the projection of the disk on the plane of the sky becomes non-radially symmetric and a complete cancellation of the vibrations does not occur, so that we have $Q > 0$ and $U = 0$. The second linear polarization intensity is still zero as changing the inclination angle does not alter the symmetry of the system along the second set of axes. Thus, classical Be stars exhibit net polarization when viewed at inclinations greater than zero. The polarimetric position angle, aligned along the dominant polarization vector, is cast perpendicularly to the plane of the disk.

1.3.3 The Linear Polarization Signature

Classical Be stars exhibit a distinct intrinsic linear polarization signature, as illustrated in Figure 1.4. The source of the polarized light, electron scattering, is a wavelength-independent process, yet the polarimetric spectra of classical Be stars often show definite variations with respect to wavelength, as first reported by Coyne & Gehrels (1967) and Serkowski (1968). In particular, the spectra may include abrupt jumps in the polarization level at the hydrogen excitation series limits and relatively smaller levels of polarization in emission lines. Thus, there are separate continuum and line effects which contribute to the observed wavelength-dependence.

- The first effect is the dilution of the polarized light from the emission of unpolarized light by material outside of the scattering region. The addition of unpolarized light at particular wavelengths results in a decrease in the ratio of the polarized intensity to the total intensity. This decrease in the polarization level is noticeable in strong emission lines that arise largely in extended regions of the circumstellar disk, outside of the scattering region. Spectropolarimetric line profiles, indicative of Doppler-shifted line opacity due to the motion of the gas in the envelope (Wood & Bjorkman, 1995), have been extensively observed (early studies include Clarke & Mclean, 1975; Poeckert, 1975; Poeckert et al., 1979). Variations in the polarization angle arise from the asymmetric relative velocities of the V and R line components.

- The second effect is the attenuation of scattered light due to continuum opacity in the disk. In particular, the neutral hydrogen opacity produces a distinct saw-tooth imprint from pre- and post-scattering absorption that is commonly observed in the polarization spectra of classical Be stars (for example Poeckert et al., 1979; Wood et al., 1997). The polarization angle remains constant across the polarimetric continuum as long as the scatterers are distributed axisymmetrically. Depolarization owing to the effects of metal-line blanketing can have a pseudo-continuous effect on the polarimetric spectra, particularly in the ultraviolet (Bjorkman, 2000b).

Variable spectropolarimetric signatures have been observed in numerous classical Be stars. For a detailed review of polarimetric observations of classical Be stars, we refer

interested readers to Chapter 13 of Clarke (2010).

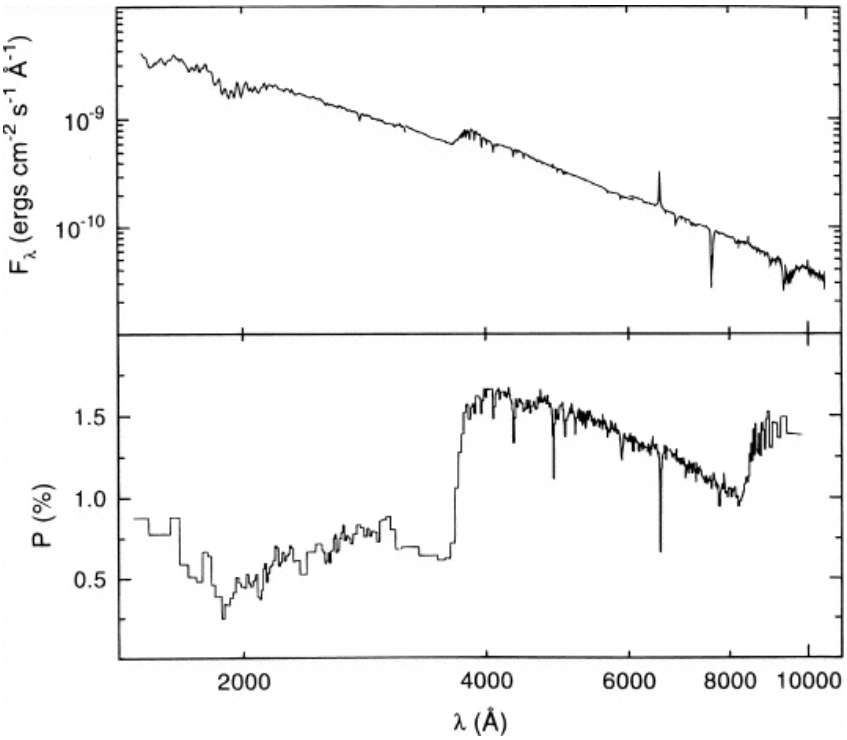

Figure 1.4: Flux (top panel) and linear polarization (bottom panel) spectrum of the classical Be star ζ Tau. This spectropolarimetric data illustrates the imprint of neutral hydrogen absorption in the optical region and metal-line blanketing in the UV. Image taken from Figure 3 of Wood et al. (1997).

1.3.4 Previous Modelling Efforts

While Chandrasekhar (1960) and Collins (1970) provided analytic solutions for predicting the fraction of polarized light generated by scattering in plane-parallel atmospheres, the first general expressions for the polarization levels produced in Thomson scattering circumstellar envelopes were derived by Brown & McLean (1977). In their analysis, they considered axisymmetric, ionized envelopes of gas centred on a point source radiating unpolarized light. They determined that the polarization level observed from single-scattering incidents in such an envelope, when viewed at an arbitrary inclination i and neglecting the effects of disk absorption and emission, is

$$p \simeq \overline{\tau_{es}}(1 - 3\gamma)\sin^2 i, \tag{1.13}$$

where the parameter γ is related to the shape of the envelope and $\overline{\tau_{es}}$ is a mean electron scattering optical depth. From this expression, the maximum polarization for any given distribution of gas occurs when the inclination of the system is at 90°, while the polarization decreases with decreasing inclination.

This analytic expression of Brown & McLean was further studied by others, coinciding with an increasing interest in using the polarization measurements as a diagnostic of envelope geometry. Cassinelli et al. (1987) and Brown et al. (1989) found that considering a source of illumination with a finite angular extent significantly reduced the net polarization from scattering envelopes. Brown & Fox (1989) and Fox & Brown (1991) investigated the effect of occultation of the envelope by the stellar disk and found that occultation enhances the net polarization at low inclinations while reducing it at high inclinations. Finally, Fox (1991) concluded that the polarization arising from electron scattering envelopes as a function of inclination is a complex, model-dependent expression that is not adequately described as $p \propto \sin^2 i$.

The effects of multiple-scattering in circumstellar envelopes were investigated by Wood et al. (1996a) using Monte Carlo radiative transfer simulations. Prior to the advent of computational methods capable of tackling this process, it was anticipated that multiple-scattering would reduce the net polarization (Waters & Marlborough, 1992). Conversely, Wood et al. showed that multiple-scattering yields polarization levels that exceed those predicted from single-scattering treatments owing to an increased bias in the orientation of the scattering planes. Furthermore, they found that, given a multiple-scattering environment, the finite size of the stellar disk enhances the net polarization rather than diminishing it. With the inclusion of the absorptive opacity, Wood et al. (1996b) found that the average polarization levels declined to the levels predicted from single-scattering treatments. However, at wavelengths where the absorptive opacity changes abruptly (i.e. at the hydrogen series limits), they noted the importance of multiple-scattering in reproducing the discontinuities in the polarimetric spectrum because of their predicted increase in polarization (relative to single-scattering approximations) where the absorptive opacity is lowest.

1.4 Summary

Classical Be stars are an interesting class of rapidly-rotating, massive stars that are associated with gaseous circumstellar disks. The observational features of these objects reflect the interaction of stellar radiation from the hot star with the cooler material in the circumstellar environment. These features include:

- spectral line emission arising from recombination in the highly-ionized circumstellar gas;
- excess continuum emission produced by the reprocessing of stellar radiation in the disk;
- linear polarization of light arising from Thomson scattering in the flattened envelope; and
- long-term variability owing to the transient nature of the circumstellar disk and to dynamical processes occurring therein.

The physical and kinematic nature of these objects has been largely agreed upon owing to the interpretation of the distinctive set of observational characteristics that these stars exhibit. The circumstellar envelope is a geometrically-thin, decretion disk of gas orbiting the central star with near-Keplerian orbital velocities. Despite this knowledge, our understanding of classical Be stars remains burdened by a few unanswered questions on the dynamical front. Principally, we lack a clear description of the physical process(es) through which the disks form and a complete picture of the evolutionary status of these objects. Addressing these deficiencies is the overarching objective of current theoretical and observational investigations of classical Be stars.

The focus of this thesis is the continuous linear polarization signature in the radiation emitted by classical Be stars. Polarimetric observations directly probe the circumstellar environment in which scattering occurs and can provide us with crucial information regarding the geometric and physical properties of these systems. Our goal is to use the continuous polarization signature to explore the dynamical nature of the circumstellar envelopes. First, we developed a computational procedure using sophisticated non-LTE radiative transfer techniques to calculate the Stokes intensities

for models of classical Be stars, as explained in Chapter 2. Next, we analyzed the linear polarization signature to highlight the diagnostic potential of polarimetry for studying the dynamical nature of the circumstellar disks around classical Be stars. We present detailed results of these investigations in Chapters 3 through 5. Finally, in Chapter 6, we reiterate the important findings presented in this thesis and we discuss the relevance of our work in the context of present-day classical Be star research.

Bibliography

Abbott D. C. 1982, ApJ, 263, 723

Ashok, N. M., Bhatt, H. C., Kulkarni, P. V. & Joshi, S. C. 1984, MNRAS, 211, 471

Baade, D. 1982, A&A, 105, 65

Balona, L. A., 1990, MNRAS, 245, 92

Balona, L. A., 1995, MNRAS, 277, 1547

Behr, A. 1959, Nach. Akad. Wiss. Gottingen 2, Math-Phys.KL, No. 7, 185

Berio, P., et al. 1999, A&A, 345, 203

Bjorkman, J. E. 2000, in IAU Colloq. 175: The Be Phenomenon in Early-Type Stars, ed. M. A. Smith, H. F. Henrichs, & J. Fabregat, (ASP Conf. Ser. 214, San Francisco: ASP), 435

Bjorkman, K. S. 2000, in IAU Colloq. 175: The Be Phenomenon in Early-Type Stars, ed. M. A. Smith, H. F. Henrichs, & J. Fabregat, (ASP Conf. Ser. 214, San Francisco: ASP), 384

Bjorkman, J. E. & Cassinelli, J. P. 1993, ApJ, 409, 429

Brown, J.C. & McLean, I.S. 1977, A&A, 57, 141

Brown, J.C., Carlaw, V. A., & Cassinelli, J. P. 1989, ApJ, 344, 341

Brown, J.C. & Fox, G. K. 1989, ApJ, 347, 468

Carciofi, A.C., & Bjorkman, J.E. 2006, ApJ, 639, 1081

Carciofi, A.C., & Bjorkman, J.E. 2008, ApJ, 684, 1374

Carciofi, A. C., Okazaki, A. T., le Bouquin, J.-B., Stefl, S., Rivinius, Th., Baade, D., Bjorkman, J. E., & Hummel, C. A. 2009, A&A, 504, 915

Carciofi, A. C., Miroshnichenko, A. S., Kusakin, A. V., Bjorkman, J. E., Bjorkman, K. S., Marang, F., Kuratov, K. S., García-Lario, P., Calderón, J. V. Perea, Fabregat, J., & Magalhães, A. M. 2006, ApJ, 652, 1617

Carciofi, A. C. 2011, in IAU Symp. 272: Active OB Stars: Structure, Evolution, Mass Loss, and Critical Limits, ed. C. Neiner et al. (Cambridge: Cambridge Univ. Press), 325

Cassinelli, J. P., Nordsieck, K. H., Murison, M. A. 1987, ApJ, 317, 290

Cassinelli, J. P., Brown, J. C., Maheswaran, M., Miller, N. A., & Telfer, D. C. 2002, ApJ, 578, 951

Castor, J. I., Abbott, D. C.,& Klein, R. I. 1975, ApJ, 195, 157

Chandrasekhar, S. 1960, Radiative Transfer (1st ed.; New York: Dover)

Clark, J. S., & Steele, I. A., 2000, A&AS, 141, 65

Clarke, D. 2010, Stellar Polarimetry, (1st ed.; Germany: Wiley-VCH)

Clarke, D., & Mclean, I. S. 1975, MNRAS, 173, 21

Collins, G. W., II, 1963, ApJ, 138, 1134

Collins, G.W. 1970, ApJ, 159, 583

Collins, G. W., II, 1987, IAU Colloq. 92, Physics of Be Stars, eds. A. Slettebak & T. P. Snow, Cambridge: Cambridge Univ. Press, 3

Collins, G. W. & Truax, R. J. 1995, ApJ, 439, 860

Coté J., & van Kerkwijk M.H. 1993, A&A, 274, 870

Cox, A.N. 2000, Allen's Astrophysical Quantities, (4th ed.; New York: Springer)

Coyne, G. V., & Gehrels, T. 1967, AJ, 72, 887

Coyne, G. V,. & Kruszewski, A. 1969, ApJ, 74, 528

Dougherty, S. M., & Taylor, A. R. 1992, Nature, 359, 808

Ekström, S., Meynet, G., Maeder, A., & Barblan, F. 2008, A&A, 478, 467

Fabregat, J. & Torrejón, J. M. 2000, A&A, 357, 451

Fox, G. K., & Brown, J. C. 1991, ApJ, 375, 300

Fox, G. K. 1991, ApJ, 379, 663

Gayley, K. G., Ignace, R. & Owocki, S. P. 2001, ApJ, 558, 802

Gayley, K. G., Owocki, S. P. & Cranmer, S. R. 1999, ApJ, 513, 442

Gehrz, R. D., Hackwell, J. A., & Jones, T. W. 1974, ApJ, 191, 675

Ghosh, K. K., Iyengar, K. V. K., Ramsey, B. D. & Austin, R. A. 1999, ApJ, 118, 1061

Grunhut, J. H., Wade, G. A., & MiMeS Collaboration. 2012, American Institute of Physics Conference Series, 1429, 67

Hall, J.S., & Mikesell, A.H. 1950, Publications of the U.S. Naval Observatory Second Series, 17, 1

Hanuschik, R. W. 1995, A&A, 295, 423

Hanuschik, R. W., Hummel, W., Dietle, O. & Satorius, E. 1995, A&A, 300, 163

Hanuschik, R. W. 1996, A&A, 308, 170

Hanuschik, R. W., Hummel, W., Satorius, E. Dietle, O. & Thimm, G. 1996, A&AS, 116, 309

Hanuschik, R. W. 2000, in IAU Colloq. 175: The Be Phenomenon in Early-Type Stars, ed. M. A. Smith, H. F. Henrichs, & J. Fabregat, (ASP Conf. Ser. 214, San Francisco: ASP), 518

Harmanec, P. 1983, Hvar Obs. Bull., 7, 55

Houck, J. R. et al. 2004, ApJS, 154, 18

Hummel, W. & Vrancken, M. 2000, A&A, 359, 1075

Jaschek, M., Slettebak, A., & Jaschek, C. 1981, Be Star Newsletter, 4, 9

Jaschek, C. & Jaschek, M. 1983, A&A, 117, 357

Jaschek, C. & Jaschek, M. 1987, The Classification of Stars (4th ed., Cambridge: Cambridge Univ. Press)

Jaschek, C. & Jaschek, M. 1993, A&AS, 97, 807

Kato, S. 1983, PASJ, 35, 249

Keller, S. C., Bessel, M. S., & Dacosta, G. S. 2000, in IAU Colloq. 175: The Be Phenomenon in Early-Type Stars, ed. M. A. Smith, H. F. Henrichs, & J. Fabregat, (ASP Conf. Ser. 214, San Francisco: ASP), 75

Kogure, T., & Suzuki, M. 1984, PASJ, 36, 191

Kogure, T. & Leung, K.-C. 2007, The Astrophysics of Emission-Line Stars (New York: Springer)

Kříž, S., & Harmanec, P. 1975, Bull. Astron. Inst. Czechoslovakia, 26. 65

Lee, U., Osaki, Y., Saio, H. 1991, MNRAS, 250, 432

McLean, I. S., & Brown, J. C. 1978, A&A, 69, 291

Maeder A., & Meynet, G. 2001, A&A, 373, 555

Maeder, A., Grebel, E. K., & Mermilliod, J.-C. 1999, A&A, 346, 559

Mathew, B., Subramaniam, A., & Bhatt, B. C. 2008, MNRAS, 388, 1879

Mennickent, R. E., Sterken, C. & Vogt, N. 1997, A&A, 326, 1167

McSwain, M. V. & Gies, D. R. 2005, ApJ, 622, 1052

Merrill P. W., & Burwell C.G. 1933, ApJ, 78, 87

Okazaki, A. T. 1991, PASJ, 43, 75

Okazaki, A. T. 1996, PASJ, 48, 305

Okazaki, A. T. 1997, A&A, 318, 548

Okazaki, A. T. 2001, PASJ, 53, 119

Okazaki, A. T. 2007, in Active OB-Stars: Laboratories for Stellar and Circumstellar Physics, ed. S. Štefl, S. P. Owocki, & A. T. Okazaki, (ASP, Conf. Ser. 316, San Francisco: ASP), 230

Osaki, Y. 1986, PASP, 98, 30

Osaki, Y. 1999, in IAU Colloq. 169: Non-radially pulsating hot stars: Non-radial pulsations and Be phenomenon. Variable Stars and Non-spherical Stellar Winds in Luminous Hot Stars, ed. Wolf, B., Stahl, O. and Fullerton, A. W., (Berlin and Heiderberg: Springer-Verlag), 329

Oudmaijer, R. D., & Parr, A. M. 2010, MNRAS, 405, 2439

Owocki, S. P., Cranmer, S. R., & Blondin, J. M. 1994, in IAU Symp. 162: Pulsation, Rotation and Mass Loss in Early-Type Stars, ed. L. A. Balona, H. F. Henrichs, & J. M. Le Contel, (Dordrecht: Kluwer), 399

Owocki, S. P., Cranmer, S. R., & Gayley, K. G. 1996, ApJ, 472, 115

Owocki, S. P. 2006, in Stars with the B[e] Phenomenon, ed. M. Kraus, & A.S. Miroshnichenko, vol. 355 of Astronomical Society of the Pacific Conference Series, 219

Papaloizou, J. C., Savonije, G. J. & Henrichs, H. F. 1992, A&A, 265, L45

Poeckert, R. 1975, ApJ, 196, 777

Poeckert, R., Bastien, P., & Landstreet, J.D. 1979, AJ, 84, 812

Porter, J. M. 1996, MNRAS, 280, 31

Porter, J. M. 1997, A&A, 324, 597

Porter, J. M. 1999, A&A, 348, 512

Porter, J. M. 2003, Be Star Newsletter, 36, 6

Porter, J. M. & Rivinius, T. 2003, PASP, 115, 1153

Pringle, J. E. 1981, ARA& A, 19, 17

Quirrenbach, A., et al. 1993, ApJ, 416, 25

Quirrenbach, A., et al. 1994, A&A, 283, 13

Quirrenbach, A., et al. 1997, ApJ, 479, 477

Rivinius, Th., Baade, D., Štefl, S., Stahl, O., Wolf, B., & Kaufe, A. 1997, in A Half Century of Stellar Pulsation Interpretations: A Tribute to Arthur N. Cox, ed. P. A. Bradley, J. A. Guzik, (ASP: San Francisco), 343

Rivinius, Th., et al. 1998, A&A, 336, 177

Rivinius, Th., Štefl, S., & Baade, D. 1999, A&A, 348, 831

Rivinius, Th., Baade, D., Štefl, S., & Maintz, M. 2001, A&A, 369, 1058

Rivinius, Th., Baade, D. & Štefl, S. 2003, A&A, 411, 229

Rosseland, S. 1926, ApJ, 63, 218

Secchi, A. 1867, Astron. Nachr., 68, 63

Serkowski, K. 1968, ApJ, 154, 115

Shakura, N. L., & Sunyaev, R. A. 1973, A&A, 24, 337

Silaj. J., Jones, C. E., Tycner, C., Sigut, T. A. A. & Smith, A. D. 2010, ApJS, 187, 228

Slettebak, A., Collins, G. W., Parkinson, T. D., Boyce, P. B., & White, N. M. 1975, ApJS, 29, 137

Slettebak, A. 1982, ApJS, 50, 55

Slettebak, A. 1994, ApJS, 94, 163

Slettebak, A. Collins II, G. W. & Traux, R. 1992, ApJS, 94, 163

Stee, P. et al. 1995, A&A, 300, 219

Stoekcley, T. R., 1968, MNRAS, 140, 141

Stokes, G. G., 1852, Trans. Cambridge Philos. Soc., 9, 399

Struve, O. 1931, ApJ, 73, 94

Telting, J. H., Heemskerk, M. H. M., Henrichs, H. F. & Savonije, G. J. 1994, A&A, 288, 558

Townsend, R. H. D., Owocki, S. P., & Howarth, I. D. 2004, MNRAS, 350, 189

Townsend, R. H. D., Owocki, S. P., & Groote, D., 2005, ApJ, 630, 81

Tycner, C. et al. 2004, AJ, 127, 1194

Vakili, F., Mourard, D., Stee, Ph., Bonneau, D., Berio, P., Chesneau, O., Thureau, N., Morand, F., Labeyrie, A., & Tallon-Bosc, I. 1998, A&A, 335, 261

Vink, J. S., de Koter, A., & Lamers, H. J. G. L. M. 2001, A&A, 369, 574

Waters, L. B. F. M. 1986, A&A, 162, 121

Waters, L. B. F. M., & Marlborough, J. M. 1992, A&A, 256, 195

Waters, L. B. F. M., & Marlborough, J. M. 1994, in IAU Symp. 162: Pulsation, Rotation and Mass Loss in Early-Type Stars, ed. L. A. Balona, H. F. Henrichs, & J. M. Le Contel, (Dordrecht: Kluwer), 399

Waters, L. B. F. M., Coté, J., & Lamers, H. J. G. L. M. 1987, A&A, 185, 206

Wheelwright, H. E., Bjorkman, J. E., Oudmaijer, R. D., Carciofi, A. C., Bjorkman, K. S., & Porter, J. M. MNRAS, 423, 11

Wisniewski, J.P. & Bjorkman, K. S. 2006, ApJ, 652, 458

Wisniewski, J. P., Bjorkman, K. S., Magalhaes, A. M., Bjorkman, J. E., Meade, M. R., Pereyra, A. 2007, ApJ, 671, 2040

Wisniewski, J. P., Kowalski, A. F., Bjorkman, K. S., Bjorkman, J. E., Carciofi, A. C. 2007, ApJ, 656, 21

Wood, K. & Bjorkman, J. E. 1995, ApJ, 443, 348

Wood, K., Bjorkman, J.E., Whitney, B.A., & Code, A.D. 1996, ApJ, 461, 828

Wood, K., Bjorkman, J.E., Whitney, B.A., & Code, A.D. 1996, ApJ, 461, 847

Wood, K., Bjorkman, K. S. & Bjorkman, J. E. 1997, ApJ, 477, 926

Yudin, R. V. 2001, A&A, 368, 912

Zeipel, H. V. 1924, MNRAS, 84, 665

Zellner, B. H., & Serkowski, K. 1972, PASP, 84, 619

Zorec, J. & Briot, D. 1997, A&A, 318, 443

Chapter 2

Computational Radiative Transfer

Sections 2.3.3 - 2.3.5 of this chapter are a modified version of Appendix B from Halonen, R. J., Mackay, F. E., & Jones, C. E., 2013, ApJS, 204, 11.

2.1 Introduction

The production of synthetic observables of celestial objects generally requires computing the transfer of radiation through specific environments. In this chapter, we provide a description of two computational codes designed to address radiative transfer through the circumstellar disks that surround classical Be stars. The code BEDISK determines the temperature structure and atomic level populations of the gas in the circumstellar disk. BEDISK was developed prior to the commencement of this project (Sigut & Jones, 2007). The code MCTRACE employs a Monte Carlo simulation for determining the Stokes parameters of the light emitted by a classical Be star using the state of the circumstellar gas computed by BEDISK. MCTRACE was designed as part of this research endeavour and was developed, tested and implemented by the author of this thesis.

2.2 Radiative Transfer Code BEDISK

The radiative transfer code BEDISK computes the temperature structure of a classical Be star disk by solving the coupled problems of radiative equilibrium, statistical equi-

librium and radiative transfer. This code has now been used extensively in modelling the circumstellar disks and investigating the properties of classical Be stars. The code has been employed to interpret the interferometric signature of classical Be stars (Tycner et al., 2008; Jones et al., 2008a; Grzenia et al., 2013), to reproduce the IR continuum excess (Sigut & Jones, 2007; Halonen et al., 2008) and IR line flux (Jones et al., 2009), to investigate the effects of gravitational darkening on the thermal structure of the disk (McGill et al., 2011, 2013), to probe the correlation between Hα emission and visual magnitude (Sigut & Patel, 2013), to perform a systematic study of Hα line profiles (Silaj et al., 2010), to study the viscous disk model in a hydrodynamic context (Jones et al., 2008b), to study the temperature structure of disks in the Small Magellanic Cloud (Ahmed & Sigut, 2012) and to predict the visibilities of a disk measured using interferometric polarimetry (Mackay et al., 2009). In this section, we provide an overview of the BEDISK code. A complete description of the code can be found in Sigut & Jones (2007).

2.2.1 Radiative Equilibrium Solution

In a series of papers, Millar & Marlborough (1998, 1999a,b), hereafter MM, demonstrated the importance of enforcing radiative equilibrium in determining the thermal structure of the circumstellar gas self-consistently. Prior to their work, models of Be star disks assumed that the temperature of the gas could be approximated using a single, isothermal value, typically set anywhere from 0.5 to 0.8 of $T_{\rm eff}$ (the stellar effective temperature of the central star). MM found that while the isothermal assumption is valid as a first approximation in the low-density parts of the disk, the temperature structure in the denser parts, particularly in the midplane and near the surface of the star, deviates significantly from the isothermal value. It has since been established that using a radiative equilibrium enforced, non-isothermal temperature structure is essential for considering the predicted observables of classical Be stars (Sigut & Jones, 2007; Carciofi & Bjorkman, 2006).

Solving the radiative equilibrium problem requires balancing the energy gains and losses from radiative processes at each computational grid point. In BEDISK, heating of the gas occurs through photoionization and collisional excitation, while cooling

processes include recombination and collisional de-excitation. To compute the energy rates for these processes, the atomic level populations and ionization state of the gas are determined by solving the statistical equilibrium equations for each element included in the computation. The BEDISK code includes radiative and collisional processes for nine elements (H, He, C, N, O, Mg, Si, Ca, Fe) with each atom having several ionization stages. The temperatures in each computational grid point are adjusted iteratively until the rates of energy gain and loss are balanced at each location.

The energy input into the system originates entirely from the central star. The radiation field is set using ATLAS9 (Kurucz, 1993) LTE photoionizing fluxes. The diffuse field in the disk is treated using an on-the-spot approximation in which every recombination to the ground level of hydrogen is reabsorbed locally (Osterbrock, 1989). This is a reasonable assumption when the gas densities are high, and allows for the code to account for an important source of radiation in the densest parts of the disk where enforcing radiative equilibrium is most critical (Sigut & Jones, 2007).

2.2.2 Computational Disk Structure

The BEDISK code sets a two-dimensional computational domain for the circumstellar environment using the cylindrical coordinates R and Z. These coordinates represent the radial distance from the rotation axis and the height above the midplane, respectively. The density structure of circumstellar disk, assumed to be axisymmetric about the rotation axis and symmetric about the equatorial plane, is expressed as

$$\rho(R, Z) = \rho_0 (R/R_\star)^{-n} e^{-(Z/H)^2}. \tag{2.1}$$

In equation 2.1, R_* is the radius of the central star, ρ_0 is the gas density at the surface of the star in the equatorial plane, n is a power-law index and H is the vertical scale height of the disk. The radially-dependent function H is defined as

$$H = \left(\frac{2R^3 k T_0}{G M_* \mu_m m_H}\right)^{1/2}, \tag{2.2}$$

where M_* is the mass of the central star, μ_m is the mean molecular weight of the gas in the disk and T_0 is an assumed isothermal gas temperature used only in the initial setup

of the computational disk structure. At each location in R, the gas is taken to be in vertical hydrostatic equilibrium perpendicular to the plane of the disk set by balancing the isothermal gas pressure and the vertical component of the stellar gravitational acceleration. From Equation 2.2, the flaring of the disk with radial distance is apparent as $H \propto R^{3/2}$.

The power-law density prescription was derived empirically by Waters (1986) to explain the continuum emission signature of classical Be stars. This simple approximation for the gas density in the disk is commonly assumed in the construction of theoretical models (Porter, 1999; Okazaki, 2001; Sigut & Jones, 2007). Constraining the density distribution with IR observations, Waters et al. (1987) found values of n ranging mainly from 2.0 to 3.5, while Dougherty et al. (1994) found values ranging from 2.0 to 5.0. In the isothermal limit, the viscous disk model predicts a power-law exponent of $n = 3.5$ (Porter, 1999). While non-isothermal self-consistent calculations of the density suggest a more complex density distribution in which the power-law varies with distance from the star (Carciofi & Bjorkman, 2008), using a constant power-law allows us to readily discern the effects of changes to the state of the gas.

2.3 Radiative Transfer Code MCTRACE

The radiative transfer code MCTRACE uses Monte Carlo methods for calculating theoretical observables for the underlying model computed by BEDISK. In this section, we introduce the Monte Carlo method and describe the basic algorithm for calculating the Stokes parameters by simulating the propagation of stellar radiation through the gaseous envelope that surrounds the central star. This algorithm was transformed into the computational code used in this thesis to predict the polarization from classical Be stars. Similar Monte Carlo procedures that have been developed in the context of radiative transfer in circumstellar environments are described by, among others, Wood et al. (1996a), Lucy (1999), and Carciofi & Bjorkman (2006).

2.3.1 Monte Carlo Method

In the 1940s, physicists working on the Manhattan Project at the Los Alamos Scientific Laboratory developed simulations using random numbers to study neutron transport. This was the first modern use of what is now regarded as a Monte Carlo method, a method that has since been popularized for applications in many different fields. Aptly named for the famous casino in Monaco, Monte Carlo methods are a class of mathematical algorithms that involve the sampling of random numbers to investigate natural phenomena. More precisely, a Monte Carlo method can be considered either a numerical simulation of natural stochastic processes or a calculation of the solution of systems of equations using probabilistic methods. In either case, the method requires the use of a large amount of random numbers to produce accurate results.

Monte Carlo methods have become a prominent tool in many fields of research including those outside of the physical sciences. The breadth of their applicability and the inherent simplicity of their implementation have fuelled widespread interest in using Monte Carlo procedures to address challenging mathematical problems. The continued increase in computing capacity and the development of parallelization have allowed researchers to apply Monte Carlo algorithms in modelling physical problems of greater complexity. For very elaborate calculations, such as the evaluation of integrals in many dimensions, Monte Carlo methods can be the only effective means for finding a solution.

In astrophysics, Monte Carlo procedures are ideally suited for simulating the propagation of light in three-dimensional environments. In particular, Monte Carlo routines easily handle processes such as the scattering of photons during radiative transfer; the calculation of the polarization Stokes intensities incurs minimal added computing time (Bjorkman, 1997). In this section, we discuss some of the basic concepts associated with using Monte Carlo methods for simulating the propagation of photons through a medium with which the photons interact. While we address the specific situation of stellar radiation travelling through a circumstellar disk, the principles discussed are applicable to the transfer of radiation through other astronomical phenomena, such as the interstellar medium, reflection nebulae and planetary atmospheres.

2.3.2 Generating Random Numbers

In practice, a Monte Carlo simulation requires a sequence of numbers that is "sufficiently" random, that is to say, a sequence of numbers that is not truly random but that has values characterized by an adequate degree of randomness. Computational routines that generate deterministic sequences of numbers in imitation of true randomness are called pseudorandom number generators. All pseudorandom number generators repeat the sequence of numbers that they produce after some, preferably very long, number of numbers generated. Using pseudorandom number generators for Monte Carlo simulations is advantageous because they generate numbers rapidly and yield easily reproducible results. The pseudorandom number generator that is used in the MCTRACE code is the *ran2* routine provided by Press et al. (1992).

2.3.3 Sampling Probability Distributions

The basic premise underlying Monte Carlo simulations is the random sampling of probability distribution functions associated with the physical processes that are being modelled. To sample a quantity x_0 from the continuous probability distribution function $P(x)$, we begin with a statement of the cumulative probability distribution, $\psi(x_0)$, given as

$$\psi(x_0) = \frac{\int_a^{x_0} P(x)\mathrm{d}x}{\int_a^b P(x)\mathrm{d}x} = \xi, \tag{2.3}$$

where $\psi(x_0)$ ranges from 0 to 1 uniformly as x_0 ranges from a to b. To determine the value for x_0, a random number ξ is sampled uniformly from 0 to 1 and equation 2.3 is inverted and solved.

Sampling an Optical Depth

Our first example of sampling a probability distribution function while computing the transfer of radiation in an astronomical context is the determination of the distance that a photon travels before it interacts with the surrounding medium. We consider a beam of radiation with specific intensity I_ν, that is the energy passing through a unit area per unit time, per unit solid angle and per unit frequency. The beam is travelling through a homogeneous medium composed of scatterers and absorbers with

total number density n_d and cross-section σ. The cross-section governs the likelihood that photons in the beam will interact with the medium and has units of area. The product of the number density and the cross-section gives the fraction of photons scattered or absorbed per unit length and the product of the specific intensity and the cross-section gives the energy removed from the beam per second per frequency. Therefore, the number of photons removed from the beam owing to scattering or absorption along a path of length $\mathrm{d}l$ is $I_\nu \sigma n_d \mathrm{d}l$, and the change in intensity along that length can be expressed as

$$\mathrm{d}I_\nu = -I_\nu n_d \sigma \mathrm{d}l, \tag{2.4}$$

which yields

$$I_{\nu,L} = I_{\nu,0} e^{-n_d \sigma L}. \tag{2.5}$$

Thus, the probability that a photon travels a distance L before it interacts with the scattering and absorbing medium is

$$P(L) = e^{-n_d \sigma L}. \tag{2.6}$$

We now introduce the optical depth $\tau = n_d \sigma L$. Substituting this expression into Equation 2.6, the probability that a photon travels an optical depth τ before interacting becomes

$$P(\tau) = e^{-\tau}. \tag{2.7}$$

In a Monte Carlo treatment of radiative transfer, the length of each step of a photon's journey through a region of space is governed by the calculation of random optical depths. To sample a random value for the optical depth τ from the probability distribution function, we apply Equation 2.3, which yields

$$\xi = \frac{\int_0^{\tau_\nu} e^{-\tau} \mathrm{d}\tau}{\int_0^{\infty} e^{-\tau} \mathrm{d}\tau} = 1 - e^{-\tau_\nu}, \tag{2.8}$$

where ξ is a random number sampled uniformly from 0 to 1. Inverting Equation 2.8, we get our random optical depth

$$\tau_\nu = -\log(1 - \xi). \tag{2.9}$$

The optical depth over a distance L is defined, in general, as

$$\tau_\nu = \int_0^L n_d \sigma \mathrm{d}l. \tag{2.10}$$

For example, the optical depth over a distance L owing to electron scattering is

$$\tau_{es} = \sigma_T \int_0^L n_e \mathrm{d}l, \tag{2.11}$$

where n_e is the electron number density and σ_T is the Thomson scattering cross-section. Furthermore, the volume absorption coefficient $n_d\sigma$ can be expressed in terms of a mass absorption coefficient, κ, and the mass density of the scatterers and absorbers in the medium, ρ, through

$$n_d \sigma = \rho \kappa \tag{2.12}$$

The mass absorption coefficient, typically referred to as the opacity, can be separated into the scattering, κ_s, and absorption, $\kappa_{a,\nu}$, components. Substituting Equation 2.12 into Equation 2.10 while accounting for the two opacities yields

$$\tau_\nu = \int_0^L n_d (\kappa_{a,\nu} + \kappa_s) \rho \mathrm{d}l. \tag{2.13}$$

Determining the physical path length from Equation 2.13 using the random optical depth obtained from Equation 2.9 is a computationally demanding process that accounts for the bulk of the computing time in a typical Monte Carlo radiative transfer procedure. In order to reduce the complexity of finding L from Equation 2.13 in MCTRACE, the interaction region is discretized into a three-dimensional grid. Within each grid cell, the gas density ρ, the scattering opacity κ_s and the absorptive opacity $\kappa_{a,\nu}$ are treated as constant to simplify the calculation of the photon path lengths. Hence,

$$\tau_\nu = (\kappa_{a,\nu} + \kappa_s) \rho L, \tag{2.14}$$

and substituting in the random optical depth obtained from Equation 2.9 yields the distance travelled by the photon as determined by random sampling.

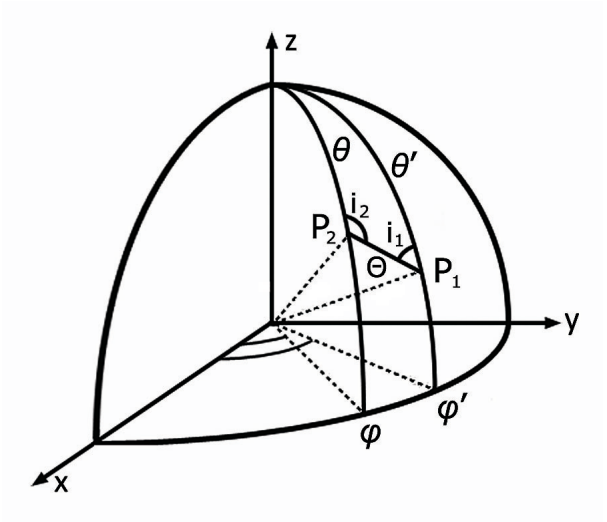

Figure 2.1: Geometry of a photon travelling in direction P_1 and scattering through the angle Θ into a new direction P_2 (reproduced from Chandrasekhar, 1960).

Sampling from an Isotropic Distribution

A basic example of random sampling is used in obtaining a direction from an isotropic distribution over 4π steradians. To obtain a direction described by $\mu = \cos\theta$ and ϕ, we sample μ uniformly in the range -1 to 1 and ϕ in the range 0 to 2π, which is simply

$$\mu = 2\xi - 1, \tag{2.15}$$

and

$$\phi = 2\pi\xi. \tag{2.16}$$

Sampling from a Scattering Matrix

Sampling a direction from an isotropic distribution is insufficient for modelling scattering processes that are not isotropic. Our computation of the Stokes intensities and the direction of scattered photons is based on the method prescribed by Chandrasekhar (1960).

We consider a photon characterized by a partial polarization described by the

Stokes parameters expressed in vector form as

$$\mathbf{S} = \begin{pmatrix} I \\ Q \\ U \\ V \end{pmatrix}. \tag{2.17}$$

The Stokes intensities are required in the observation frame of reference. Therefore, updating the Stokes vector during a scattering event means rotating the vector into and out of the frame of reference of the moving photon. The coordinate system described by Chandrasekhar is illustrated in Figure 2.1. First, we rotate the vector into the frame of reference of the moving photon using a Mueller matrix, $\mathbf{L}(\eta)$. Next, we apply the scattering matrix, $\mathbf{R}(\Theta)$, where Θ is the angle between the incident and scattered radiation. Finally, we rotate the Stokes vector back into the original frame of reference, again using a Mueller matrix. Thus, a photon described by the Stokes vector $\mathbf{S}$ and travelling in the direction (θ,ϕ) scatters into a new direction (θ',ϕ') and is now described by the Stokes vector

$$\mathbf{S}' = \mathbf{L}(\pi - i_2)\mathbf{R}\mathbf{L}(-i_1)\mathbf{S}. \tag{2.18}$$

The Mueller matrix, $\mathbf{L}(\eta)$, is defined as

$$\mathbf{L}(\eta) = \begin{bmatrix} 1 & 0 & 0 & 0 \\ 0 & \cos 2\eta & \sin 2\eta & 0 \\ 0 & -\sin 2\eta & \cos 2\eta & 0 \\ 0 & 0 & 0 & 1 \end{bmatrix}. \tag{2.19}$$

The scattering matrix, $\mathbf{R}(\Theta)$, where Θ is the scattering angle measured from the direction of the incident photon, is defined as

$$\mathbf{R}(\Theta) = A \begin{bmatrix} P_{11} & P_{12} & P_{13} & P_{14} \\ P_{21} & P_{22} & P_{23} & P_{24} \\ P_{31} & P_{32} & P_{33} & P_{34} \\ P_{41} & P_{42} & P_{43} & P_{44} \end{bmatrix}. \tag{2.20}$$

In the case of electron scattering, the coefficient A and the elements of the scattering matrix are

$$\begin{aligned} A &= \tfrac{3}{4} \\ P_{11} = P_{22} &= \cos^2\Theta + 1 \\ P_{12} = P_{21} &= \cos^2\Theta - 1 \\ P_{33} = P_{44} &= 2\cos\Theta \end{aligned} \tag{2.21}$$

and all other elements of the matrix are zero. Therefore, the scattering matrix is

$$\mathbf{R}(\Theta) = \frac{3}{4}\begin{bmatrix} \cos^2\Theta + 1 & \cos^2\Theta - 1 & 0 & 0 \\ \cos^2\Theta - 1 & \cos^2\Theta + 1 & 0 & 0 \\ 0 & 0 & 2\cos\Theta & 0 \\ 0 & 0 & 0 & 2\cos\Theta \end{bmatrix}. \tag{2.22}$$

Now, the I Stokes parameter in the photon's reference frame can be computed using Equation 2.18 as

$$I'(\Theta, i_1) = (\cos^2\Theta + 1)I + (\cos^2\Theta - 1)\cos 2i_1 Q - 2\cos\Theta \sin 2i_1 U. \tag{2.23}$$

Before calculating the updated Stokes intensities and rotating the vector back to the initial reference frame, we sample the angles Θ and i_1 that alter the direction of the photon from P_1 to P_2, as illustrated in Figure 2.1. We use the rejection method to sample from the exact probability distribution of the intensity of the scattered radiation. In brief, to sample a value x_0 from $P(x)$ with a known maximum over a to b, we sample x_0 from a uniform distribution between a and b, we sample y_0 from a uniform distribution between 0 and the maximum of $P(x)$ and we reject any value of x_0 for which $y_0 > P(x_0)$.

Thus, we sample Θ and i_1 from an isotropic distribution and calculate $I'(\Theta, i_1)$ from equation 2.23. We sample I_0 from $I_0 = \xi I_{max}$, where I_{max} is the maximum intensity of the scattered radiation. If $I_0 < I'(\Theta, i_1)$, then Θ and i_1 satisfy the rejection method and we can proceed to the next step of the calculation. Otherwise, we must repeat the process until we obtain values that satisfy the rejection criteria. Once satisfied, we update the values of the Stokes intensities in the observer's frame and determine the direction of the scattered photon.

2.3.4 Computational Domain

The BEDISK code assumes that the circumstellar disk is axisymmetric about the rotational axis and symmetric about the midplane. In other words, the computational domain of BEDISK consists of a grid in R and Z, with R the radial distance from the rotation axis, and Z the vertical distance perpendicular to the equatorial plane. The MCTRACE code extends this domain to three-dimensions with the introduction of an azimuthal coordinate Φ such that any location in the disk can be labelled, using conventional representation for cylindrical coordinate systems, as (R, Φ, Z). Typically, our disk models use 60 radial grid points extending from the stellar surface outward to 100 stellar radii. The models use 60 vertical grid points (30 grid points above and 30 grid points below the midplane) and 72 azimuthal grid points. While the azimuthal grid points are equally-spaced, the points on the radial and vertical axes are predetermined (in the BEDISK initialization of the model) and generally spaced for better sampling of the highest density regions. Our choice of grid points is somewhat arbitrary, however we did perform comparisons with models using larger numbers of grid points. We concluded that our current initial grid provides sufficient sampling to effectively predict our desired observables.

2.3.5 Algorithm

Before outlining the essential steps for simulating the propagation of light through the circumstellar environment, we must describe the individual units under consideration in this treatment of radiative transfer. The simulated elements of light are monochromatic *photon packets* of frequency ν quantized by a total energy $E_\nu = n_\nu h\nu$, where n_ν is the number of photons contained in the packet and $h\nu$ is the energy of each photon. We take all photon packets to have equivalent total energy E_0 such that when a photon packet of frequency ν is absorbed, it is re-emitted with frequency ν' and energy $E_\nu = E_{\nu'} = E_0$. This enforces the balance between the rates of absorption and emission in accordance with the radiative equilibrium solution computed by BEDISK. The energy of the photon packets can be related to the total radiant energy of the system

by assuming an arbitrary simulation time Δt such that

$$NE_0 = L_* \Delta t, \tag{2.24}$$

where L_* is the luminosity of the system and N is the total number of photon packets used in the simulation. Each photon packet is characterized by a partial polarization described by the Stokes parameters and represented with the initial Stokes vector as

$$\mathbf{S} = \begin{pmatrix} 1 \\ 0 \\ 0 \\ 0 \end{pmatrix}. \tag{2.25}$$

Hereafter, we refer to the photon packets simply as *photons*.

For each photon in the simulation, MCTRACE executes the following procedure:

1. The photon is assigned an initial location on the stellar surface along with a direction of propagation and frequency. In general, each of these properties are selected by randomly sampling the appropriate probability distribution functions. For example, the probability distribution for direction and frequency are given by
$$\frac{\mathrm{d}P}{\mathrm{d}\Omega\,\mathrm{d}\nu} \propto \mu I_\nu(\mu), \tag{2.26}$$
where μ is the cosine of the angle between the radial direction and the direction of the emitted photon. In practice, it is more efficient for MCTRACE to predetermine the numbers of packets emitted from each stellar grid location for each frequency and assign the initial properties of each photon accordingly.

2. A random optical depth τ_ν is sampled and the photon travels a corresponding distance L, as described in Section 2.3.3. If this distance is greater than the distance to the nearest cell boundary along its current direction of travel, the photon crosses the cell boundary and a new random optical depth is calculated. This is consistent with the fact that the probable distance travelled between interactions is always $\tau_\nu = 1$ regardless of the distance the photon has already travelled along its current trajectory (Lucy, 1999).

3. If the photon has not exited the interaction region once it has travelled a distance L, is either scattered or absorbed. The photon is scattered if

$$\xi \leq \frac{\kappa_s}{\kappa_{a,\nu} + \kappa_s}, \tag{2.27}$$

and the direction of the scattered photon and the Stokes vector are updated following the procedure described in Section 2.3.3. Otherwise, the photon is absorbed and re-emitted with a probability

$$\frac{\mathrm{d}P}{\mathrm{d}\Omega\,\mathrm{d}\nu} \propto j_\nu, \tag{2.28}$$

where j_ν is the local emissivity of the gas.

4. The photon is tracked (i.e. steps 2 and 3 are repeated) until it exits the interaction region, after which MCTRACE records the values of interest and bins them according to their angle of departure and frequency.

2.3.6 Testing

Before using any computational code for its intended purpose, careful testing is required to ensure the correctness of the implementation and the validity of the technique. In applying a code to simplified cases, comparisons can generally be made to accurate analytic solutions. In applying a code to cases with greater complexity, comparisons must be made to the numerical results computed using other codes. We tested MCTRACE by comparing its output to the analytic results for Rayleigh-scattering plane-parallel atmospheres and to numerical results for single-scattering plus attenuation and multiple-scattering models of circumstellar disks. Furthermore, we performed *ad hoc* simulations designed to ensure that specific aspects of the code operated as intended.

The cases for which analytic solutions can be derived are limited but nonetheless provide excellent benchmarks for testing the basic functioning of our code. We simulated the transmission of light through a Rayleigh-scattering, plane-parallel atmosphere. The analytic solution of the radiative transfer equations describing the intensity and polarization of the radiation emerging from such an atmosphere were

introduced by Chandrasekhar (1960). Full tables of updated solutions have been published as a reference standard (Coulson et al., 1960) with revised, high-precision tables recently provided by Natraj et al. (2009). As the primary function of MCTRACE is the calculation of the Stokes intensities from the transmission of light through a scattering medium, this is an ideal problem for testing the code.

In the Rayleigh-scattering atmosphere simulation, the scattering medium is represented by a homogeneous, plane-parallel slab parametrized by a vertical optical depth τ_{pp}. The slab is illuminated from above by parallel, unpolarized radiation. The direction of the light is given by the cosine of the incident zenith angle, μ_0, with the incident azimuth angle set to zero. The direction of observation above or below the atmosphere is expressed with the cosine of the viewing zenith angle μ and the viewing azimuth angle ϕ. We ran this simulation for varying optical depths and compared the results for different incident and viewing directions. The comparisons showed consistent agreement between our calculations and the analytic solutions, as illustrated by the examples in Figures 2.2 and 2.3.

Next, we compared the output of MCTRACE to numerical results from previous efforts at predicting the fraction of linearly polarized light that arises from electron scattering in circumstellar disks. Many previous theoretical studies were limited to calculating the polarization from single-scattering while including the attenuation of light from absorption and scattering. We compared the output from our Monte Carlo method to that from an updated version of the procedure used by Poeckert & Marlborough (1978), who modelled observations of the classical Be star γ Cas with reasonable success considering their computational limitations. The results of this comparison are presented in Chapter 3. In short, the comparison between MCTRACE and the PM procedure showed excellent agreement. Given that the basic operation of the Monte Carlo code is unaffected by enforcing the special case of single-scattering, this comparison provides assurance that MCTRACE functions as intended.

In addition, we compared our predictions to the results presented by Wood et al. (1996b) who also used a Monte Carlo code to calculate the degree of polarization arising from multiple-scattering in a geometrically-thin, equatorial disk. They used a varying albedo to simulate all the absorptive opacity sources in the envelope. We modified our code to make a similar determination for whether a photon is scattered

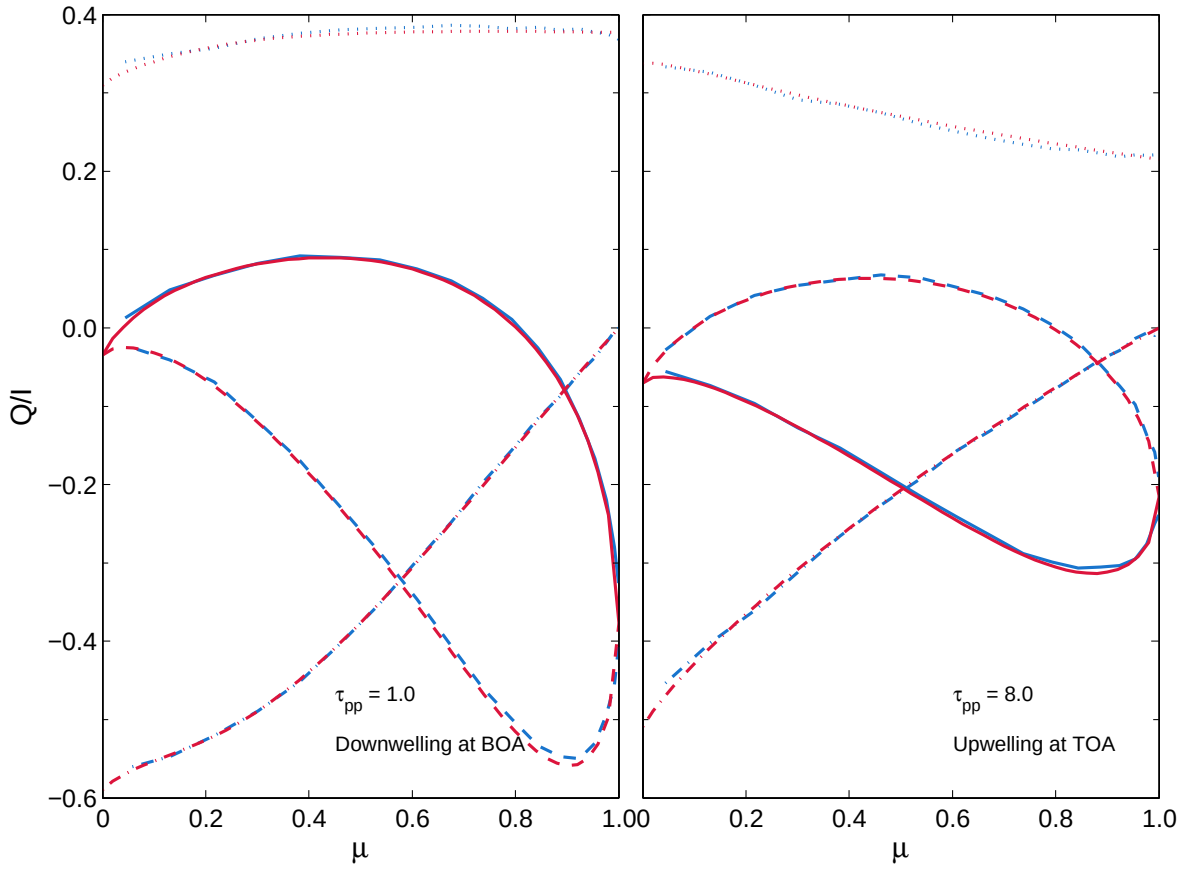

Figure 2.2: Normalized Q Stokes parameter as a function of μ emerging from a Raleigh-scattering, plane-parallel atmosphere. The panel on the left shows the downwelling radiation at the bottom of the atmosphere of optical depth $\tau_{pp} = 1.0$, while the panel on the right shows the upwelling radiation at the top of the atmosphere of optical depth $\tau_{pp} = 8.0$. The Q/I values are plotted for $\mu_0 = 1.0$ (dashed-dotted, equivalent at any viewing azimuth angle) and for $\mu_0 = 0.5$ with $\phi = 0$ (solid), $\phi = 90$ (dotted), and $\phi = 180$ (dashed). The red lines represent the values calculated by Natraj et al. (2009) and the blue lines show the values computed by MCTRACE.

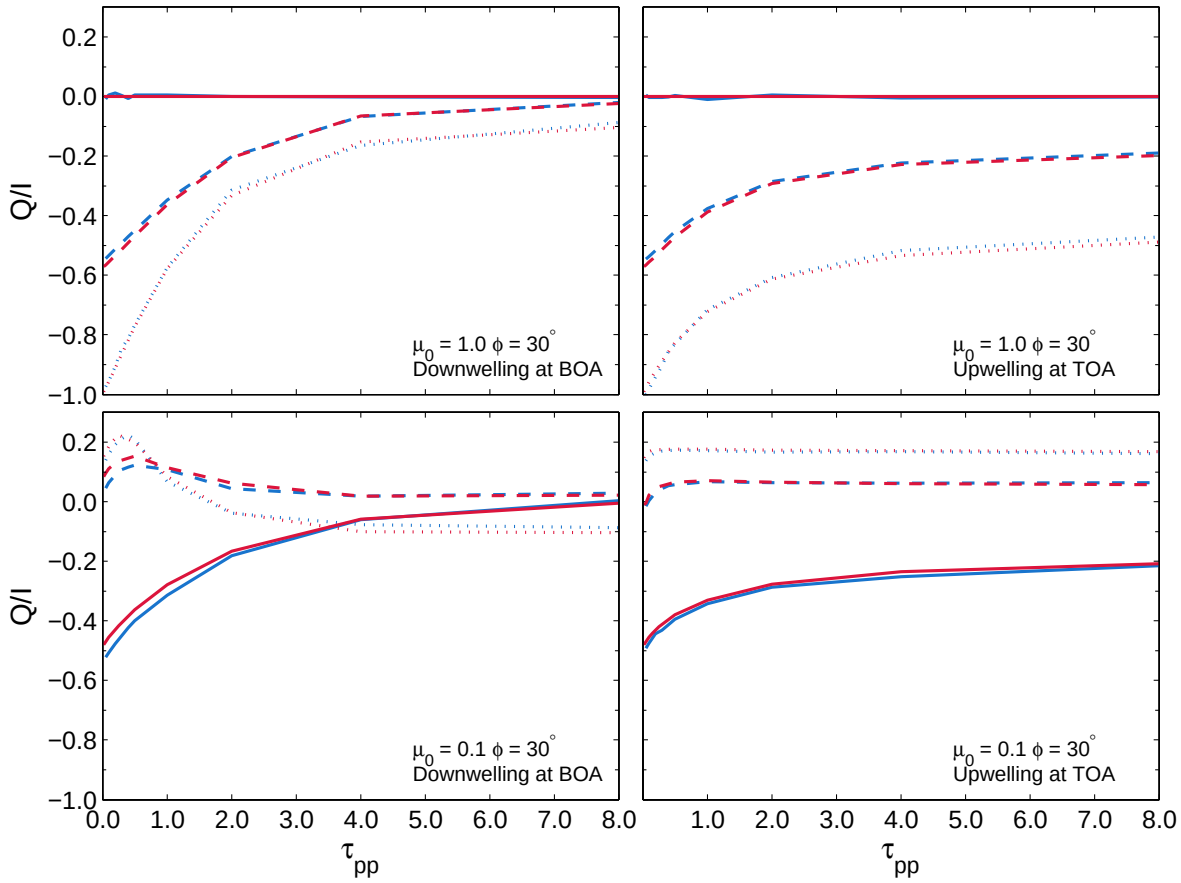

Figure 2.3: Normalized Q Stokes parameter as a function of τ_{pp} emerging from a Raleigh-scattering, plane-parallel atmosphere for $\phi = 30°$. The panels on the left show the downwelling radiation at the bottom of the atmosphere, while the panels on the right show the upwelling radiation at the top of the atmosphere of optical depth. The Q/I values are plotted for $\mu_0 = 1.0$ (top) and $\mu_0 = 0.1$ (bottom) with $\mu = 1.0$ (solid), $\mu = 0.52$ (dashed), and $\mu = 0.02$ (dotted). The red lines represent the values calculated by Natraj et al. (2009) and the blue lines show the values computed by MCTRACE.

or absorbed upon each interaction. Our comparison showed qualitatively similar results, with quantitative differences in the polarization level attributable to differences in the configurations of the circumstellar gas.

Lastly, we verified the functioning of our code by constructing arbitrary configurations for which the behaviour of the Stokes intensities is easily understood in order to ensure that the scattering computation yields correct geometric solutions. For example, a simple 45° wedge of dense, isothermal gas, viewed pole-on, should produce a circle in a $q-u$ plot when rotated about the rotation axis of the star. When such a system is viewed at a high inclination, the polarization is dominated by scattering in the plane of the disk and should favour, according to the geometry established in Chapter 1, the q intensity with an asymmetry in the u intensity caused by the wedge's position in front or in back of the star. These examples are illustrated in the top row of Figure 2.4. Similarly, a pair of diametrically-opposed wedges should again produce a circle in the $q-u$ plot. However, due to the symmetric nature of the configuration, there should be no asymmetry in the u intensity when viewed at higher inclinations. These examples are illustrated in the bottom row of Figure 2.4. *Ad hoc* simulations of this nature provide reasonable confirmation that our calculation of the Stokes intensities produces the expected qualitative results.

2.3.7 Summary

We use computational radiative transfer codes to model the circumstellar environments of classical Be stars so that we can interpret observations and gain insight into the physical and dynamical nature of these systems. We have developed a Monte Carlo computational procedure, MCTRACE, capable of producing synthetic spectra for the Stokes intensities using a self-consistent solution for the temperature structure of the gaseous circumstellar disk. We have tested this code using comparisons to analytic and numerical solutions for similar problems. In the following chapters, we employ MCTRACE to investigate the continuous linear polarization signature of classical Be stars.

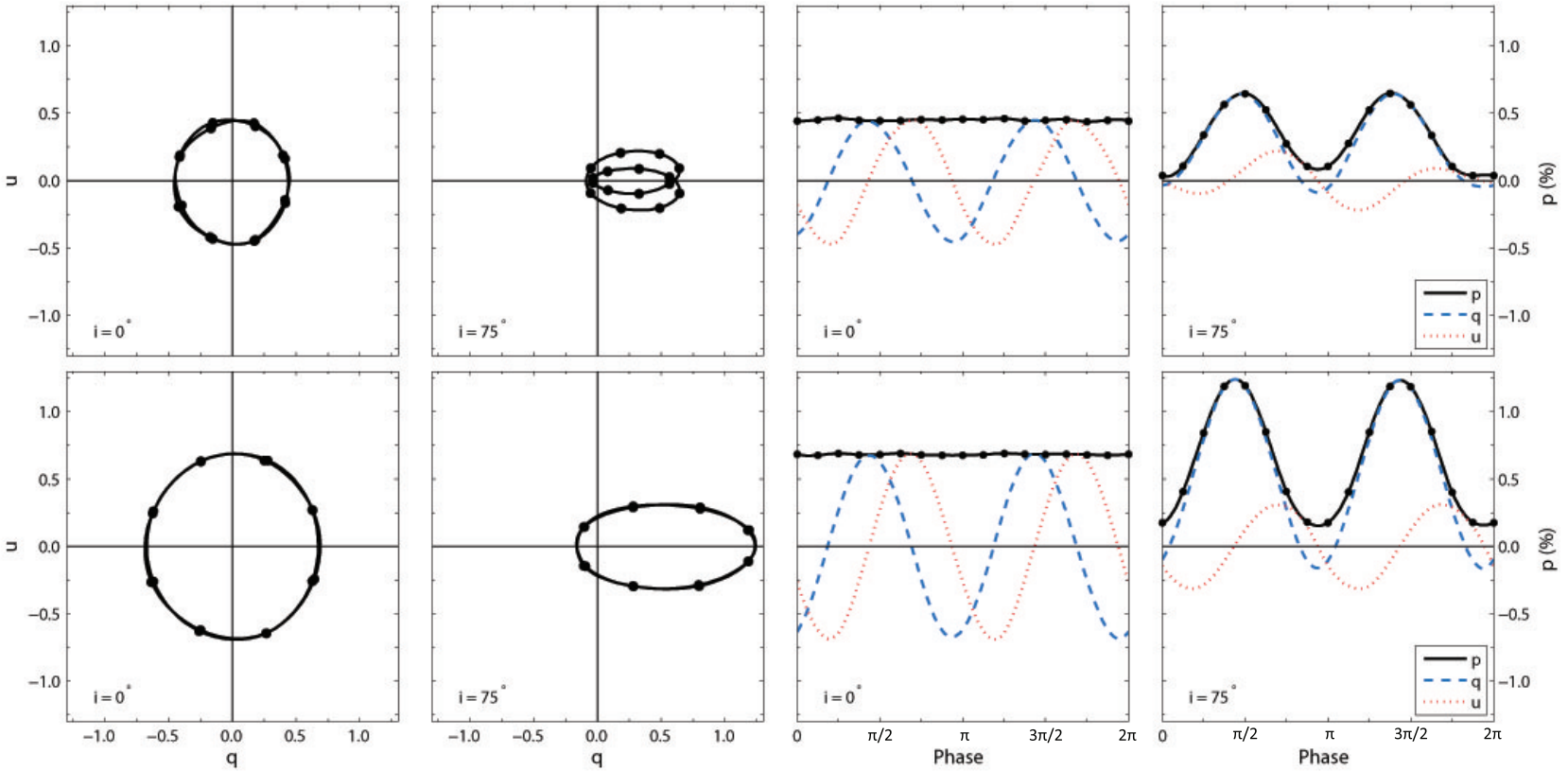

Figure 2.4: Linear polarization for test density configurations viewed at inclination $0°$ and $75°$. The top row shows the polarization for a $45°$ wedge of dense gas. The bottom row shows the polarization for two diametrically-opposed $45°$ wedges of gas. The first two columns from the left show the polarization in $q - u$ plots and the last two columns show the polarization as a function of the viewing phase.

Bibliography

Ahmed, A., & Sigut, T. A. A. 2012, ApJ, 744, 191

Bjorkman, J. E. 1997, in Stellar Atmospheres: Theory and Observations, ed. J. P. De Greve, R. Blomme & H. Hensberge, (Berlin: Springer Verlag) , 239

Brown, J. C. & McLean, I. S. 1977, A&A, 57, 141

Carciofi, A.C., & Bjorkman, J. E. 2006, ApJ, 639, 1081

Carciofi, A.C., & Bjorkman, J. E. 2006, ApJ, 684, 1374

Carciofi, A. C., Miroshnichenko, A. S., Kusakin, A. V., Bjorkman, J. E., Bjorkman, K. S., Marang, F., Kuratov, K. S., García-Lario, P., Calderón, J. V. Perea, Fabregat, J., & Magalhães, A. M. 2006, ApJ, 652, 1617

Clarke, D. 2010, Stellar Polarimetry, (1st ed.; Germany: Wiley-VCH)

Clarke, D., & Bjorkman, K. S. 1998, A&A, 331, 1059

Chandrasekhar, S. 1960, Radiative Transfer (1st ed.; New York: Dover)

Coulson, K. L., Dave, J. V., & Sekera, Z. 1960, Tables Related to Radiation Emerging From a Planetary Atmosphere With Rayleigh Scattering (Berkeley, CA: Univ. California Press)

Coyne, G.V., & Kruszewski, A. 1969,AJ, 74, 528

Dougherty, S. M., Waters, L. B. F. M., Burki, G., Coté, J., Cramer, N., van Kerkwijk, M. H., & Taylor, A. R. 1994, A&A, 290, 609

Draper, Z. H., Wisniewski, J. P., Bjorkman, K. S., Haubois, X., Carciofi, A. C., Bjorkman, J. E., Meade, M. R., & Okazaki, A. 2011, ApJ, 728, 40

Halonen, R. J., Jones, C. E., Sigut, T. A. A., Zavala, R. T., Tycner, C., Levine, S. E., Luginbuhl, C. B., Vlieg, N., Vrba, F. J. 2012, PASP, 120, 498

Halonen, R. J., & Jones, C. E. 2013, ApJ, 765, 17

Halonen, R. J., Mackay, F. E., & Jones, C. E. 2013, ApJS, 204, 11

Grzenia, B. J., Tycner, C., Jones, C. E., Rinehart, S. A., van Belle, G. T., & Sigut, T. A. A. 2013, AJ, 145, 141

Jones, C. E., Sigut, T.A.A., & Marlborough, J. M. 2004, MNRAS, 352, 841

Jones, C. E., Tycner, C., Sigut, T. A. A., Benson, J. A., & Hutter, D. J. 2008, ApJ, 687, 598

Jones, C. E., Sigut, T. A. A, & Porter, J. M. 2008, MNRAS, 386, 1922

Jones, C. E., Molak, A., Sigut, T. A. A., de Koter, A., Lenorzer, A., & Popa, S. C. 2009, MNRAS, 392, 383

Kurucz, R. F. 1993, Kurucz CD-ROM No. 13. Cambridge, Mass: Smithsonian Astrophysical Observatory

Lucy, L. B. 1999, A&A, 344, 282

Marlborough, J. M. 1969, ApJ, 156, 135M

Mackay, F. E., Elias, N. M., Jones, C. E., & Sigut, T. A. A. 2009, ApJ, 704, 591

McDavid, D. 1998, PASP, 758, 494

McGill, M. A., Sigut, T. A. A., & Jones, C. E. 2011, ApJ, 743, 111

McGill, M. A., Sigut, T. A. A., & Jones, C. E. 2011, ApJS, 204, 2

Millar, C. E., & Marlborough, J. M. 1998, ApJ, 494, 715

Millar, C. E., & Marlborough, J. M. 1999, ApJ, 516, 276

Millar, C. E., & Marlborough, J. M. 1999, ApJ, 526, 400

Natraj, V., Li, K., & Yung, Y.L. 2009, ApJ, 691, 1909

Okazaki, A. T. 2001, PASJ, 53, 119

Osterbrock, D. E. 1989, Astrophysics of Gaseous Nebulae and Active Galactic Nuclei (Mill Valley: University Science Books)

Poeckert, R., & Marlborough, J.M. 1978, ApJ, 220, 940

Porter, J. M. 1999, A&A, 348, 512

Porter, J. M., & Rivinius, T. 2003, PASP, 115, 1153

Press, W. H., Teukolsky, S. A., Vetterling, W. T., & Flannery, B. P. 1992, Numerical Recipes in FORTRAN (Cambridge: University Press),

Quirrenbach, A., Bjorkman, K. S., Bjorkman, J. E., Hummel, C. A., Buscher, D. F., Armstrong, J. T., Mozurkewich, D., Elias, N. M. II, & Babler, B. L. 1997, ApJ, 479, 477

Sigut, T.A.A. & Jones, C.E. 2007, ApJ, 668, 481

Sigut, T. A. A. & Patel, P. 2013, ApJ, 765, 41

Silaj, J., Jones, C. E., Tycner, C., Sigut, T. A. A. & Smith, A. D. 2010, ApJS, 187, 228

Tycner, C., Jones, C. E., Sigut, T. A. A., Schmitt, H. R., Benson, J. A., Hutter, D. J., & Zavala, R. T. 2008, ApJ, 689, 461

Waters, L. B. F. M. 1986, A&A, 162, 121

Waters, L. B. F. M., Coté, J., & Lamers, H. J. G. L. M. 1987, A&A, 185, 206

Wisniewski, J. P., Draper, Z. H., Bjorkman, K. S., Meade, M. R., Bjorkman, J. E., & Kowalski, A. F. 2010, ApJ, 709, 1306

Wood, K., Bjorkman, J. E., Whitney, B. A., & Code, A. D. 1996, ApJ, 461, 828

Wood, K., Bjorkman, J. E., Whitney, B. A., & Code, A. D. 1996, ApJ, 461, 847

Wood, K., Bjorkman, K. S., & Bjorkman, J. E. 1997, ApJ, 477, 926

Chapter 3

Computing the Continuum Polarization from Thomson Scattering in Gaseous Circumstellar Disks

A version of this chapter has been published in The Astrophysical Journal Supplement as Halonen, R. J., Mackay, F. E., & Jones, C. E., 2013, ApJS, 204, 11. In this chapter, Halonen & Jones 2013 refers to Chapter 4 of this thesis.

3.1 Introduction

Classical Be stars are rapidly rotating B-type stars surrounded by thin, equatorial, decretion disks of gas. The radiation emitted by these hot massive stars interacts with the enveloping circumstellar gas to produce variable observational characteristics that peculiarize these objects. While classical Be stars are identified principally by prominent hydrogen emission lines and excess continuum emission, these rapid rotators also typically exhibit a detectable linear polarization signature in their emitted light. The linearly polarized light results from the Thomson scattering of stellar radiation off of free electrons in the non-spherically symmetric distribution of gas that surrounds these stars (Coyne & Kruszewski, 1969). A distinct wavelength-dependence to the polarization spectrum arises from sources of absorptive opacity in the scattering region (see, for example, Clarke & Bjorkman, 1998). Observations such as the multi-band po-

larimetry collected by McDavid (1998) have illustrated variability in the polarization levels of classical Be stars. Because the mechanisms that generate and shape the polarization spectrum are intrinsic to the envelope, the observed signature is a distinct feature that characterizes the scattering material itself. Hence, polarimetry provides a means for probing the scattering environment of classical Be stars without having to spatially resolve the object.

Detailed modelling of observations of classical Be stars, using data obtained through techniques such as photometry, spectroscopy and interferometry, have contributed greatly to our understanding of the nature of their circumstellar environment (see the most recent review by Porter & Rivinus, 2003). Polarimetry also constitutes a key observing method for studying classical Be stars as the properties of the polarized light from scattering in the ionized disk can yield valuable information. Notably, Quirrenbach et al. (1997) combined the orientation from the polarization position angle with optical interferometric observations to ascertain the geometric structure of the circumstellar disk. Recently, Wisniewski et al. (2010) developed interesting observational disk diagnostics using the spectropolarimetric features of classical Be stars to study the formation and dissipation of the disk. In the near future, higher resolution observations and innovative observing techniques, such as interferometric polarimetry (Mackay et al., 2009), will further increase the relevance of polarization measurements with respect to the study of classical Be stars.

These successes underlie the importance of accurately reproducing the correct linear polarization levels with well-tested theoretical calculations. For the simplest case of an optically thin, axisymmetric envelope illuminated by a point light source, Brown & McLean (1977) produced a theoretical relation between the polarization and inclination angle. They found that the polarization was $\propto \sin^2 i$. The analytic problem becomes complicated with the inclusion of absorption and emission by the circumstellar gas and with consideration for the finite stellar disk and occultation of the circumstellar material by the star. The polarization as a function of inclination then becomes a complex, model-dependent expression. Detailed computational modelling efforts began with the work of Poeckert & Marlborough (1978), hereafter PM. PM used a radiative transfer code to predict the polarization of the classical Be star γ Cas. The complexity of the problem and the computational limitations at the time meant that PM's

models were more or less *ad hoc*, yet they were remarkably successful in reproducing the polarization and other observables for γ Cas (Millar & Marlborough, 1998). Since then, more sophisticated computational procedures have been used to reproduce the polarization levels of Be stars (see, for example, Wood, Bjorkman & Bjorkman, 1997; Carciofi et al., 2006).

Our current understanding of classical Be stars lacks a clear physical description of the formation and dissipation of the disks of gas surrounding these objects. Theoretical endeavours to study these enigmatic systems attempt to identify the physical conditions and mechanisms associated with stellar mass-loss and angular momentum transfer by comparing observations to realistic models. The polarimetric properties of classical Be stars provide crucial diagnostics in investigating the evolution of circumstellar environments (Draper et al., 2011; Halonen & Jones, 2013). Reproducing polarimetric observations necessitates careful consideration of the state of the circumstellar material in which stellar radiation becomes scattered or absorbed and re-emitted. Accurate computation of local electron densities and gas temperatures are crucial. Fortunately, sophisticated non-LTE radiative transfer models exist that can perform the necessary calculations (Carciofi & Bjorkman, 2006; Sigut & Jones, 2007).

In this paper, we use models from the non-LTE radiative transfer code of Sigut & Jones (2007), implemented with a pair of independently-developed scattering codes, to investigate the computation of the polarization in gaseous disks. We bridge the gap between the pioneering work of PM and current-day modelling of polarimetric observables, providing a needed theoretical perspective on Thomson scattering in optically thin and thick gaseous disks. This work provides insight into the technical aspects of computational methods for calculating the observables from scattering in circumstellar environments. We also emphasize the importance of using multiple-scattering calculations when considering systems with optically thick circumstellar disks. We have organized this paper as follows: Section 3.2 briefly summarizes the computational procedures relevant to this work; Section 3.3 describes the technical improvements over the modelling efforts of PM and demonstrates their effect on the polarization prediction; Section 3.4 discusses the comparison of the single-scattering and multiple-scattering techniques; finally, Section 3.5 summarizes our results.

3.2 Computational Procedures

The computational procedures that we have developed to calculate the polarization from scattering in gaseous envelopes of classical Be stars use an underlying detailed model of the circumstellar disk produced by the non-LTE radiative transfer code BEDISK developed by Sigut & Jones (2007). This computational code solves the equations of radiative transfer, statistical equilibrium and radiative equilibrium to provide a self-consistent calculation of the thermal structure of the circumstellar disk. The code employs an ATLAS9 LTE stellar atmosphere (Kurucz, 1993) to compute the direct photoionizing stellar radiation field at each grid location in the disk. The code balances the heating and cooling rates using the computed atomic level populations for a user-specified set of atoms and ions. The modelled disk is assumed to be axisymmetric about the stellar rotation axis, and symmetric about the midplane. The density distribution of gas in the envelope at coordinates (R, Z), where R is the radial distance from the stellar rotation axis and Z is the distance above the equatorial midplane, is specified by

$$\rho(R, Z) = \rho_0 (R)^{-n} e^{-(\frac{Z}{H})^2}. \tag{3.1}$$

Here, ρ_0 is the gas density at the inner edge of the disk, n is the power-law index and H is a vertical scale height which depends on an initial isothermal disk temperature. At each R, the gas is taken to be in vertical hydrostatic equilibrium perpendicular to the plane of the disk.

We have developed two computational methods for calculating the fractional polarization of the emergent intensity from the ionized circumstellar medium using the atomic level populations and gas temperature structure computed by the BEDISK code. The first method is analogous to the procedure described by PM. The net polarization of the disk is determined by integrating the Stokes parameters at individual grid points along lines of sight through the disk, with the results summed over the projected area of the disk on the sky. This method assumes single electron scattering and includes an attenuation factor to account for absorption and the scattering of photons out of the line of sight. The second technique employs random sampling of probability distribution functions to simulate the propagation of individual photons through the circumstellar medium. This Monte Carlo procedure computes the Stokes parameters

by following the path of each photon through the gas and resolving the interactions that occur between the photon and the medium. Photons may undergo multiple occurrences of scattering and/or absorption and re-emission before eventually exiting the interaction region.

3.3 Comparisons to Poeckert & Marlborough

Given the desire to understand the evolution of the circumstellar gas, it is essential for computational models to accurately determine the state of the gas, particularly the ionization levels, in addition to providing adequate sampling of the density distribution. In both of these regards, modern non-LTE radiative transfer methods have made significant advances since the work presented by PM. The most notable improvement to models of classical Be stars introduced by radiative transfer codes such as BEDISK is the self-consistent calculation of the thermal structure of the disk. This is accomplished by enforcing radiative equilibrium throughout the disk: at each computational grid point, the gas temperature is determined by balancing the local heating and cooling rates as determined by the relevant physical processes. In contrast, PM simply assumed an isothermal disk, an assumption that greatly affects the predicted observables (Millar & Marlborough, 1999). Furthermore, while PM restricted themselves to a disk of pure hydrogen, BEDISK is capable of running models for a realistic chemical composition, including up to 30 levels of hydrogen, compared to the five used by PM. These improvements are crucial in determining the non-isothermal structure of the disk; thus they affect the level populations and the number of scatterers present in the disk and influence the predicted polarization.

Several additional differences exist between the radiative transfer codes of PM and Sigut & Jones. First of all, the two codes employ different techniques for the treatment of line radiation. The BEDISK code employs an escape probability approximation in which the single-flight static escape probability at a given point is calculated using the optical depth from the grid point to the closest vertical edge of the disk assuming complete redistribution in the line. In contrast, PM employed specific *cases* based on whether the envelope is optically thin or thick for a series of lines. For a description of these *cases*, see Marlborough (1969) or Millar & Marlborough (1998). Next, the two

procedures assume different density distributions. The BEDISK code uses the density distribution expressed in Equation 3.1. In contrast, PM determined the radial density distribution in the equatorial plane by assuming both the density at one location and a radial velocity distribution, and then implementing the equation of continuity. They then assumed vertical hydrostatic equilibrium at one location and used this to calculate the vertical densities throughout the disk. Lastly, updated stellar atmosphere models and limb darkening laws, critical for accurately determining the photoionizing radiation field at each location in the disk, have been incorporated into BEDISK.

Our access to PM's code provides us with a unique opportunity to investigate the effect that limitations on certain computational parameters have on the results. In addition, it allows us to directly compare PM's results with those obtained using the BEDISK code. We investigated the effect that the number of hydrogen levels, the number of sectors on the star, the thermal structure of the gaseous disk, and the chemical composition in the disk have on the resultant polarization levels. This work has allowed us to consider the effect of various parameters on polarization predictions and to understand which simplifications yield the most significant changes in the results.

3.3.1 Effects of the Improvements

We used the PM and BEDISK codes to construct baseline models for comparison. In establishing a baseline model between the two codes, we ensured that the density structure employed by BEDISK was consistent with that used by PM. We note that the version of the PM code available to us has been slightly modified since the analysis of Poeckert & Marlborough (1978). As such, the level populations that we obtained using our version of the PM code are not in exact agreement with those published in the 1978 paper, although they are quite similar. We used the same parameters for the central star as PM, given in Table 3.1. The polarization levels using BEDISK were calculated using the integration along lines of sight method.

As a starting point, we computed the BEDISK solution for an isothermal disk of 24 by 4 grid points, using a pure hydrogen chemical composition for the disk with the first five atomic levels included, and using 13 sectors on the star. These computational parameters match those used in PM's model. We note that a typical BEDISK model

Table 3.1: Stellar Parameters for γ Cassiopeia

Property	Value
Spectral Type	B0 IVe
Radius	10.0 $R_\odot$
Mass	17.0 $M_\odot$
Luminosity	3.4×10^4 $L_\odot$
$T_{\rm eff}$	25 000 K
$\log(g)$	3.50 $\mathrm{cm\,s^{-2}}$

uses uses $\sim$ 60 radial and 30 vertical points, with the visible stellar surface divided into into $\sim$ 200 patches. The combined effect of the updated stellar model and limb darkening law, as well as any other intrinsic differences between the two codes, on the degree of polarization for a representative model is illustrated in Figure 3.1. Clearly, the polarization predictions from the two codes are not dramatically different in this instance. For the remainder of the comparisons, we increased the number of grid points until a convergence of the solution was obtained. The updated baseline model is shown in Figure 3.2A.

The first improvement was an increase in the number of hydrogen levels from 5 to 15. As depicted in Figure 3.2B, this change results in an increase in the continuum polarization at all wavelengths. This increase arises because the change in level populations results in a decrease in the overall absorptive opacity in the disk. Next, we replaced the 13 sectors on the star with a grid of 19 points in θ_* by 19 in ϕ_*, where θ_* and ϕ_* correspond to the usual spherical coordinates. This change lowered the polarization level at all wavelengths, as shown in Figure 3.2C. Two factors contribute to this decrease. The most significant factor is an increase in the accuracy of the integration due to finer stellar grid; with a rough grid of fewer points, the integration over the visible stellar surface produces a larger angular size for the star than is actually present. The artificially enlarged stellar disk causes a higher value for each of the Stokes parameters at all points in the disk. The second factor is improved sampling near the edge of the visible stellar disk where the stellar intensity is reduced due to the limb darkening effect. The limited stellar grid results in an higher integrated intensities, which contributes to inflated values for each of the Stokes parameters.

The previous models assumed an isothermal disk with a temperature of 20000 K. This assumption is generally not valid for the circumstellar disks surrounding classical

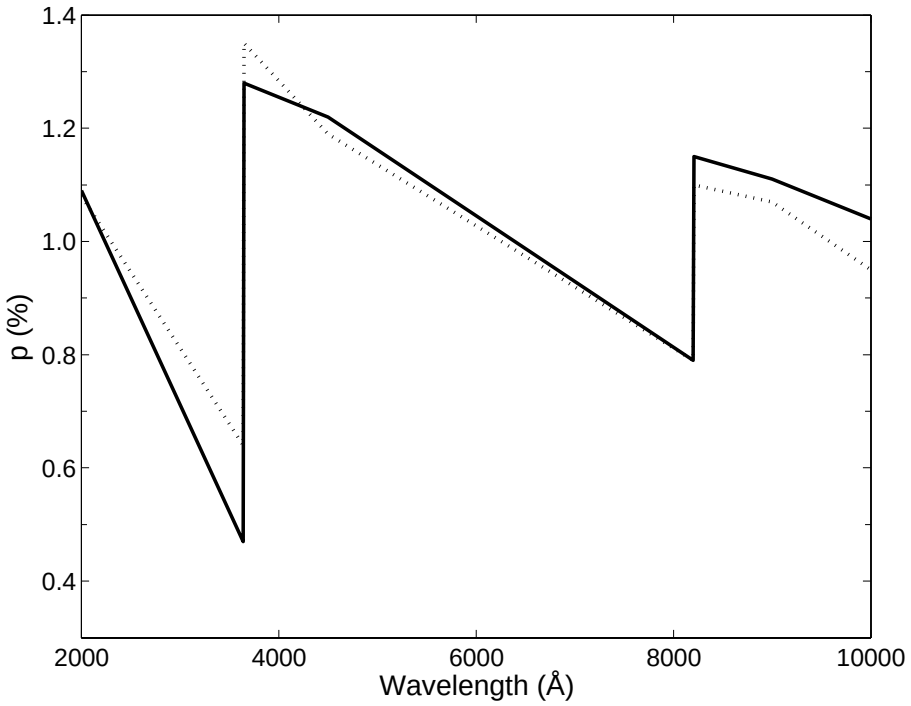

Figure 3.1: Comparison between the BEDISK and PM single-scattering polarization results. The solid line corresponds to the polarization obtained using the Poeckert and Marlborough code. The dashed line represents the polarization obtained using the corresponding BEDISK model.

Be stars. The effect of a self-consistent computation of the thermal structure of the disk, which results in a lower mass-weighted average gas temperature, is shown in Figure 3.2D. The differences in temperature in a non-isothermal disk affect the level populations and the amount of ionization in the disk: cooler temperatures in the midplane result in increased absorptive opacity and decreased ionization with fewer electrons available for scattering (Millar & Marlborough, 1998). These two factors contribute to a dramatic decrease in the net continuum polarization. We find that the inclusion of the non-isothermal disk has the most significant impact on the predicted continuum polarization levels. This result is consistent with Carciofi & Bjorkman (2008) who also found that computing a non-isothermal solution for the temperature structure of the disk yielded a significant decrease in the continuum polarization.

Finally, we investigated the effect of substituting the pure hydrogen chemical composition for one consisting of H, He, C, N, O, Mg, Si, Ca, and Fe. The inclusion of metals in the disk can have an important impact on the temperature structure of the disk

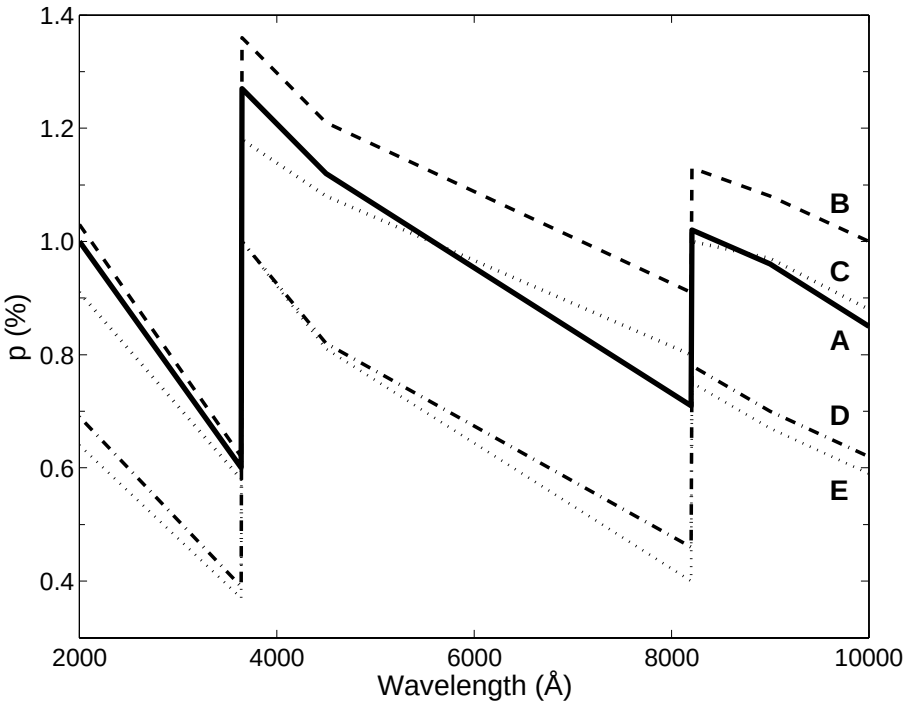

Figure 3.2: Effect of the improvements incorporated by the BEDISK code on the continuum polarization. (A) Baseline model of pure hydrogen with 5 levels included, an isothermal disk and 13 sectors used on the stellar surface. (B) Pure hydrogen with 15 levels included, an isothermal disk, and 13 sectors. (C) Pure hydrogen with 15 levels included, an isothermal disk, and 19x19 stellar sectors. (D) Pure hydrogen with 15 levels included, a non-isothermal disk, and 19x19 stellar sectors. (E) Full solar chemical composition, including 15 levels of hydrogen, a non-isothermal disk, and 19x19 stellar sectors.

(Jones et al., 2004). The presence of metals in the circumstellar environment introduces new mechanisms of heating and cooling the gaseous disk. The most important effect is the escape of collisionally excited line radiation that acts to cool the gas. The effect of implementing a realistic chemical composition in the disk on the continuum polarization is illustrated in Figure 3.2E. The resulting change in the absorptive opacity with the inclusion of additional components yields a small decrease in the polarization across most of the spectrum.

3.3.2 Comparison to Observations

As we have shown, the polarization results published by PM may not accurately reflect the true polarization measure given the inherent limitations of the computational

model: an insufficient density sampling coupled with a lack of a realistic chemical composition for a non-isothermal temperature distribution. These factors greatly affect the level populations and the ionization in the disk, and this produces a substantial impact on the predicted polarization. For the sake of completeness, we used BEDISK to find a best-fit model for the polarimetric observations used by PM. Again, we used the same stellar parameters as PM, provided in Table 3.1. A range of parameters covering ρ_0 = 1×10^{-11} to 7.5×10^{-11} g cm^{-3} and n = 2.5 to 3.5 was considered. Our best-fit model for the observational data fitted by PM, illustrated in Figure 3.3, was obtained using ρ_0 = 5×10^{-11} g cm^{-3} and n = 3.5. Our predicted polarization provides a good fit to the slope of the continuum and the Balmer jump. Overall, this fit provides a better agreement to the data than was obtained by PM, whose models predicted consistently higher levels than measured.

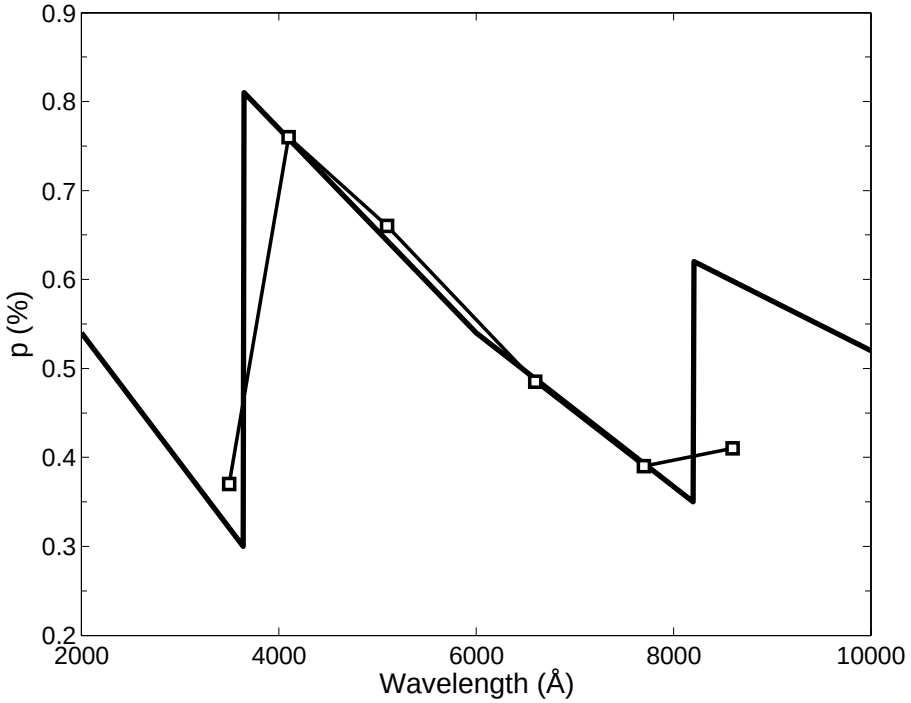

Figure 3.3: Polarimetric spectrum of the classical Be star γ Cas. The thick line represents our best fit to the 1976 November observations which are plotted with open squares. PM's original comparison included the observations plotted here along with additional observations that highlighted the variation of the polarization of γ Cas with time (Poeckert & Marlborough, 1978).

3.4 Effect of multiple-scattering

As both the Monte Carlo routine and the integration along lines of sight use the same underlying models in their computations, we can compare their output in the single-scattering limit to ensure that their predictions are consistent with each other. Restricting the Monte Carlo code to a single-scattering mode, we tested the two codes using an extensive series of BEDISK models that included variations in n and ρ_0 as well as modifications to the structure of the density distribution. Then, we compared the Stokes parameters calculated by the two procedures. The comparisons showed good agreement between the two procedures for all the models. Figure 3.4 illustrates sample comparisons for two models. Clearly, the polarization spectra produced by the two codes are quite similar for the two represented models. For the remainder of this section, we use the Monte Carlo code to produce both single-scattering and multiple-scattering results to evaluate the importance of multiple-scattering on the continuum polarization levels that arise in optically thin and optically thick gaseous disks.

We first compared single- and multiple-scattering in circumstellar disks with zero absorptive opacity. Without any absorption of pre- or post-scattered photons, the polarization spectra is wavelength-independent. For circumstellar disks that are optically thin or mostly optically thin, the single- and multiple-scattering calculations yield the same polarization level as most scattered photons only scatter once before exiting the disk. Differences between the two modes arise for models with $\rho_0 \geq 2.5 \times 10^{-11}$ g cm^{-3}, as illustrated in the left panel of Figure 3.5. Given a sufficient density of free electrons, photons are more likely to be scattered multiple times, with most of the scattering occurring in the optically thick region around the equatorial plane. This yields higher polarization values as the orientation of the scattering planes is biased towards the midplane of the disk.

The same effects occurs in circumstellar disks where the absorptive opacity of the gas is included, as shown in the right panel of Figure 3.5. With the addition of gas absorption, the continuous polarization spectra become imprinted with the wavelength-dependent signature of the absorptive opacity. Significant differences between the polarization spectra for the single- and multiple-scattering modes are apparent when the density of the material is high, with $\rho_0 \geq 1.0 \times 10^{-10}$ g cm^{-3}. In these cases, multiple-

scattering becomes important in properly determining the height of the Balmer jump and the slope of the continuum because multiple-scattering increases the polarization level more at wavelengths where the absorptive opacity is lowest. In our highest density model, for $\rho_0 = 4.0 \times 10^{-10}$ g cm^{-3}, the difference in the Balmer height between the single and multiple-scattering models was $p = 0.5\%$. In disks where the density of the material is lower, so $\rho_0 \leq 5.0 \times 10^{-11}$ g cm^{-3}, the difference between the polarization level predicted from the multiple- and single-scattering modes across all wavelengths is generally less than $p = 0.1\%$. Examining the specific contribution from multiple-scattered photons to the continuum polarization levels, as illustrated in Figure 3.6, again highlights the unimportance of multiple-scattering in circumstellar disks that are optically thin and its importance in optically thicker circumstellar disks.

These results are consistent with the findings of Wood et al. (1996b) who also found that the polarization levels from multiple-scattering exceeds single-scattering levels at wavelengths where the absorptive opacity is lowest and decreases to single-scattering levels where the absorptive opacity is highest. Because of this effect, the inclusion of multiple-scattering is necessary in correctly reproducing the primary features of the polarimetric spectrum such as the height of the jumps and the slope of continuum.

3.5 Summary

In this work, we used the non-LTE radiative transfer code of Sigut & Jones (2007), complemented by a pair of procedures for computing the Stokes parameters, to investigate the physical conditions and processes which affect the fraction of linearly polarized light emitted from classical Be stars. As polarimetric measurements provide an important perspective for observing the formation and dissipation of the circumstellar disks (Wisniewski et al., 2010; Halonen & Jones, 2013), it is critical that we develop an accurate understanding of how physical changes to the circumstellar material shape the observed polarization measurements. We investigated the importance of multiple electron scattering in circumstellar scattering regions of varying optical depths. We have shown that for gaseous disks with extended optically thick regions, multiple-scattering can significantly modify the resultant continuous polarization spectrum and is essential for computational modelling of the spectropolarimetric features. In

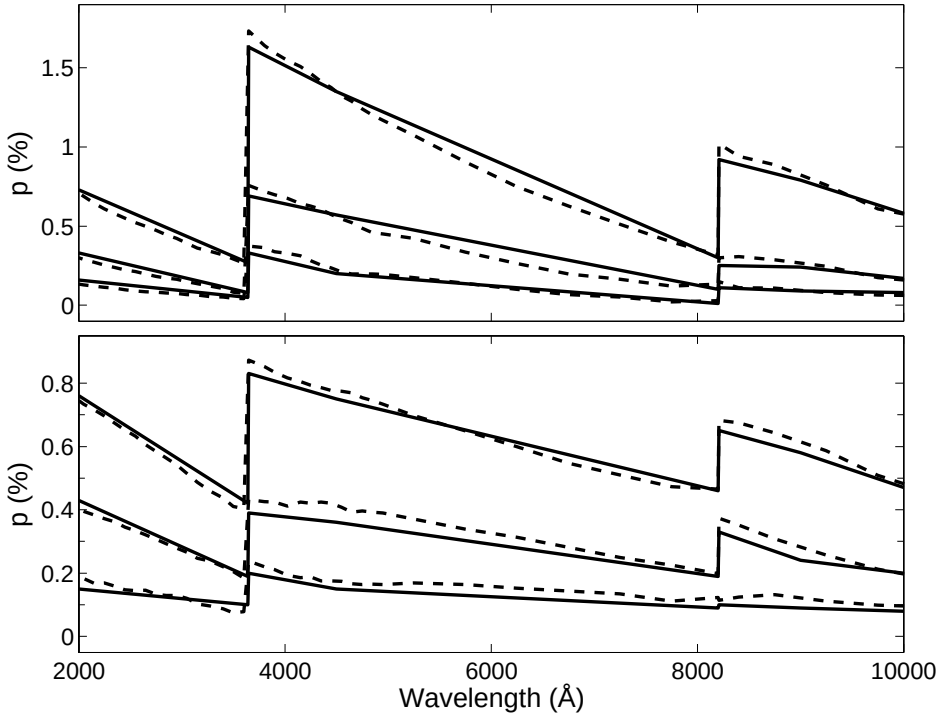

Figure 3.4: Comparison of polarization spectra computed with the integration along lines of sight calculation (solid lines) and the forced single-scattering Monte Carlo calculation (dashed lines) at inclination i = 75°, 45° and 30° (from top to bottom). The modelled star is a B2V star with disk parameters $n = 3.5$ and $\rho_0 = 2.0 \times 10^{-10}$ g cm^{-3} (top panel) and $\rho_0 = 1.5 \times 10^{-11}$ g cm^{-3} (bottom panel).

optically thin circumstellar disks, the effect of multiple-scattering is generally negligible.

We have shown that the improvements of Sigut & Jones' code from the pioneering modelling efforts of PM can provide insight into the computational parameters that affect the predicted linear continuum polarization. Once a baseline model was established between the two radiative transfer codes, we investigated the effect of each of the improvements introduced by the BEDISK code on the calculated polarization levels. We have demonstrated the need to ensure that sufficient sampling is used for both the density structure of the inner disk and the radiating surface of the central star. We showed that the polarization is quite sensitive to the calculated level populations and the degree of ionization present in the gaseous disk, thus careful consideration must be given to accurately determine these quantities. We have assessed that it is critical to compute a self-consistent thermal structure while using a realistic chemical compo-

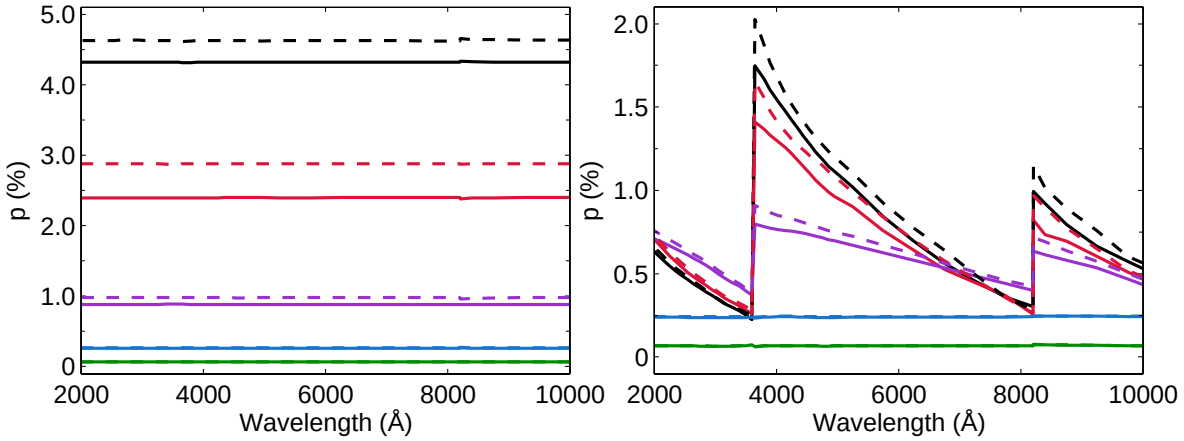

Figure 3.5: Comparison of polarization levels calculated using single-scattering (solid line) and multiple-scattering (dashed line). The models plotted have disks parameters $n = 3.5$ and, from top to bottom, $\rho_0 = 4.0 \times 10^{-10}$ g cm^{-3} (black), $\rho_0 = 1.0 \times 10^{-10}$ g cm^{-3} (red), $\rho_0 = 2.5 \times 10^{-11}$ g cm^{-3} (violet), $\rho_0 = 6.25 \times 10^{-12}$ g cm^{-3} (blue), and $\rho_0 = 1.56 \times 10^{-12}$ g cm^{-3} (green). The panel at left represent disks with zero absorptive opacity. The panel at right represents disks with both scattering and absorption processes. The spectra are plotted for an inclination i = 75°.

sition for the material in the disk when attempting to model the intrinsic continuous polarization spectrum originating from classical Be stars.

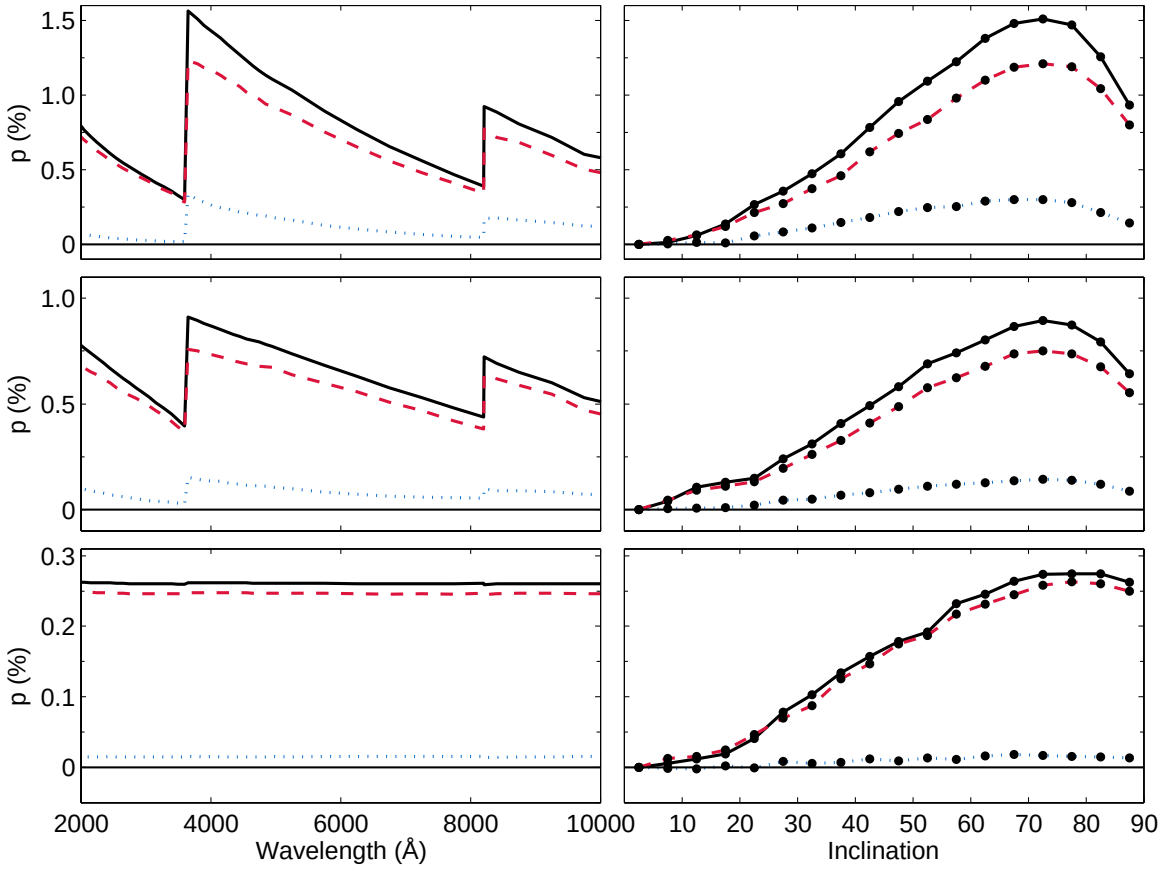

Figure 3.6: Polarization levels highlighting the contribution from multiple-scattering. The black solid line represents the entire polarization spectra with the red dashed line showing the contribution from single-scattering and the blue dotted line showing the contribution from photons that were scattered more than once. The three models illustrate the effect for disks of varying equatorial optical depths ($\lambda = 3700$Å): $\tau_{eq} \approx 50$ (top row),$\tau_{eq} \approx 10$ (middle row) and $\tau_{eq} \approx 1$ (bottom row).

Bibliography

Brown, J. C. & McLean, I. S. 1977, A&A, 57, 141

Carciofi, A. C., & Bjorkman, J.E. 2006, ApJ, 639, 1081

Carciofi, A. C., & Bjorkman, J.E. 2006, ApJ, 684, 1374

Carciofi, A. C., Miroshnichenko, A. S., Kusakin, A. V., Bjorkman, J. E., Bjorkman, K. S., Marang, F., Kuratov, K. S., García-Lario, P., Calderón, J. V. Perea, Fabregat, J., & Magalhães, A. M. 2006, ApJ, 652, 1617

Clarke, D. 2010, Stellar Polarimetry, (1st ed.; Germany: Wiley-VCH)

Clarke, D., & Bjorkman, K. S. 1998, A&A, 331, 1059

Chandrasekhar, S. 1960, Radiative Transfer (1st ed.; New York: Dover)

Coyne, G. V., & Kruszewski, A. 1969, AJ, 74, 528

Draper, Z. H., Wisniewski, J. P., Bjorkman, K. S., Haubois, X., Carciofi, A. C., Bjorkman, J. E., Meade, M. R., & Okazaki, A. 2011, ApJ, 728, 40

Halonen, R. J., & Jones, C. E. 2013, ApJ, 765, 17

Jones, C. E., Sigut, T. A. A., & Marlborough, J. M. 2004, MNRAS, 352, 841

Kurucz, R. F. 1993, Kurucz CD-ROM No. 13. Cambridge, Mass: Smithsonian Astrophysical Observatory

Lucy, L. B. 1999, A&A, 344, 282

Marlborough, J. M. 1969, ApJ, 156, 135M

Mackay, F. E., Elias, N. M., Jones, C. E., & Sigut, T. A. A. 2009, ApJ, 704, 591

McDavid, D. 1998, PASP, 758, 494

Millar, C. E., & Marlborough, J. M. 1998, ApJ, 494, 715

Millar, C. E., & Marlborough, J. M. 1999, ApJ, 526, 400

Poeckert, R., & Marlborough, J.M. 1978, ApJ, 220, 940

Porter, J. M., & Rivinius, T. 2003, PASP, 115, 1153

Quirrenbach, A., Bjorkman, K. S., Bjorkman, J. E., Hummel, C. A., Buscher, D. F., Armstrong, J. T., Mozurkewich, D., Elias, N. M. II, & Babler, B. L. 1997, ApJ, 479, 477

Sigut, T. A. A. & Jones, C. E. 2007, ApJ, 668, 481

Wisniewski, J. P., Draper, Z. H., Bjorkman, K. S., Meade, M. R., Bjorkman, J. E., & Kowalski, A.F. 2010, ApJ, 709, 1306

Wood, K., Bjorkman, J. E., Whitney, B. A., & Code, A. D. 1996, ApJ, 461, 828

Wood, K., Bjorkman, J. E., Whitney, B. A., & Code, A. D. 1996, ApJ, 461, 847

Wood, K., Bjorkman, K. S., & Bjorkman, J. E. 1997, ApJ, 477, 926

Chapter 4

On the Intrinsic Continuum Linear Polarization of Classical Be Stars during Disk Growth and Dissipation

A version of this chapter has been published in The Astrophysical Journal as Halonen, R. J., & Jones, C. E., 2013, ApJ, 765, 17. In this chapter, Halonen et al. 2013 refers to Chapter 3 of this thesis.

4.1 Introduction

In his treatise on the transfer of radiation in stellar atmospheres, Chandrasekhar (1946) predicted the polarization of continuous light in the emergent radiation from early-type stars. He theorized that the polarization from light scattered in the darkened limbs of stellar atmospheres could be detectable under favourable conditions. While the early observational polarimetry is widely recognized for the serendipitous discovery of polarization from scattering by interstellar dust, it also confirmed that some stars emit intrinsically polarized light. These observations suggested a different source for the detected polarization than that of the hypothesis that spurred the investigation; instead, the polarigenic mechanism was determined to be the scattering of radiation in the circumstellar material enveloping the stars (see, for example, Coyne & Kruszewski, 1969; Zellner & Serkowski, 1972). Since then, the observation of stel-

lar phenomena through polarimetric observation has yielded important findings for many different types of stars. For an overview of the history and application of polarimetry in stellar astronomy, we refer the interested reader to the excellent textbook by Clarke (2010).

It is now known that the intrinsic polarization from scattering is an important property for investigating the nature of celestial objects. Particularly, the polarization signature of the light from an observed target contains information regarding the geometric properties of the system. Clues to the astronomical geometry of sources of scattered light may be ascertained by examining the orientation associated with the observed polarized light. In the case of stars with circumstellar environments, polarimetric observations of stars provide a means of examining the surrounding material without having to resolve the object. Because the polarigenic mechanism responsible for the detected polarized light is intrinsic to the surrounding envelope, the signature is a separate observational feature that characterizes the scattering material. As such, stellar polarimetry provides a direct means for probing the scattering environments around particular stars.

In this paper, we examine the characteristics of the linearly polarized continuous light produced in classical Be stars. Before proceeding, it is necessary to distinguish between objects that are designated as *classical* and those that are not. The general term *Be star* describes any B-type star that exhibits spectral line emission. This description commonly includes, but is not limited to, classical Be stars, Herbig Be stars, B[e] stars and luminous blue variables. The term *classical Be star* refers to an object for which there is observational evidence that it possesses, or has possessed at some point in time, a circumstellar disk of gas orbiting the star in Keplerian fashion (Porter & Rivinus, 2003).

The prototypical classical Be star is characterized by observational features that reflect the interaction between the radiation emitted by a hot massive star and the cooler material present in its circumstellar environment. It is now accepted that this material exists predominantly in the form of a thin, equatorial, decretion disk of ionized gas with minimal radial outflow. This is confirmed by interferometric observations which resolve the disk of nearby classical Be stars (Quirrenbach et al., 1997) and spectroastrometric observations which verify that the disk rotation is Keplerian (Wheelwright

et al., 2011). In addition to a linear polarization signature, the distinct set of features observed in classical Be stars include a prominent emission-line spectrum, an excess of continuum emission and periodic line profile variations. Due to changing physical conditions in the disk, the relative intensity of these observational properties may vary on timescales that range from days to decades. These observed features may even disappear, a phenomenon that is interpreted as the complete dissipation of the surrounding gas, and reappear after a period when the disk reforms.

The physical description of the Keplerian disk adheres well to the steady-state viscous disk model (Lee et al., 1991; Okazaki, 2001) which can explain numerous features of classical Be stars (Carciofi, 2011). Despite extensive observation and study, however, the processes involved in the formation of the viscous disks remain unidentified. While several mechanisms have been proposed (see Owocki, 2006), none rigorously satisfy all of the observational requirements. Rapid rotation is presumed to be vital to the process as classical Be stars rotate more rapidly than average B-type stars. Typical rotational velocities are measured at about 70 to 80 % of the critical velocities (Porter, 1996), although this number may be systematically underestimated due to the inherent nature of these systems (Townsend et al., 2004). Mass ejection from the central star may be driven by non-radial pulsations (Rivinius et al., 2003; Cranmer, 2009) or binary companions (Harmanec et al., 2002). However, a viable process for providing sufficient angular momentum to achieve a tenable Keplerian disk remains elusive. The collaborative efforts of observers and theorists are crucial to resolving this long-standing challenge of classical Be stars.

The motivation of theoretical studies is to identify the processes involved in the evolution of stellar decretion disks and to improve our understanding of the interaction between massive stars and their circumstellar environments. In order to do so, it is important to accurately determine the physical properties of these disks through observation and modelling. With particular regards to this study, non-zero polarization levels constitute a key observable for investigating the nature of classical Be stars, particularly for probing the geometric properties of the circumstellar environment. With modern instrumentation, polarimetric measurements with high spectral and temporal resolution are achievable. It is critical that realistic and well-understood theoretical models are available to interpret these observations and to underlie their relevance.

In this paper, we present the implementation of a Monte Carlo calculation of the Stokes parameters using the self-consistent solution of the non-LTE radiative transfer code of Sigut & Jones (2007) to investigate the physical properties of the circumstellar disks of classical Be stars. This study provides a much-needed theoretical consideration of classical Be stars for an important astronomical technique and reinforces the merits of polarimetry in tracing the evolution of circumstellar disks. We aim to improve the visibility of polarimetry within the community by highlighting the utility of this observing method in investigating circumstellar environments and by emphasizing an understanding of the underlying physical properties which yield the observed polarization signature. We also use models representing the growth and dissipation of a disk surrounding classical Be stars to demonstrate how polarimetric observables are ideally suited for tracing physical changes in the circumstellar disk. These polarimetric diagnostics will be important in understanding mass decretion in classical Be stars and divining the origin of circumstellar disks.

We have organized the paper as follows: in Section 4.2, we review the basics of polarization and the Stokes parameters; in Section 4.3, we describe the computational procedures relevant to this investigation; in Section 4.4, we discuss an analysis of varying the parameters used to evaluate the polarization levels from scattering in the circumstellar gas; in Section 4.5, we examine the changes to the polarization spectrum while simulating the processes of disk growth and dissipation; and lastly, in Section 4.6, we summarize our results and discuss our ongoing research.

4.2 Polarization and the Stokes Parameters

Thomson scattering is the primary source of intrinsic continuum polarization in classical Be stars. When unpolarized light undergoes scattering by free electrons, it becomes linearly polarized perpendicular to the plane containing the incident and scattered radiation. When Thomson scattering occurs in a source that appears spherically symmetric on the plane of the sky, the distribution of polarizing planes is uniform, resulting in the complete cancellation of vibrations from orthogonal directions. In a classical Be star, the projection of the circumstellar disk is spherically symmetric when the rotational axis of the star coincides with the observing line-of-sight. In other words,

classical Be stars should exhibit no net polarization when viewed pole-on. When the rotational axis of a classical Be star is inclined with respect to the direction of an observer, the projection of the disk on the observation plane becomes non-radially symmetric and the complete cancellation of the vibrations does not occur. Thus, classical Be stars exhibit net polarization when viewed at higher inclinations, with the polarimetric position angle cast perpendicularly to the plane of the disk.

Among the earliest indications that the light emitted by some classical Be stars is partially polarized were the variable polarimetric measurements in ζ Tau by Hall & Mikesell (1950) and γ Cas by Behr (1959). Since then, observations have shown that a significant number of classical Be stars exhibit some intrinsic linear polarization of their continuous light. The degree of this polarization signature is often variable, but it has been measured to be as high as a few percent of the total emitted radiation. Analysis of the intrinsic polarization distribution for a sample of 495 objects by Yudin (2001) concluded that 95% of classical Be stars exhibit polarization on a level of $0\% < p < 1.5\%$.

Analyzing the behaviour of the polarized light from scattering in the ionized disk can yield valuable information regarding the nature of the medium. The importance of polarimetric observations in monitoring these systems is exhibited in several ways: the orientation of the polarization position angle provides information regarding the astronomical geometry of the disk; the relative intensity of the polarization reflects the number of scatterers in the disk; the wavelength-dependence of the polarization spectrum reveals the composition and density of the disk material; and the time-dependence of the position angle and the relative intensity exposes evolutionary trends in the physical structure of the disk.

Although electron scattering is a wavelength-independent process, there are two effects which contribute to the wavelength-dependence observed in spectropolarimetric measurements of classical Be stars. The first effect is the dilution of the polarized light from the emission of unpolarized light by material outside of the scattering region. The addition of unpolarized light at particular wavelengths results in a decrease in the ratio of the polarized intensity to the total intensity. This decrease in the polarization level is noticeable in strong emission lines that arise largely in extended regions of the circumstellar disk, outside of the scattering region. The second effect is the at-

tenuation of scattered light due to disk opacity. In particular, the hydrogen bound-free absorptive opacity produces a distinct sawtooth shape that is commonly observed in sufficiently strong polarization spectra of classical Be stars (see, for example, Poeckert et al., 1979; Wood, Bjorkman & Bjorkman, 1997).

Our consideration of the polarization from electron scattering in circumstellar environments builds on many previous theoretical investigations. Methods for predicting the continuum polarization from particular geometries have improved on the early analytic solutions for plane-parallel atmospheres derived by Chandrasekhar (1960) and Collins (1970) and the subsequent single-scattering approximations used by Brown & McLean (1977) and Poeckert & Marlborough (1978), for example. Using Monte Carlo simulations, Wood et al. (1996a) showed that multiple-scattering in axisymmetric circumstellar distributions of gas yields polarization levels that are higher than those predicted by single-scattering models. After including absorptive opacity in their model, Wood et al. (1996b) highlighted the importance of multiple-scattering for accurately modelling features in the continuous polarization spectrum. At present, sophisticated radiative transfer models (Carciofi et al., 2006; Sigut & Jones, 2007) have provided significant insight into the electron density and temperature structure of the circumstellar disk and have enabled greater understanding of the physical conditions that generate the observed characteristics of classical Be stars.

4.3 Computational Method

4.3.1 Radiative Transfer Code BEDISK

In a series of papers, Millar & Marlborough (1998, 1999a,b) demonstrated the importance of using a realistic non-isothermal temperature structure in considering the predicted observables of classical Be stars. For the purposes of this work, the underlying theoretical models of the classical Be stars and their gaseous envelopes are computed using the non-LTE radiative transfer code BEDISK developed by Sigut & Jones (2007). This computational code solves the coupled problems of statistical equilibrium and radiative equilibrium to provide a self-consistent calculation of the thermal structure of the circumstellar disk. Tycner et al. (2008) and Jones et al. (2009) illustrate the success-

ful use of the BEDISK code in the modelling of interferometric observations of classical Be stars.

In the computations performed by BEDISK, the energy input into the disk is assumed to originate entirely from radiation from the central star. The code employs an ATLAS9 LTE stellar atmosphere (Kurucz, 1993) to calculate the stellar photoionizing radiation field in the disk. The modelled disk is assumed to be axisymmetric about the stellar rotation axis, and symmetric about the equatorial midplane. The density distribution of gas in the envelope at coordinates (R, Z), where R is the radial distance from the stellar rotation axis and Z is the distance above the midplane, is specified by

$$\rho(R, Z) = \rho_0 (R)^{-n} e^{-(\frac{Z}{H})^2}. \tag{4.1}$$

Here, ρ_0 is the density at the base of the disk or where the disk encounters the stellar surface, n is a power-law index and H is a vertical scale height which depends on an initial value of the disk temperature. At each R, the gas is taken to be in vertical hydrostatic equilibrium perpendicular to the plane of the disk. At each computational grid location in the disk, the code computes the level populations for a specified set of atoms and ions and balances the heating (photoionization and collisional excitation) and cooling (recombination and collisional de-excitation) rates.

4.3.2 Multiple-Scattering Code

We employ a Monte Carlo procedure for calculating the fractional polarization of the emergent intensity due to electron scattering in the disk. The thermal solution computed by BEDISK provides the circumstellar gas model used by our multiple-scattering routine. Our computations follow a straightforward algorithm for simulating the propagation of photons through the extended envelope of material that surrounds a star, similar to the procedures found in Lucy (1999) and Carciofi & Bjorkman (2006).

We compared the output of our code to previous analytic and numerical results as a method for ascertaining the validity of our technique. In order to verify the accuracy of our calculations of the Stokes parameters, we simulated the reflection and transmission of light by a Rayleigh scattering atmosphere. Analytic solutions of the radiative transfer equations for the intensity and polarization of the radiation emerging from

such atmosphere were introduced by Chandrasekhar (1960). Full tables of updated solutions have been published, most recently by Natraj et al. (2009). We simulated this problem to calculate the quantities describing the emergent radiation using our Monte Carlo scattering procedure. We ran this simulation for plane-parallel slabs of varying optical depths and compared the results for different incident and viewing angles. The comparisons showed excellent agreement between our calculations and the analytic solutions.

We also tested our code against a single-scattering plus attenuation procedure for calculating the continuum linear polarization level from a classical Be star. Both procedures employ the level populations calculated by the non-LTE radiative transfer code BEDISK. The single-scattering calculations represent an update to the work of (Poeckert & Marlborough, 1978) who modelled observations of the classical Be star γ Cas with reasonable success despite the computational limitations at the time. Our comparison showed a good agreement between the two procedures. An interesting consideration that arises from this comparison is the effect of multiple-scattering in the circumstellar medium. An analysis of single-scattering versus multiple-scattering in circumstellar disks and further details of the code comparisons mentioned above are presented in Halonen et al. (2013).

4.4 Parameter Study

The primary focus of this work is to show the intrinsic continuum polarization levels that arise from circumstellar distributions of gas in particular axisymmetric geometries. As we described in the previous section, the radiative transfer code BEDISK solves the statistical and radiative equilibrium problems to compute a self-consistent solution for the thermal structure of a circumstellar disk constructed using Equation 4.1. This density equation contains two free parameters which determine the initial allocation of gas surrounding the star: the density of the disk at the stellar surface ρ_0 and the power-law index n. While the assumption of a power-law density distribution limits our consideration of smaller scale disk structure, it allows for the effect of disk density as a function of radial distance to be probed with just two free parameters and represents an ideal model for studying disk growth and dissipation, as we will discuss

in Section 4.5. In this section, we examine the effects of varying the density on the resulting polarization spectra, and we consider the importance of the inclination of the system and the temperature structure of the disk. While investigations of these effects are not novel, they provide the necessary framework for understanding the physical changes that shape the resultant polarization spectrum. Recognizing these effects is crucial for evaluating the use of polarimetry as a diagnostic for disk evolution.

4.4.1 Density Distribution

The simplest changes to the gas density distribution in the circumstellar disk are through adjustments to the density parameter ρ_0. We have computed theoretical polarization spectra for a large number of disk models. In each set of models of a disk surrounding a star of a given spectral type, we vary ρ_0 from 1.0×10^{-10} g cm^{-3} to 1.0×10^{-13} g cm^{-3} for a power-law index of $n = 3.5$. We present the results from the set of models using the stellar properties of a representative B2V star (see Table 4.1) as the central star in the system under consideration. The sets of models for other spectral types exhibit qualitatively similar results. We also examined models for varying power-law indices and found the results to support the implications made from the varying base density models.

The polarization spectra plotted in Figure 4.1 demonstrate the effects of modifying the distribution of gas in the disk on the resulting polarization. To better visualize the evolution of the spectrum as the density changes, the differences in two key polarization quantities are plotted in Figure 4.2. These two quantities are the polarization level at a particular wavelength, in this case the V-band, and the change across the jump in polarization at one of the hydrogen series limits, in this case the Balmer limit. As we will show, comparing the V-band polarization level and the change in polarization at the Balmer limit is useful in tracing the changes to the continuous polarization spectrum as we modify the distribution of gas in the disk.

In varying the density of the disk at the stellar surface, the resulting spectra are easily explained and illustrate an important optical depth effect. As ρ_0 increases, the number of electrons available for Thomson scattering increases. As expected, this translates into an increase in the polarization level. While the optical depth through the disk

is small, the polarization spectra remain flat, reflecting a wavelength-independent Thomson scattering signature unaltered by hydrogen absorption. As ρ_0 increases, it eventually attains a density at which hydrogen absorption of pre- or post-scattered photons imprints the wavelength-dependent opacity signature on the emergent spectrum of polarized light. For a power-law index of 3.5, this occurs roughly when $\rho_0 = 1.0 \times 10^{-11}$ g cm^{-3}. Above this density, the increase in scattering yields greater increases in the polarization level at wavelengths where the absorptive opacity is lowest (longward of the series limits) than at wavelengths where the absorptive opacity is highest (shortward of the series limits). This is clearly exhibited in Figure 4.1 by the appearance of jumps in the polarization spectrum at the Balmer and Paschen limits, and the steep rise of the Balmer jump as shown in Figure 4.2.

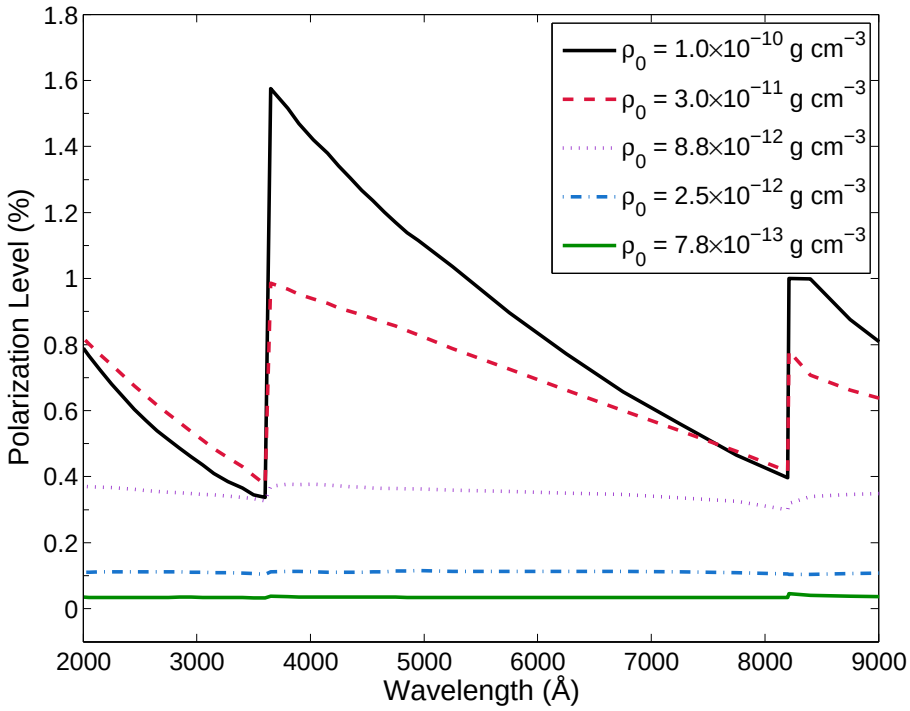

Figure 4.1: Polarization spectra for models with circumstellar disks with varying ρ_0 and with $n = 3.5$. The modelled star is a B2V star viewed at an inclination of $i = 75°$.

4.4.2 Inclination

The inclination of the classical Be star system is critical for the observed polarization. As previously discussed, as the inclination of the system tends to zero, or when the

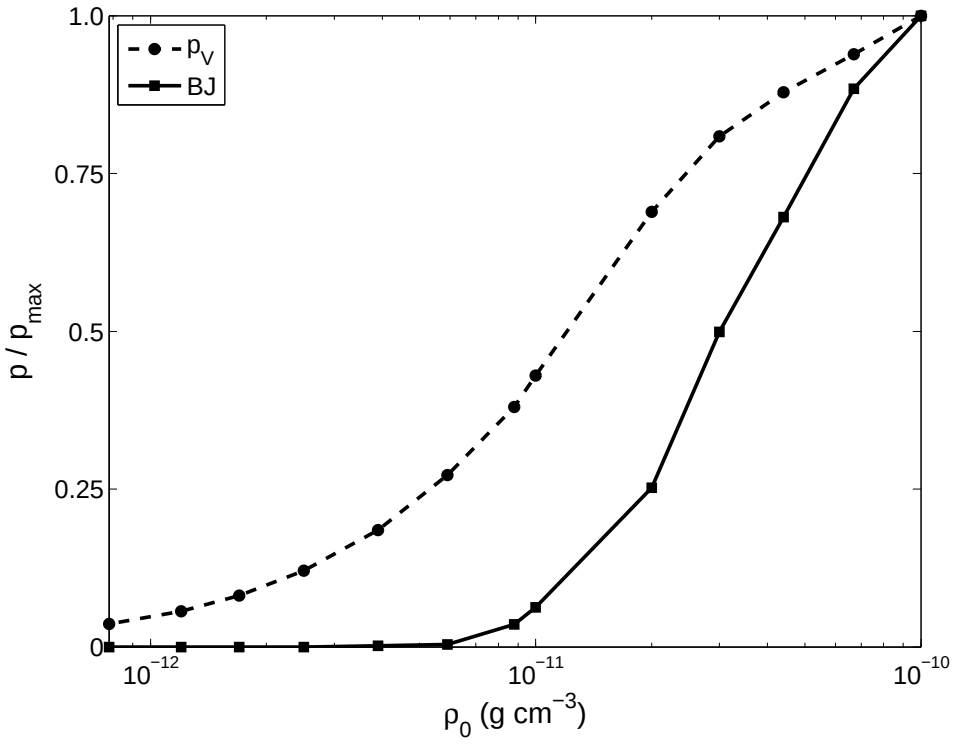

Figure 4.2: Comparison of the growth of polarimetric features (polarization level in V-band p_V and height of Balmer jump BJ) for models with circumstellar disks with varying ρ_0 and with $n = 3.5$. The modelled star is a B2V star viewed at an inclination of i = 75°.

system is viewed pole-on, the fraction of polarized light drops to zero due to the uniform distribution of polarizing planes. One might expect that the polarization would attain its maximum value when the system is viewed edge-on such that the viewing angle coincides with the scattering plane of the disk. At this inclination, we can certainly expect the smallest amount of cancellation in a geometrically thin disk. At high inclinations, however, the scattered light must travel through more gas before it exits the system. A fraction of this polarized light will be absorbed and the overall polarization level will decrease as a result. As Figure 4.3 demonstrates, the maximum polarization level does not occur at i = 90°, but instead occurs between i = 70° and i = 80°.

Table 4.1: Stellar parameters for Main Sequence B0, B2, B5 and B8 stars

Spectral Type	Radius ($R_\odot$)	Mass ($M_\odot$)	Luminosity ($L_\odot$)	$T_{\rm eff}$ (K)	$\log(g)$ ($\mathrm{cm\,s^{-2}}$)
B0V	7.4	18	4.0×10^4	3.0×10^4	3.9
B2V	5.3	9.1	4.8×10^3	2.1×10^4	3.9
B5V	3.9	5.9	7.3×10^2	1.5×10^4	4.0
B8V	3.0	3.8	1.4×10^2	1.1×10^4	4.1

4.4.3 Disk Temperature

Recent theoretical studies of classical Be stars using realistic radiative transfers models have emphasized the importance of correctly determining the thermal structure of the disk when modelling observables. Clearly, the disk models produced by Carciofi & Bjorkman (2006) and Sigut & Jones (2007) exhibit temperature maximums and minimums that deviate significantly from an isothermal disk. In order to examine the importance of the temperature structure on the polarization spectrum, we computed the polarization spectra for several models using BEDISK's self-consistent thermal structure of the circumstellar disk and compared the output to that from models using an isothermal disk. The isothermal temperatures used were 0.6 $T_{\rm eff}$. A sample of the results of the comparison are illustrated in Figure 4.4. The polarization spectra computed using the isothermal models deviate appreciably from the polarization spectra produced using the non-isothermal disk for higher-density models. For optically thinner models, the difference between the polarization levels is much less pronounced. This agrees with the results of a study by Carciofi & Bjorkman (2008). The computation of the disk temperature solution produces a region of cooler gas in near the equatorial plane of the disk. This affects the level populations in the non-isothermal parts of the disk and an increase in the absorption of scattered photons. Hence, the non-isothermal disks yield smaller polarization levels than the isothermal disks.

4.5 Disk Growth and Dissipation

To illustrate the changes in the polarization during key periods in the evolution of the circumstellar disk, we consider models that approximate the disk growth and dissipa-

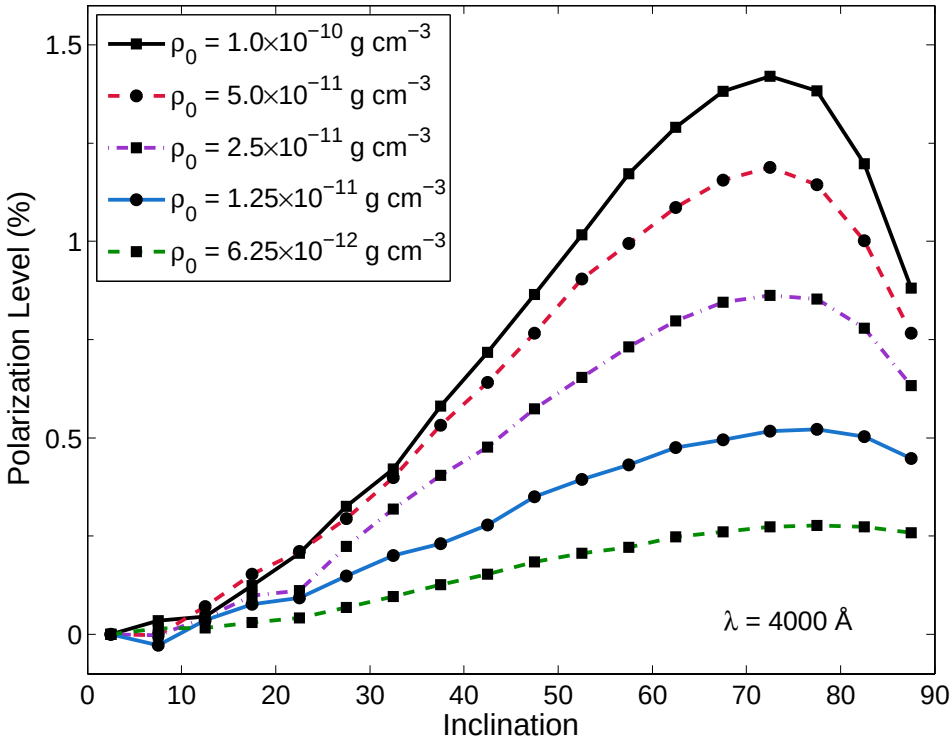

Figure 4.3: Polarization level versus inclination for a B2V star with circumstellar disks with varying ρ_0 and $n = 3.5$. For all the values of ρ_0 plotted, the polarization level peaks between $i = 70°$ and $i = 80°$.

tion phases. In order to simulate the formation of the disk, we use a series of models with the same values of n and ρ_0 and increasing disk size. Similarly, the dissipation of the disk is simulated using a series of models with an inner hole of increasing width. While these series of models represent idealized approximations of actual disk growth and dissipation, the results trace important changes to the observables and demonstrate the possibilities for time-dependent polarimetric measurements as a diagnostic of changing physical conditions in the circumstellar gas.

4.5.1 Growth

We produced a series of models that approximates disk growth by incrementally increasing the outer radius of the circumstellar disk from the stellar surface up to 100 R_*. With each adjustment to the size of the disk, we recompute the thermal structure of the disk using the radiative transfer code. Figure 4.5 shows the gradual change in the polarization spectra as the size of the disk increases. Figure 4.6 plots the evolution of

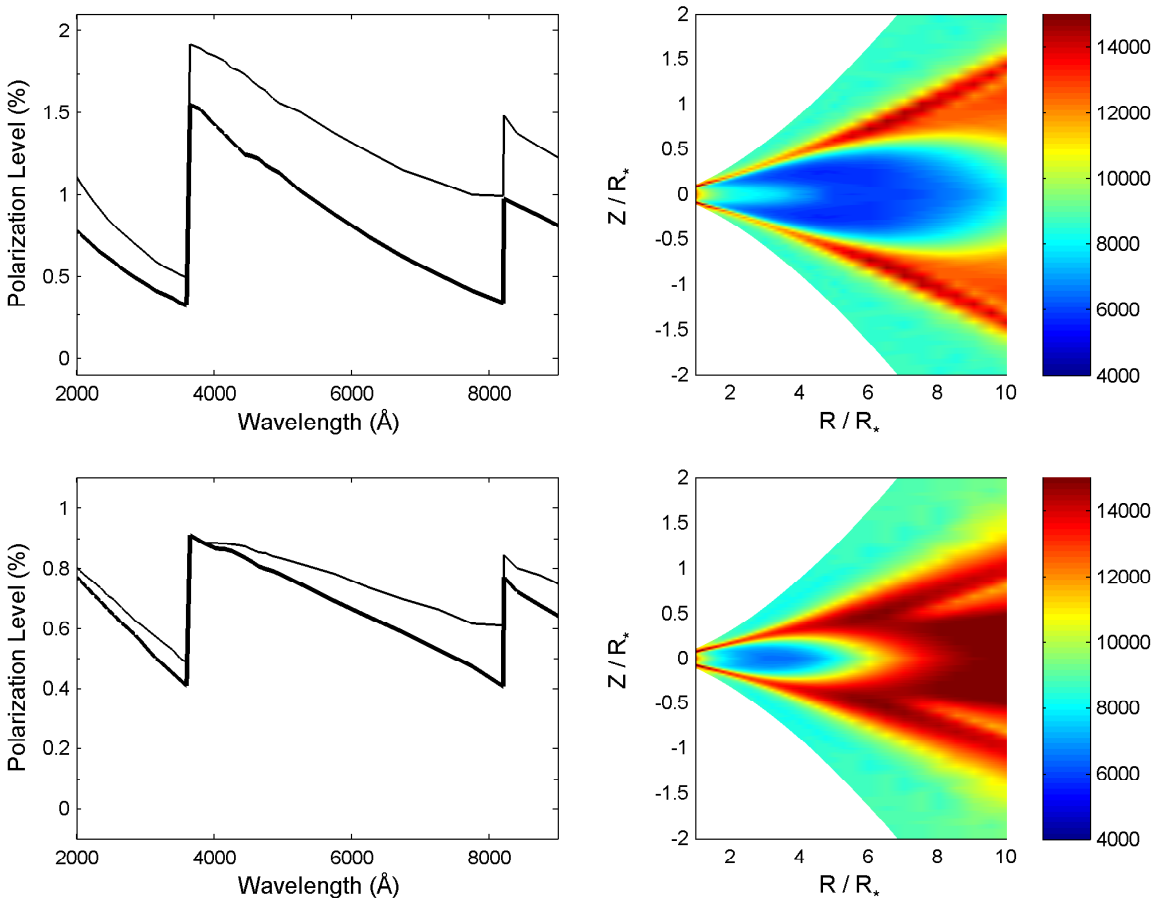

Figure 4.4: Left: Polarization spectra for models using a non-isothermal disk (thick lines) and an isothermal disk (thin lines) viewed at $i = 75°$. Right: Temperature structure of the non-isothermal disks computed by BEDISK. The models plotted are for B2V stars surrounded by circumstellar disks with $n = 3.5$ and with $\rho_0 = 1.0 \times 10^{-10}$ g cm^{-3} (top) and 2.5×10^{-11} g cm^{-3} (bottom).

the two previously-introduced polarization quantities, the V-band polarization level and the change in polarization at the Balmer jump.

The formation of the disk is reflected in the polarization spectra with the steep rise of the Balmer jump and the comparatively more gradual rise of the polarization level. As mass is ejected from the stellar surface, the density and optical depth in the innermost region of the disk rapidly increases to the point at which the wavelength-dependent imprint of the absorptive opacity appears in the polarization spectrum. As the disk increases in mass and extent, the number of scatterers increases and the solid angle subtended by the disk grows; hence, the polarization level rises, albeit more slowly than the Balmer jump. The differences in the changes of these two quantities are reflective of a system in which equatorial mass loss from the central star builds a geometrically thin, gaseous disk.

Carciofi (2011, 2012) has emphasized the importance of careful consideration of the location of the disk where observables originate when analyzing observations. Knowledge of the formation region for different observables is essential in developing diagnostics that trace the evolution of physical changes in the disk. Using the disk growth models as a basis for determining the disk formation regions, we corroborate Carciofi's assertion that 95% of the maximum V-band polarization level is reached when the disk size reaches 10 stellar radii. We note that the Balmer jump reaches this level at much smaller disk radii. It attains 95% of its maximum value when the disk size reaches 6 stellar radii. This difference in the formation regions between the two polarimetric quantities highlights their usefulness as tracers for disk growth and loss.

4.5.2 Dissipation

It is suggested that the dissipation of the circumstellar disks of classical Be stars may begin from the inner disk and proceed outward, leaving an evacuated region close to the star. Wisniewski et al. (2010) presented spectropolarimetric and Hα spectroscopic observations of two Be stars, π Aqr and 60 Cyg, with extended temporal coverage that witnessed both disk-loss and disk-renewal phases. During the disk-loss event of 60 Cyg, they noted a lag of the maximum in the Hα equivalent width from the maximum V-band polarization. Similarly, during the disk-loss event of π Aqr, they noted a lag

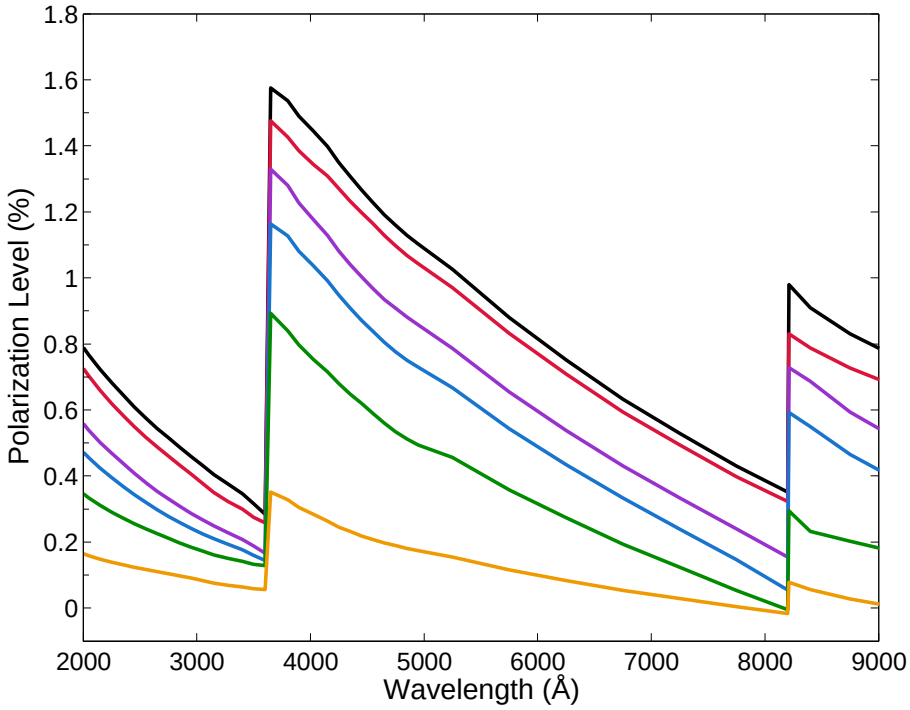

Figure 4.5: Polarization spectra for models with circumstellar disks of increasing outer radius. The models correspond to a disk with $n = 3.5$ and with $\rho_0 = 1.0 \times 10^{-10}$ g cm^{-3} and outer radius, from bottom to top: 2.0 R_* (yellow), 3.0 R_* (green), 4.0 R_* (blue), 5.0 R_* (violet), 10.0 R_* (red) and 100.0 R_* (black). The modelled star is a B2V star viewed at an inclination of $i = 75°$.

in the onset of the minimum in the Hα equivalent width strength from the minimum V-band polarization. The authors propose that these observations indicate that the evacuation of the disk proceeded in an "inside-out" manner.

In order to examine the effect of this process on the polarization level, we produced a series of models with an evacuated inner region. We begin with a disk that extends from the stellar surface up to 100 R_*. We introduce an evacuated inner region from the stellar surface up to 1.4 R_* and we incrementally increase the radius of the inner hole with each successive model. With each adjustment to the size of the inner hole, we recompute the thermal structure of the disk using the radiative transfer code. Figure 4.7 shows the gradual change in the polarization spectra as the radius of the hole increases. Figure 4.8 plots the evolution of the V-band polarization level and the change in polarization at the Balmer jump.

As one would expect, the characteristics that we noted in the growth model are inverted in this series of models. Once mass decretion from the central star terminates,

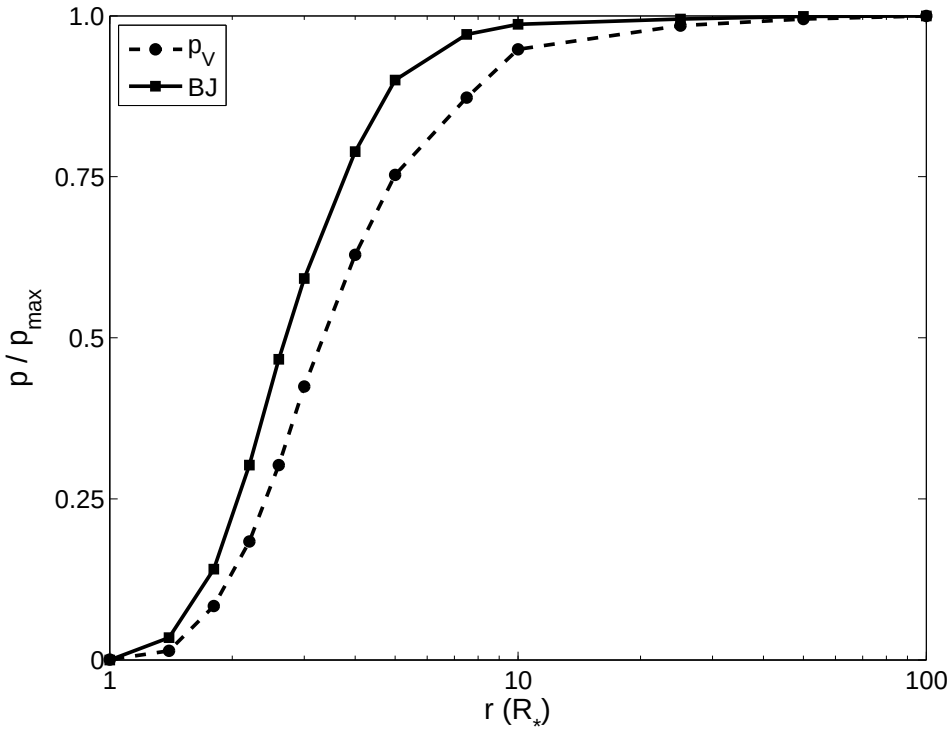

Figure 4.6: Comparison of the growth of polarimetric features for models with circumstellar disks of increasing outer radius. The models correspond to a disk with $n = 3.5$ and with $\rho_0 = 1.0 \times 10^{-10}$ g cm^{-3} and outer radius ranging from 1.0 R_* to 100.0 R_*. The modelled star is a B2V star viewed at an inclination of $i = 75°$. The differences between the two quantities in the models reflect that gas ejected from the central star is forming an equatorial disk.

the material in the disk is removed through reaccretion or outward flow. As the dense gas in the innermost region of the disk disappears and the optical depth through the disk diminishes, the height of the Balmer jump declines quickly. Once the disk is cleared up to five stellar radii, the remaining gas is entirely optically thin to hydrogen bound-free absorption and the wavelength-dependent signature of the polarization spectrum vanishes. The V-band polarization gradually declines as the mass of the disk and the number density of electrons decreases. Again, the differences in the changes of these two quantities in this series of models are reflective of the physical change to the circumstellar gas: it is being cleared from the inside-out.

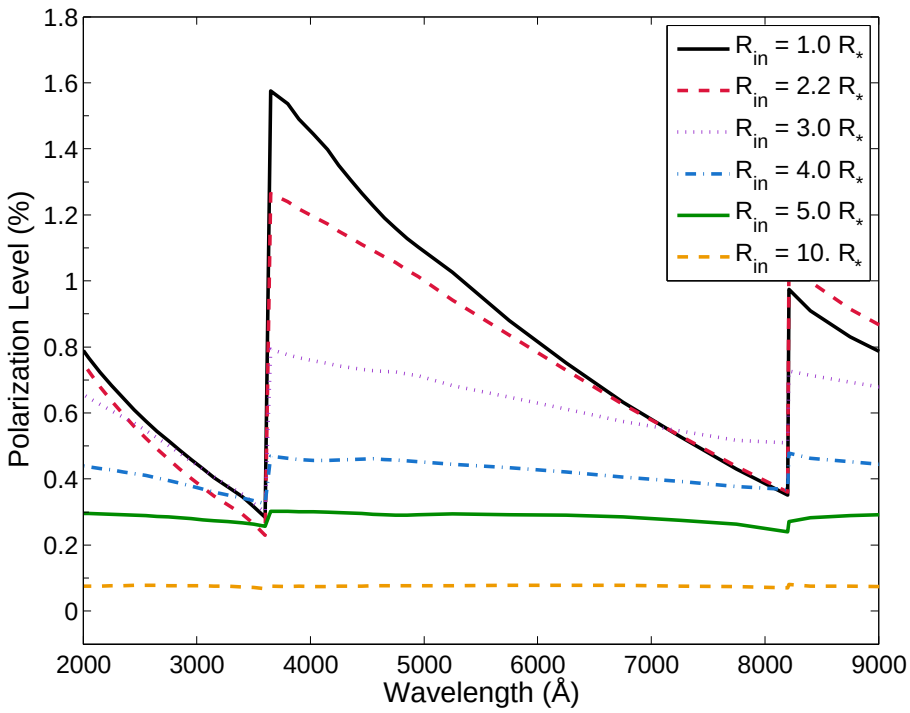

Figure 4.7: Polarization spectra for models with circumstellar disks of increasing inner hole radius. The models correspond to a disk with $n = 3.5$ and with $\rho_0 = 1.0 \times 10^{-10}$ g cm^{-3}. The modelled star is a B2V star viewed at an inclination of $i = 75°$.

4.5.3 BJV Loop

With the results from our disk growth and disk dissipation approximations, we can illustrate the complete cycle of the evolution of the disk using the Balmer jump and the V-band polarization level in what is referred to as a BJV diagram (Draper et al., 2011). In Figure 4.9, we plot the BJV diagram for the system modelled in the previous two sections. The progression of the system, as the disk grows from the stellar surface out to 100.0 R_* and then dissipates outward from the stellar surface until the disk has completely disappeared, traces a clockwise loop in the BJV diagram. Qualitatively similar loops have been observed in colour magnitude diagrams of Be stars (de Wit et al., 2006). These loops are an illustration of the effects of changes in the distribution of gas in the circumstellar disk for observables that arise from different parts of the disk. In Figure 4.10, we illustrate theoretical loops in colour magnitude diagrams and BJV diagrams for four disk models.

Having presented the polarimetric characteristics of models that approximate a Be

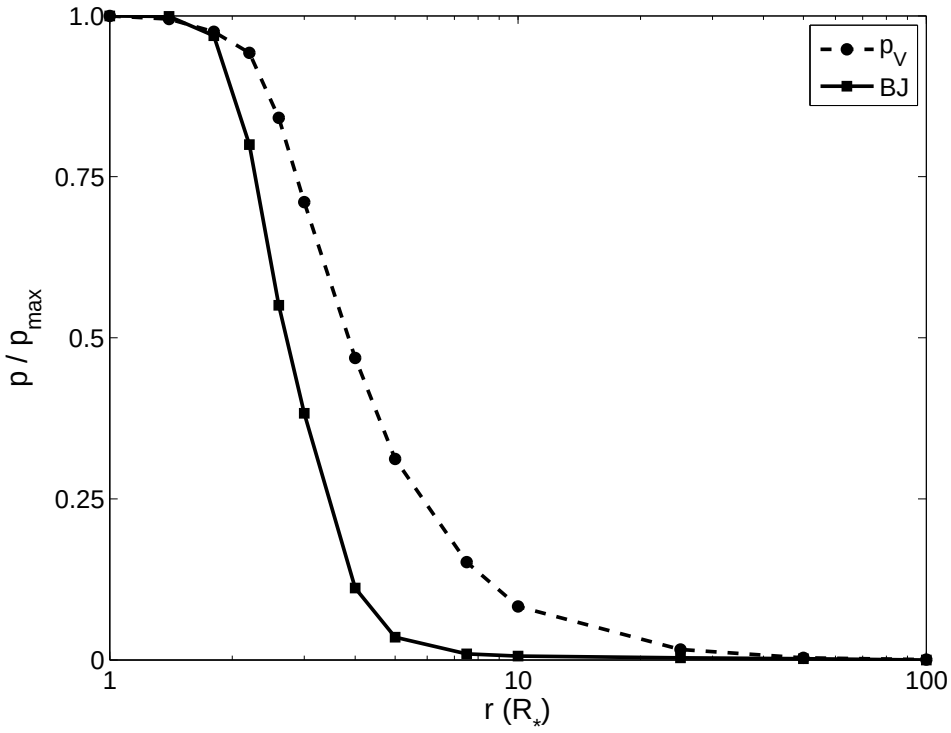

Figure 4.8: Comparison of the change in the polarimetric features for models with circumstellar disks of increasing inner hole radius. The models correspond to a disk with $n = 3.5$ and with $\rho_0 = 1.0 \times 10^{-10}$ g cm^{-3} and inner hole radius ranging from 1.0 R_* to 100.0 R_*. The modelled star is a B2V star viewed at an inclination of $i = 75°$. The differences between the two quantities in the models reflect that the circumstellar gas is clearing from the inside-out.

disk during formation and dissipation, we now examine the physical trends exhibited in BJV diagrams. We have already stated that the electron scattering polarization level, and consequently the level at wavelengths where the absorptive opacity is minimal, is determined mainly by the number of scatterers in the disk. The difference in the V-band polarization level between disks with identical density distributions but surrounding stars with different spectral types can be explained by the factor primarily determining the number of scatterers: the disk temperature. The disks around earlier spectral type stars are hotter and fully ionized. The disks around later spectral types are cooler and less ionized. As such, the disks surrounding earlier spectral type stars are more amenable to electron scattering and produce higher unattenuated polarization levels.

We now consider the polarization levels at wavelengths where the absorptive opac-

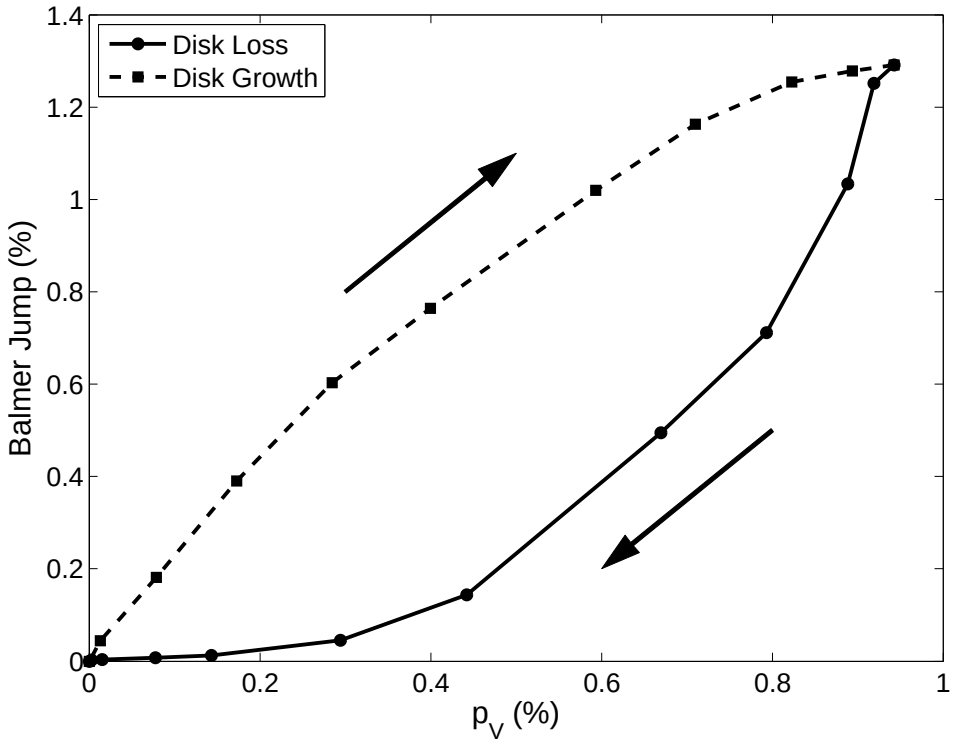

Figure 4.9: BJV loop using the models presented in Sections 4.5.1 and 4.5.2. The modelled star is a B2V star viewed at an inclination of $i = 75^\circ$ and surrounded by a disk with $n = 3.5$ and with $\rho_0 = 1.0 \times 10^{-10}$ g cm^{-3}. The disk dissipation models correspond to an inner hole of increasing radius ranging from 1.0 R_* to 100.0 R_*. The disk growth models correspond to an increasing outer radius ranging from 1.0 R_* to 100.0 R_*. The evolution of the system, from the moment that mass decretion from the central star begins until the moment where the disk is completely dissipated, traces a clockwise loop in the BJV diagram.

ity is greatest. To analyze the depolarizing effect of absorption by neutral hydrogen, we consider a series of hydrogen-only models of varying ρ_0. This allows us to examine the effect of changing the amount of disk material without the geometrical effects inherent to the growth and dissipation models. Figure 4.11 illustrates that the BJV curves produced using these models mirror those of the disk dissipation models. That is, for decreasing disk mass, we observe a clockwise descent from maximum to minimum BJV signature, with the curve more pronounced for the disk surrounding the earlier spectral type star.

The top panels in Figure 4.12 show the polarization level shortward ($\lambda \approx 3600$ Å) and longward ($\lambda \approx 3700$ Å) of the Balmer jump for disks surrounding B0V (top-right) and B8V (top-left) stars. As the disk mass increases, the polarization spectrum be-

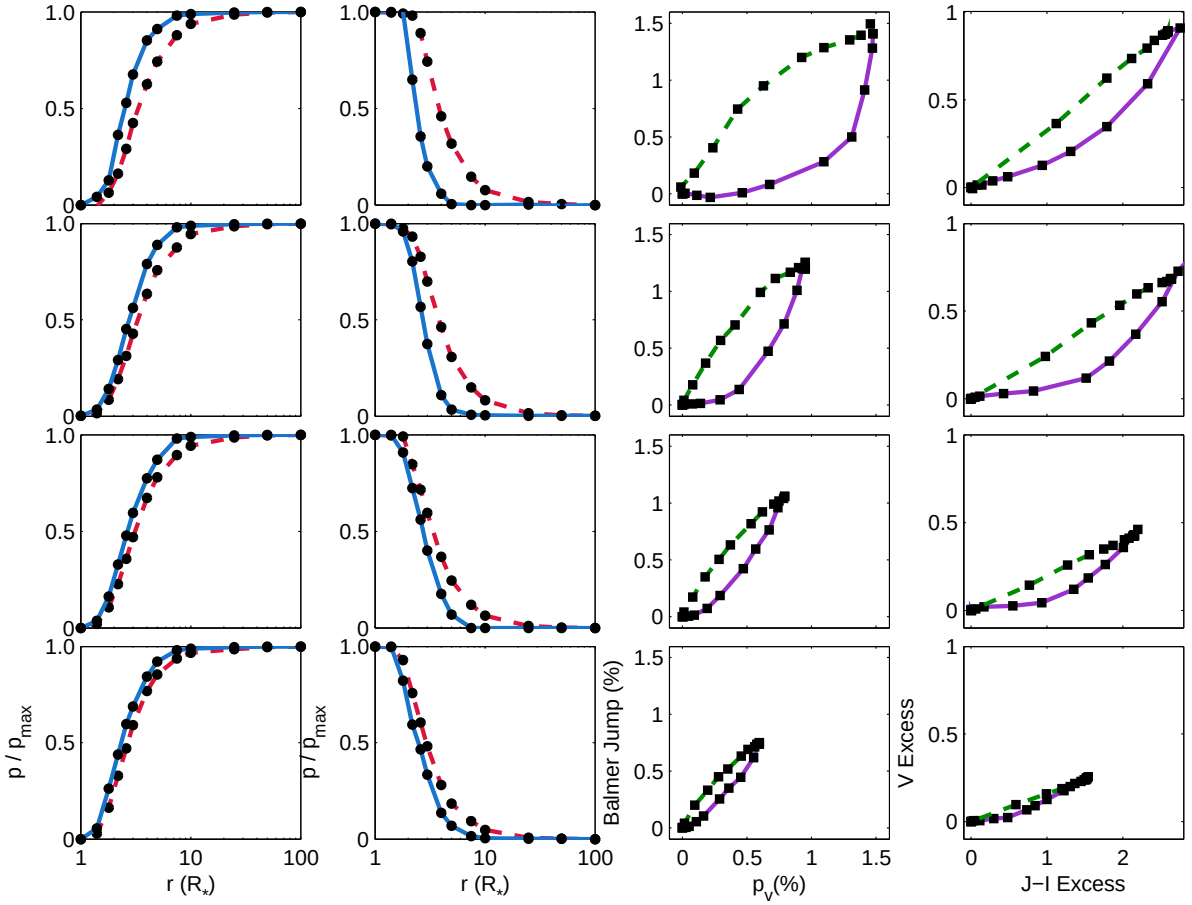

Figure 4.10: Column 1: Balmer jump (blue solid line) and V-band polarization level (red dashed line) during disk growth. Column 2: Balmer jump (blue solid line) and V-band polarization level (red dashed line) during disk dissipation. Column 3: BJV diagram at $i = 75°$ showing disk growth (green dashed line) and dissipation (violet solid line). Column 4: colour magnitude diagram at $i = 15°$ showing disk growth (green dashed line) and dissipation (violet solid line). From top to bottom: B0V, B2V, B5V and B8V stars. The models correspond to disks with $n = 3.5$ and with $\rho_0 = 1.0 \times 10^{-10}$ g cm^{-3}.

comes wavelength-dependent and the levels diverge. This occurs at a lower density for the B8 model, as the volume of the disk where scattering at 3600 Å occurs becomes dominated by absorption at lower densities in the cooler disk than in the hotter disk, as shown in the bottom-left panel of Figure 4.12. For both stars, the scattering and absorbing regions at 3700 Å remain comparable, resulting in changes to the polarization levels that are consistent with the corresponding increase in the number of scatterers. Hence, the jumps in the polarization spectrum are mainly caused by the scattered photons of the disk becoming obscured as they propagate through a larger volume of the disk where the absorptive opacity from neutral hydrogen dominates.

The general implications of these results with respect to understanding the physical insight in BJV loops are as follows. First, where the slope of the BJV curve is steepest, the absorptive opacity of the disk is changing without much change to the overall amount of polarization from electron scattering. In other words, material in the densest regions of the disk is undergoing significant changes. In terms of what is happening in the disk, this may represent an appreciable mass injection or loss in the inner disk, depending on the direction of the BJV curve. Second, where the slope of the BJV curve is flattest, the unattenuated polarization level is increasing or decreasing without much change in the disk opacity. Hence, the mass of the scattering region is changing, whether from the spread of material from the inner disk to the outer disk (top part of the disk growth curve) or the dissipation of the outer disk once the interior has vanished (lower part of the disk dissipation curve). From this interpretation of the BJV loop, it becomes clearer how this tool may be useful in understanding decretion trends in classical Be stars.

4.6 Summary

The first objective of this project was to develop a code capable of producing synthetic spectra in all four Stokes parameters to supplement a non-LTE radiative transfer computation of the thermal structure of a gaseous circumstellar disk. We report that the computational method that we have developed has been successfully tested and we are using it to analyze and model observations of classical Be stars. In achieving this goal, we have addressed one of the immediate needs identified at the recent workshop

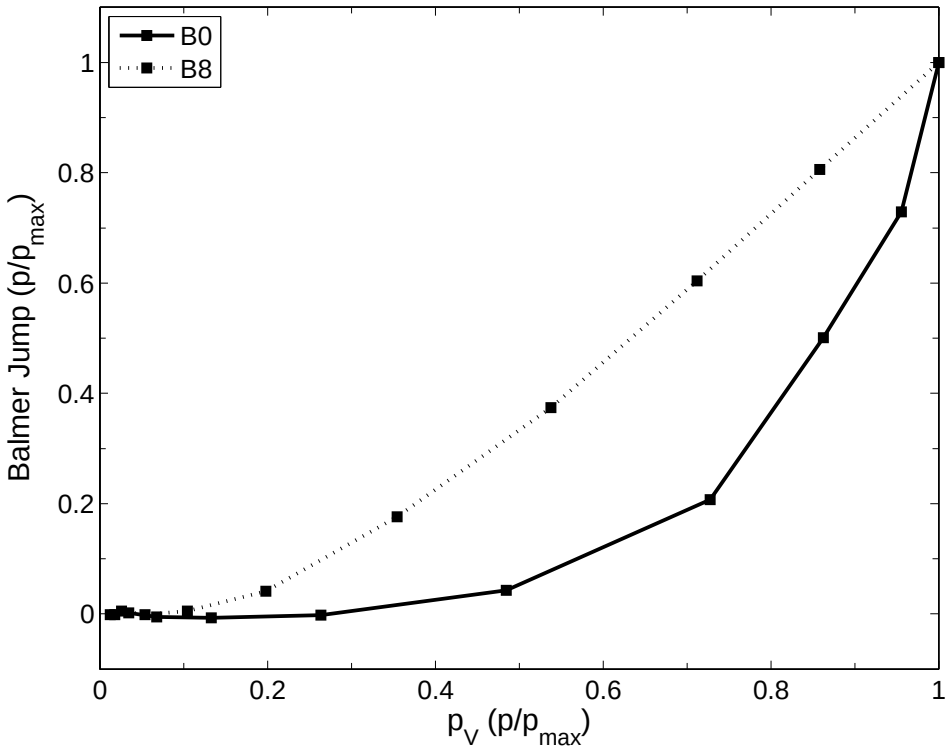

Figure 4.11: BJV curves for disks of increasing mass. The modelled stars are viewed at an inclination of $i = 75°$ and surrounded by a disk with $n = 3.5$ and with ρ_0 increasing from 3.81×10^{-13} g cm^{-3} to 2.0×10^{-10} g cm^{-3}.

on stellar polarimetry held at the University of Wisconsin-Madison (see Hoffman et al., 2012), namely to have realistic modelling codes readily available for polarimetric analysis of observations. With time-dependent analysis of the formation and dissipation of their circumstellar disks possible, we encourage the community to engage in polarimetric monitoring of classical Be stars, especially of those objects with known variability.

We have discussed the geometric and physical properties of circumstellar disks that need to be considered when interpreting polarimetric observations of classical Be stars. In particular, we emphasized the use of two quantities, the polarization level in the V-band and the polarization change across the Balmer series limit, as diagnostics of the physical structure of the disk. While the polarization level is a gauge of the number density of scattering electrons in the disk, the Balmer jump indicates the regions where bound-free opacity is greatest. We have shown that these two polarimetric quantities originate from different parts of the disk: the Balmer jump arises from the innermost

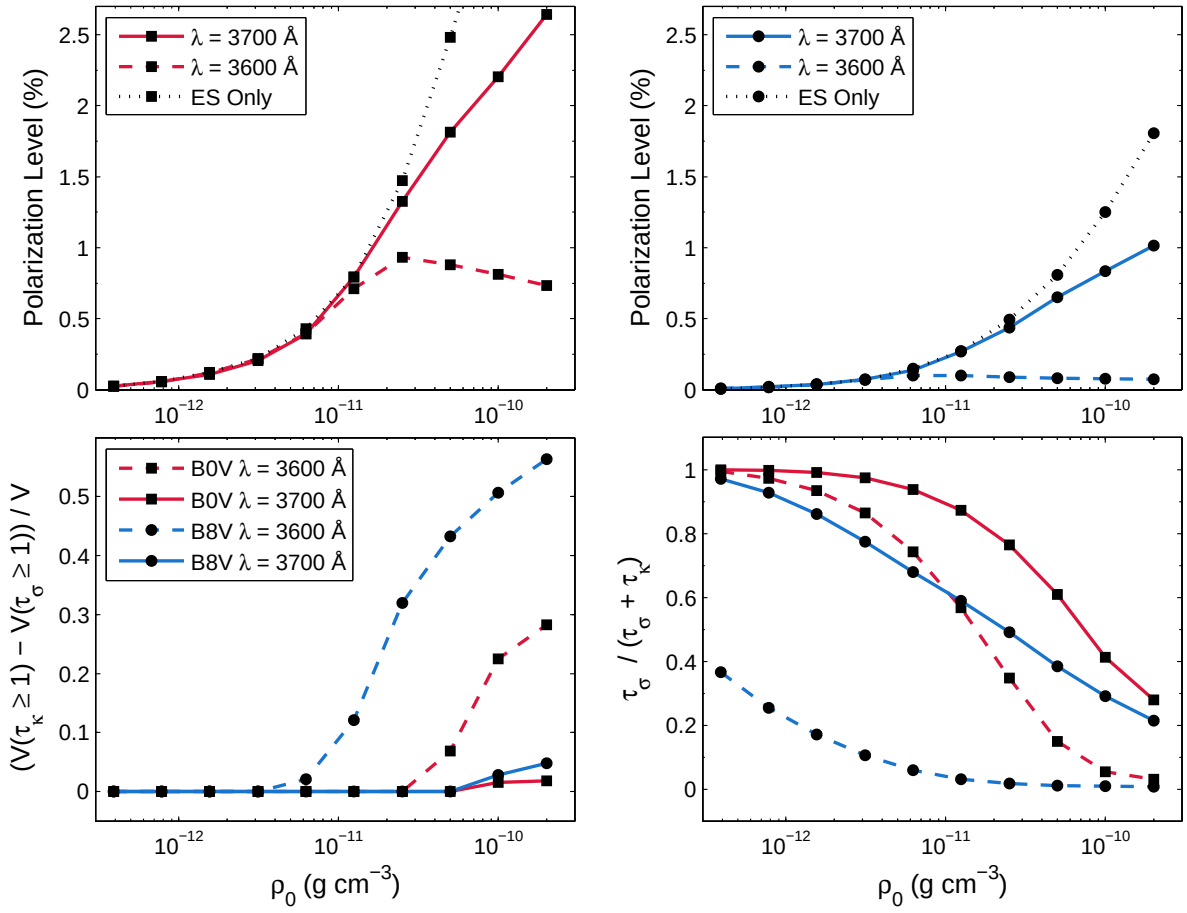

Figure 4.12: Top left: Polarization levels for a B0V star. Top right: Polarization levels for a B8V star. Bottom left: Size of the effective absorbing volume minus the effective scattering volume. Bottom right: Equatorial electron scattering optical depth with respect to the total equatorial optical depth. The modelled stars are viewed at an inclination of $i = 75°$ and surrounded by a disk with $n = 3.5$ and with ρ_0 increasing from 3.81×10^{-13} g cm^{-3} to 2.0×10^{-10} g cm^{-3}.

regions of the disk while the source of the polarization level extends further out in the disk. In particular, we have shown here that the Balmer jump in the polarization spectrum arises from the region of the disk located up to 6 stellar radii from the star. Showing that the excess continuum flux in the K-band arises from a region of this exact radial size, Haubois et al. (2012) stated the importance of this region as being where the highest density variations for periodic decretion are observed. Given our understanding of the dependence of the polarimetric Balmer jump on density, it is clear that this polarimetric feature will be useful for monitoring mass decretion in classical Be stars.

We presented radiative equilibrium consistent models that approximate the formation and dissipation of a thin, decretion disk of gas surrounding a hot, massive star. While the evolution of the disk is idealized, these models represent an excellent test bed for predicting and understanding the behaviour of the continuous polarization spectrum during the evolution of the circumstellar disk. We corroborated the theoretical BJV loop presented in Draper et al. (2011). In Figure 4.10, we presented different models which emphasize the difference in the formation region of different observables, a characteristic manifested by loops in BJV diagrams. With this focused study on the polarimetric properties of classical Be stars, we have established a framework for characterizing the BJV loops through knowledge of the physical properties of the disk. These results are particularly important as we expect these loops to reflect time dependent mass decretion in classical Be stars. Thus, observing and modelling these features should play a pivotal role in identifying the mass-loss processes which drive the development of circumstellar disks.

All of the models in this work assume fixed-rate mass decretion from the surface of the central star and axisymmetry in the distribution of the gas in the disk. As such, these idealized models trace out clear, clockwise loops in the colour magnitude and BJV diagrams. Observed colour magnitude and BJV diagrams of classical Be stars show more complicated behaviour then presented here. Modelling and interpreting these observations will require the inclusion of varying mass decretion rates and the consideration of non-axisymmetric distributions of disk material. Furthermore, it has been suggested that in circumstellar environments where material is actively accreting onto the central star, we might observe counter-clockwise loops in colour-magnitude

and BJV diagrams. Such loops in classical Be stars may indicate that a significant portion of the disk material reaccretes onto the star during the disk dissipation period. However, Draper et al. (2011) speculate that counter-clockwise loops in BJV diagrams could be caused by non-constant mass decretion rates or more complicated mass ejection processes. Whatever the case, more sophisticated models of disk growth and dissipation are required for tackling these problems. We are currently working on models which included variable mass-loss rates and non-axisymmetric disk density distributions.

It should be clear that polarimetric observations can aid in identifying the physical properties of circumstellar disks and can be useful in constraining the theoretical models that are crucial to correctly interpreting the observations. We are currently continuing our comprehensive investigation of the polarimetric properties of classical Be stars. While this paper focused on a theoretical consideration of the continuous polarization levels in models of circumstellar disks, our current endeavours also include comparisons with polarimetric observations of classical Be stars. Furthermore, we are currently working to produce synthetic linear spectropolarimetric profiles. This addition to the Monte Carlo scattering code will allow us to further study the geometric structure of the disk on spatial scales that cannot be directly imaged.

Bibliography

Behr, A. 1959, Z. Astrophys., 47, 54

Brown, J. C. & McLean, I. S. 1977, A&A, 57, 141

Carciofi, A. C., & Bjorkman, J. E. 2006, ApJ, 639, 1081

Carciofi, A. C., Miroshnichenko, A. S., Kusakin, A. V., Bjorkman, J. E., Bjorkman, K. S., Marang, F., Kuratov, K. S., Garca-Lario, P., Caldern, J. V., Fabregat, J., Magalhes, A. M. 2006, ApJ, 652, 1617

Carciofi, A. C., & Bjorkman, J. E. 2006, ApJ, 684, 1374

Carciofi, A. C. 2011, in IAU Symp. 272, Active OB Stars: Structure, Evolution, Mass Loss, and Critical Limits, ed. C. Neiner et al. (Cambridge: Cambridge Univ. Press), 325

Carciofi, A. C. 2012, in AIP Conference Proceedings 1429, Stellar Polarimetry: From Birth to Death, eds. J.L. Hoffman, J. Bjorkman & B. Whitney (New York: AIP), 121

Chandrasekhar, S. 1946, ApJ, 103, 351

Chandrasekhar, S. 1960, Radiative Transfer (1st ed.; New York: Dover)

Clarke, D. 2010, Stellar Polarimetry, (1st ed.; Germany: Wiley-VCH)

Collins, G. W. 1970, ApJ, 159, 583

Cox, A. N. 2000, Allen's Astrophysical Quantities, (4th ed.; New York: Springer)

Coyne, G. V., & Kruszewski, A. 1969, AJ, 74, 528

Cranmer, S. R. 2009, ApJ, 701, 396

de Wit, W. J., Lamers, H. J. G. L. M., Marquette, J. B., & Beaulieu, J. P. 2006, A&A, 456, 1027

Draper, Z. H., Wisniewski, J. P., Bjorkman, K. S., Haubois, X., Carciofi, A. C., Bjorkman, J. E., Meade, M. R., & Okazaki, A. 2011, ApJ, 728, 40

Hall, J. S., & Mikesell, A. H. 1950, Publications of the U.S. Naval Observatory Second Series, 17, 1

Halonen, R. J., Mackay, F. E., & Jones, C. E. 2013, ApJS, 204, 11

Haubois, X., Carciofi, A. C., Rivinius, T., Okazaki, A. T., & Bjorkman, J. E. 2012, ApJ, 756, 156

Harmaec, P., Bisikalo, D. V., Boyarchuk, A. A., & Kuznetsov, O. A. 2002, A&A, 396, 937

Hoffman, J. L, Brown, J. C., Nordsieck K., St-Louis, N. & Wade, G. 2012, in AIP Conference Proceedings 1429, Stellar Polarimetry: From Birth to Death, eds. J.L. Hoffman, J. Bjorkman & B. Whitney (New York: AIP), 289

Jones, C. E., Molak, A., Sigut, T. A. A., de Koter, A., Lenorzer, A., Popa, S. C. 2009, MNRAS, 392, 383

Kurucz, R. F. 1993, Kurucz CD-ROM No. 13. Cambridge, Mass: Smithsonian Astrophysical Observatory

Lee, U., Osaki, Y., & Saio, H. 1991 MNRAS, 250, 432

Lucy, L. B. 1999, A&A, 344, 282

Millar, C. E., & Marlborough, J. M. 1998, ApJ, 494, 715

Millar, C. E., & Marlborough, J. M. 1999, ApJ, 516, 276

Millar, C. E., & Marlborough, J. M. 1999, ApJ, 526, 400

Natraj, V., Li, K., & Yung, Y.L. 2009, ApJ, 691, 1909

Owocki, S. 2006, in Stars with the B[e] Phenomenon, edited by M.Kraus, & A.S. Miroshnichenko, vol. 355 of Astronomical Society of the Pacific Conference Series, 219

Okazaki, A. T. 2001, PASJ, 53, 119

Poeckert, R., & Marlborough, J.M. 1978, ApJ, 220, 940

Poeckert, R., Bastien, P., & Landstreet, J.D. 1979, AJ, 84, 812

Porter, J. M. 1996, MNRAS, 280, L31

Porter, J. M., & Rivinius, T. 2003, PASP, 115, 1153

Quirrenbach, A., Bjorkman, K. S., Bjorkman, J. E., Hummel, C. A., Buscher, D. F., Armstrong, J. T., Mozurkewich, D., Elias, N. M. II, & Babler, B. L. 1997, ApJ, 479, 477

Rivinius, T., Baade, D., & Stefl, S. 2003, A&A, 411, 299

Sigut, T. A. A., & Jones, C. E. 2007, ApJ, 668, 481

Townsend, R. H. D., Owocki, S. P., & Howarth, I. D. 2004, MNRAS, 350, 189

Tycner, C., Jones, C. E., Sigut, T. A. A., Schmitt, H. R., Benson, J. A., Hutter, D. J., & Zavala, R. T. 2008, ApJ, 689, 461

Wisniewski, J. P., Draper, Z. H., Bjorkman, K. S., Meade, M. R., Bjorkman, J. E., & Kowalski, A. F. 2010, ApJ, 709, 1306

Wheelwright, H. E., Bjorkman, J. E., Oudmaijer, R. D., Carciofi, A. C., Bjorkman, K. S., & Porter, J. M. 2012, MNRAS, 423, 11

Wood, K., Bjorkman, J. E., Whitney, B. A., & Code, A. D. 1996, ApJ, 461, 828

Wood, K., Bjorkman, J. E., Whitney, B. A., & Code, A. D. 1996, ApJ, 461, 847

Wood, K., Bjorkman, K. S., & Bjorkman, J. E. 1997, ApJ, 477, 926

Yudin, R. V. 2001, A&A, 368, 912

Zellner, B. H. & Serkowski, K. 1972, PASP, 84, 619

Chapter 5

On the Intrinsic Continuum Linear Polarization of Classical Be Stars: The Effects of Metallicity and One-Armed Density Perturbations

A version of this chapter has been accepted for publication in The Astrophysical Journal Supplement by Halonen, R. J., & Jones, C. E. In this chapter, Halonen et al. 2013 refers to Chapter 3 and Halonen & Jones 2013 refers to Chapter 4 of this thesis.

5.1 Introduction

Classical Be stars are objects that exhibit, or have exhibited at some point in time, observational properties indicative of a Keplerian disk of ionized gas orbiting a non-supergiant star. These objects are characterized by features that arise from the interaction between the radiation emitted by the massive central star and the enveloping material, most prominent among which are an emission-line spectrum, an excess of continuum emission, and a linear polarization signature. While the steady-state viscous disk model (Lee et al., 1991; Okazaki, 2001) provides a good theoretical description of the geometrically-thin, Keplerian disk from which these features originate, the mechanisms through which the viscous disk is fed gas and angular momentum re-

main unidentified. Also unclear are the reasons for which particular B stars undergo the classical Be phenomenon while others do not. Almost certainly, the rapid rotation of these objects plays an important role in their development, but the accuracy of rotational velocity determinations is contentious (Townsend et al., 2004) and debate regarding the extent to which rotation can drive the formation of the decretion disks persists. Identifying the processes which may be responsible for producing tenable Keplerian decretion disks around rapidly-rotating B-type stars remains an intriguing challenge (for further discussion, see the review papers by Porter & Rivinius, 2003; Owocki, 2006).

Determining the origins of the classical Be phenomenon requires a reliable understanding of the physical and dynamical nature of the gaseous envelopes. While our current understanding is unsatisfactory in many regards, steady progress is being achieved through the detailed modelling of high-resolution observations using modern non-LTE radiative transfer codes, such as those described by Carciofi & Bjorkman (2006) and Sigut & Jones (2007). Beginning with our work in Halonen & Jones (2013), we have considered the modelling of the polarimetric properties of classical Be stars for tracing the evolution of the circumstellar gas. In this report, we supplement our previous investigation by considering two important disk properties which may have an appreciable effect on the computation of polarimetric observables. First, we investigate the effect of gas metallicity on the thermal solution of the modelled disk. As the gas temperature can profoundly affect the state of the scattering and absorptive opacities in the disk, it is essential to account for effects which may cause discernible changes to the computed solution. Second, we consider the implications of including non-axisymmetric density perturbations in the disk. Such perturbations alter the physical and geometric properties of the region in which electron scattering, the process responsible for the linear polarization signature in classical Be stars, occurs. For both the inclusion of gas metallicity and the addition of density perturbations, we determine how these modifications to the model affect the properties of the disk and, as a result, the predictions of the continuum linear polarization.

In this paper, we evaluate the importance of gas metallicity and non-axisymmetric density distributions in the computation of the continuum linear polarization signature from classical Be star models. While these two disk properties are unrelated in

most respects, understanding how each property affects the circumstellar gas is important when modelling and interpreting observables. For this reason, they are both key considerations in our ongoing analysis of the properties of the linearly polarized light observed in classical Be stars. We use the Monte Carlo calculation of the Stokes intensities described in Halonen et al. (2013) with the self-consistent thermal solution of the non-LTE radiative transfer code of Sigut & Jones (2007) to predict the polarimetric observables. We have organized the paper as follows: in Section 5.2, we briefly explain the computational procedures used in this investigation; in Section 5.3, we compare the polarimetric Balmer jump from classical Be stars with low- and solar-metallicity compositions; in Section 5.4, we consider the presence of one-armed density oscillations in the disk; lastly, in Section 5.5, we summarize the findings of this report.

5.2 Computational Method

We obtain the linear polarization for classical Be star models computed using the non-LTE radiative transfer code developed by Sigut & Jones (2007) and the Monte Carlo multiple-scattering treatment described in Halonen et al. (2013). The Sigut & Jones code solves the coupled problems of statistical and radiative equilibrium to produce a self-consistent calculation of the thermal structure of the circumstellar disk. The Monte Carlo procedure adopts the computed atomic level populations and gas temperatures as the underlying model of the circumstellar envelope and simulates the propagation of photons from the photoionizing radiation field of a star described by a Kurucz (1993) model atmosphere. Random sampling is used for determining the photon path lengths and scattering angles, and for resolving photon interactions with the gas. Combining the radiative equilibrium solution of the Sigut & Jones code with the Monte Carlo simulation provides an effective computational procedure for modelling circumstellar disks, such as those of classical Be stars, while employing realistic chemical compositions and self-consistent calculations of the thermal structure of the disk.

The density distribution of the circumstellar gas follows a simple power-law parameterization first prescribed to explain IR observations of Be stars (Waters, 1986;

Table 5.1: Stellar Parameters

Spectral Type	Radius ($R_\odot$)	Mass ($M_\odot$)	Luminosity ($L_\odot$)	$T_{\rm eff}$ (K)	$\log(g)$ ($\mathrm{cm\,s^{-2}}$)
B0V	7.40	17.5	3.98×10^4	3.00×10^4	3.9
B1V	6.42	13.2	1.45×10^4	2.54×10^4	3.9
B2V	5.33	9.11	4.76×10^3	2.08×10^4	3.9
B3V	4.80	7.60	2.58×10^3	1.88×10^4	4.0
B4V	4.32	6.62	1.33×10^3	1.68×10^4	4.0
B5V	3.90	5.90	7.28×10^2	1.52×10^4	4.0
B6V	3.56	5.17	4.31×10^2	1.38×10^4	4.0
B7V	3.28	4.45	2.28×10^2	1.24×10^4	4.1
B8V	3.00	3.80	1.36×10^2	1.14×10^4	4.1

Waters et al., 1987). The density of the gas at coordinates (R, Z), where R is the radial distance from the stellar rotation axis and Z is the distance above the midplane, is specified by

$$\rho(R, Z) = \rho_0 (R)^{-n} e^{-(\frac{Z}{H})^2}. \tag{5.1}$$

Here, ρ_0 fixes the density of the disk at the surface of the central star, n sets the exponential decline in density with increasing distance from the star, and H establishes the vertical scale height at each radial point using an initial value for the gas temperature, typically around 0.6 $T_{\rm eff}$. In this work, our disk models use 60 radial grid points extending from the stellar surface outward to 100 stellar radii. At each R, the gas is assumed to be in vertical hydrostatic equilibrium perpendicular to the plane of the disk. The models use 30 vertical grid points above and below the midplane. The Monte Carlo simulation extends the two-dimensional computational domain from the Sigut & Jones code into a three-dimensional model using 72 azimuthal grid points. While observational investigations have found that the value of n can range from 2.0 to 5.0, we use $n = 3.5$ which is the value predicted from isothermal viscosity (Porter, 1999). For the purposes of this work, we considered main sequence stars of spectral types B0 through B8. The stellar parameters used for each model are listed in Table 5.1.

The source of the intrinsic continuum polarization in classical Be stars is Thomson scattering (for example Coyne & Kruszewski, 1969; Zellner & Serkowski, 1972). When unpolarized light is scattered by free electrons, it becomes linearly polarized perpendicular to the plane containing the incident and scattered radiation. If the scattering

source is spherically symmetric on the plane of the sky, the distribution of polarizing planes is uniform, a complete cancellation of vibrations from orthogonal directions occurs and the net polarization is zero. Thus, axisymmetric disks, as an example, should exhibit zero net polarization when viewed pole-on. The projection of the disk on the plane of the sky is spherically asymmetric at any other viewing angle. The polarization level arising from electron scattering in the disk increases with inclination, peaking at around 75° (Halonen & Jones, 2013). At inclinations higher than 75°, the polarization level declines as the scattered light undergoes increased attenuation from HI absorption.

The Monte Carlo procedure determines the fraction of polarized light emerging from the modelled circumstellar environment by calculating the Stokes intensities, which are simply the sums or differences in intensity between components of the radiation field measured along the defining axes. The I parameter is the total intensity of the beam of light. The Q and U parameters, representing the linear polarization, are the differences in intensity between orthogonal directions of vibration, with one pair of orthogonal axes fixed at 45° from the other. As electron scattering produces no circularly polarized component, we ignore the V parameter and the normalized polarization level is expressed as:

$$p = (q^2 + u^2)^{1/2} \tag{5.2}$$

where $q = Q/I$ and $u = U/I$. In an axisymmetric disk, one of the linear polarization parameters is always zero if one defines the principal axes to coincide with the plane of the disk when viewed at 90°. Accounting for both linear polarization parameters becomes necessary when the density distribution in the disk is not axially symmetric.

5.3 Metallicity

The origin of the classical Be phenomenon may be intrinsically tied to the evolutionary characteristics of the stars that constitute this group. As such, the respective roles of metallicity and stellar age are important focuses for classical Be star research. Comparison studies of the fractional Be star populations of Milky Way (MW), Small Magel-

lanic Cloud (SMC) and Large Magellanic Cloud (LMC) clusters suggest that the prevalence of the Be phenomenon increases in lower metallicity environments (Maeder et al., 1999). This result carries important implications for the nature of classical Be stars as metallicity may have a dominant effect on the fraction of stars that attain critical rotation (Maeder & Meynet, 2001). The evolutionary age of Be stars remains somewhat unsettled due to the conflicting suggestions that (1) the phenomenon occurs largely in the latter half of the main sequence (Fabregat & Torrejón, 2000) and (2) the phenomenon is present throughout the entire main sequence (Mathew et al., 2008; Wisniewski & Bjorkman, 2006). Presenting perhaps the most compelling research on the issue to date, Wisniewski et al. (2007b)'s investigation Be stars in the LMC and SMC suggests that classical Be stars are present in young stellar clusters with an enhanced fraction in older clusters. Of significance, the authors point out that two-colour photometry, the method commonly used to study evolutionary age and metallicity in the Be phenomenon, cannot reliably discern between classical Be stars and other B-type Hα emitters. They refine the classical Be identification process through the use of these objects' distinct linear polarization signature characterized by the wavelength-dependent imprint of neutral hydrogen absorption.

In this section, we evaluate the importance of metallicity in computing the thermal structure of Be star disks and the effect of metallicity-induced temperature differences on the predicted polarimetric Balmer jump. In light of Wisniewski et al. (2007b)'s finding that the frequency of polarimetric Balmer jumps is smaller in low metallicity environments, we address the possibility that this is due to the inherent temperature discrepancies between disks in different metallicity environments, as reported by Ahmed & Sigut (2012).

5.3.1 Results and Discussion

We began by computing two sets of models using identical mass density distributions and different gas compositions. One set of models used a pure hydrogen composition while the second set included nine elements (H, He, C, N, O, Mg, Si, Ca and Fe) and assumed solar abundances. The details of the atomic models implemented in the radiative equilibrium calculation and the exact chemical abundances adopted are given

in Sigut & Jones (2007). The comparison of these two sets of models provide us with a reasonable gauge to the effect of including heating and cooling from metal processes in the determination of the thermal structure of the disk. We evaluate the global disk temperature using a density-weighted temperature defined as:

$$\langle T_\rho \rangle = \frac{1}{M_{disk}} \int T(R,Z)\rho(R,Z)dV_{disk}, \tag{5.3}$$

where M_{disk} is the total mass of the disk. We find that the density-weighted temperature does not differ appreciably between the two sets, as shown in Table 5.2. This is consistent with the findings of Jones et al. (2004) who reported very small differences between the self-consistent density-weighted temperatures of pure hydrogen and solar Fe abundance disks for models of the classical Be stars γ Cas and 1 Del. Sigut & Jones (2007) noted that the absorption of ionizing radiation by elements heavier than hydrogen offsets some of the line cooling, arising mainly from FeII, in higher density disks. Figure 5.1 shows the density-weighted temperature of the gas as a function of radial distance for three stars. We note that the gas temperatures in all the sets are very similar within the first six stellar radii of the disk, the region of the disk where the polarimetric Balmer jump forms (Halonen & Jones, 2013). While the temperatures differ somewhat more in the inner part of the disk for the models where $\rho_0 = 6.25 \times 10^{-12}$ g cm^{-3}, the density of the disk in this model yields insufficient absorption for producing a Balmer jump in the polarization spectrum. From these temperature comparisons, we do not expect there to be significant differences in the polarimetric properties caused by the inclusion of metallicity in the radiative equilibrium computation.

A consequence of the fixed-density scheme is that the hydrogen populations differ between the compared sets of models. As such, the relevant opacities that govern the linear polarization signature, the electron scattering opacity and the HI absorptive opacity, are affected by this difference when computing the underlying models. The general result is that the opacities are lower in the solar metallicity model, as demonstrated in Figure 5.1. Plainly, this effect arises from the choice of using the same mass density for both sets of models: the solar metallicity model includes less hydrogen and has fewer free electrons available for scattering. With this important consideration in mind, we examine how the Balmer jump changes due to this sim-

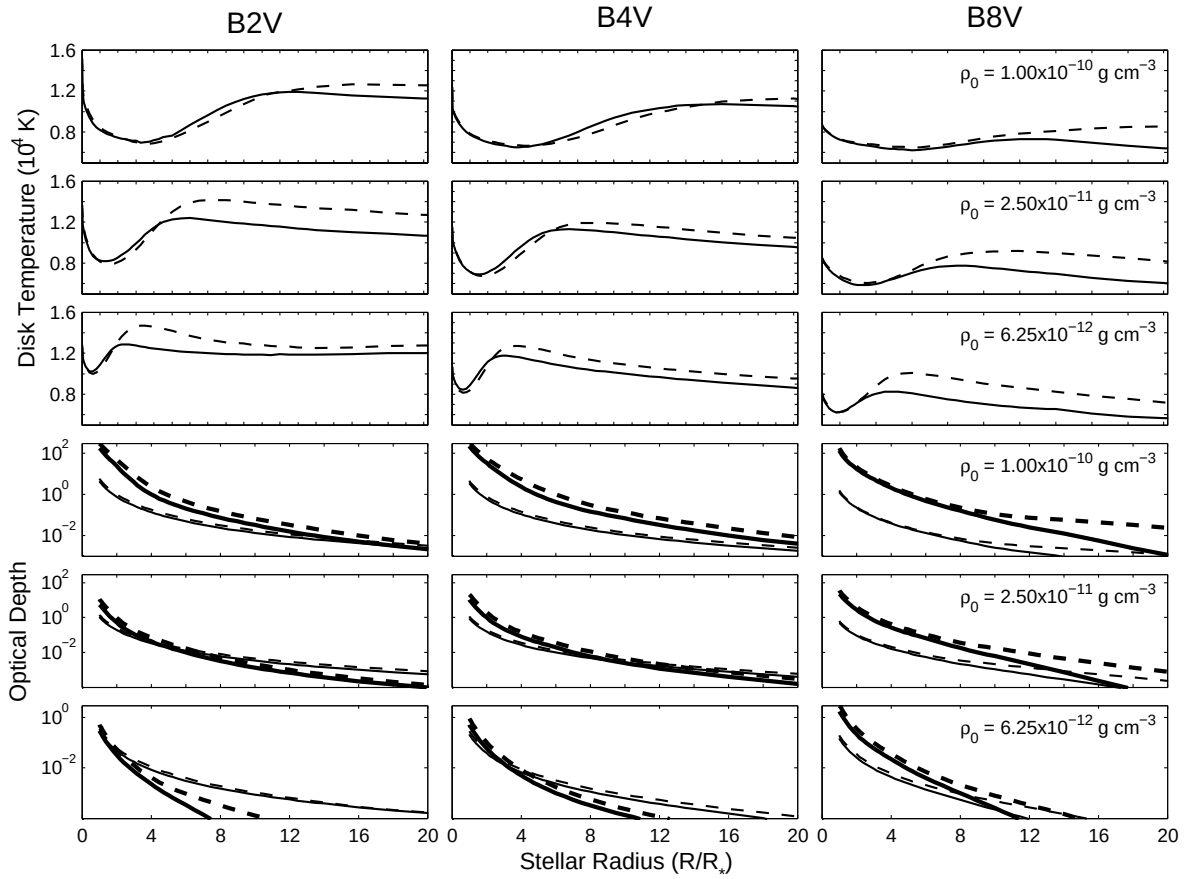

Figure 5.1: Disk temperature and optical depth comparison of circumstellar disks with $n = 3.5$ and $\rho_0 = 1.0 \times 10^{-10}$ g cm^{-3} (top frame), $\rho_0 = 2.5 \times 10^{-11}$ g cm^{-3} (middle frame), $\rho_0 = 6.25 \times 10^{-12}$ g cm^{-3} (bottom frame). The models on the left are disks surrounding a B2V star, those in the center are disks surrounding a B4V star, and those on the right are disks surrounding a B8V star. The dashed lines represent a pure hydrogen composition and the solid lines represent a solar chemical composition. In the bottom frames, the thick lines show the optical depth from hydrogen absorption just shortward of the Balmer jump, while the thin lines show the optical depth from electron scattering.

Table 5.2: Density-Weighted Disk Temperatures

ρ_0	6.25×10^{-12} g cm^{-3}	2.50×10^{-11} g cm^{-3}	1.00×10^{-10} g cm^{-3}
B2V			
Hydrogen	1.22 $\times 10^4$ K	1.09 $\times 10^4$ K	9.49 $\times 10^3$ K
Solar	1.16 $\times 10^4$ K	1.04 $\times 10^4$ K	9.29 $\times 10^3$ K
B4V			
Hydrogen	9.51 $\times 10^3$ K	9.00 $\times 10^3$ K	8.61 $\times 10^3$ K
Solar	9.00 $\times 10^3$ K	8.60 $\times 10^3$ K	8.28 $\times 10^3$ K
B8V			
Hydrogen	7.47 $\times 10^3$ K	7.25 $\times 10^3$ K	7.20 $\times 10^3$ K
Solar	6.84 $\times 10^3$ K	6.68 $\times 10^3$ K	6.60 $\times 10^3$ K

ple but important difference in the models. Figure 5.2 shows the polarization Balmer jump for both sets. The higher opacities in the hydrogen-only models contribute to systemically higher Balmer jumps. Clearly, caution must be taken in the modelling of polarimetric features: a hydrogen-only composition in the disk, as is often employed, can overestimate the amount of electron scattering and HI absorption in the disk.

In another set of models, we fixed the hydrogen number density and performed the same comparison as above. Again, the global disk temperature between the solar-metallicity and pure hydrogen models did not differ significantly close to the star and hence there were no appreciable differences in the scattering and hydrogen absorptive opacities. The Balmer jumps between the two models were nearly identical as illustrated in Figure 5.3. Given sufficient density for the characteristic hydrogen absorption signature to be discernible ($\rho_0 \gtrsim 1.0 \times 10^{-11}$ g cm^{-3} for $n = 3.5$), the polarimetric Balmer jump reflects primarily the amount of neutral hydrogen absorption occurring in the disk. As we have shown, in densities above this threshold, the presence of metal-line cooling in the disk does not sufficiently affect the thermal structure to produce an observable change in the Balmer jump.

Of course, other considerations may produce temperature differences between disks in environments with different metallicities. Using the same non-LTE radiative transfer code to solve for the radiative equilibrium solution as is used in this work, Ahmed & Sigut (2012) showed that disks in the SMC (Z_{SMC} = 0.002) are systemati-

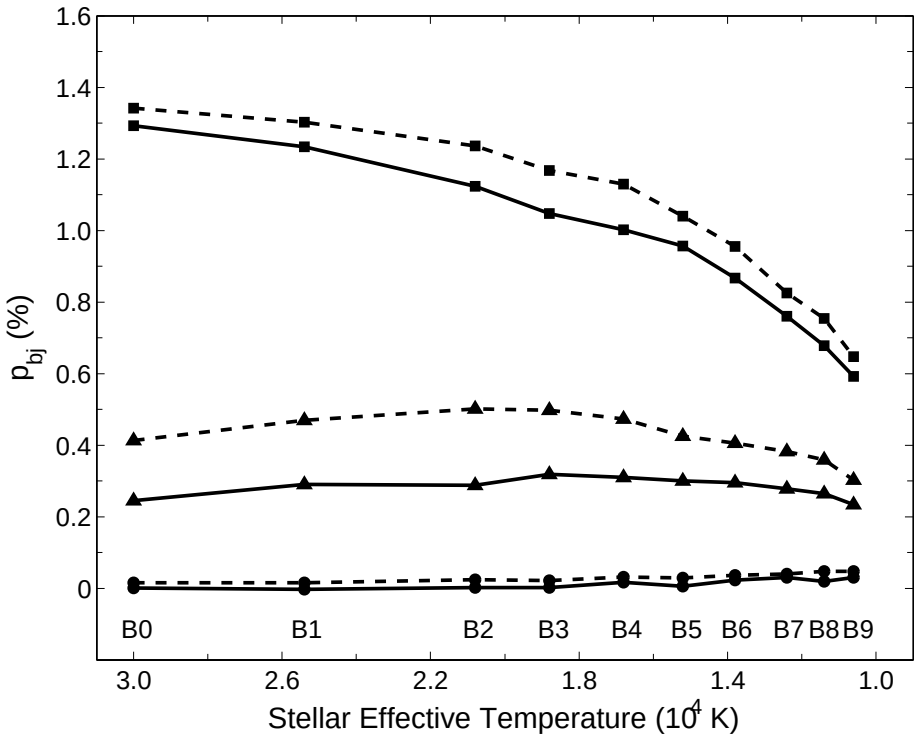

Figure 5.2: Polarimetric Balmer jump for stars surrounded by circumstellar disks of gas while keeping mass density fixed in models using a pure hydrogen composition (dashed lines) and solar composition (solid lines). The disk density distributions have $n = 3.5$ and $\rho_0 = 1.0 \times 10^{-10}$ g cm^{-3} (squares), $\rho_0 = 2.5 \times 10^{-11}$ g cm^{-3} (triangles), and $\rho_0 = 6.25 \times 10^{-12}$ g cm^{-3} (circles). The system is viewed at an inclination of i = 75°.

cally hotter than disks in the MW (Z_{MW} = 0.02). In their work, the authors accounted for the intrinsic difference in the effective temperatures of spectral types between MW and SMC populations (Trundle et al., 2007). As such, they adopted $T_{\rm eff}$'s for SMC stars that were typically a few thousand degrees higher than the $T_{\rm eff}$'s used for MW stars. In the context of this investigation, we examined the extent to which the intrinsic difference in the $T_{\rm eff}$ could affect the polarimetric Balmer jump. Figure 5.4 shows the Balmer jumps for B2V and B5V stars with varying stellar $T_{\rm eff}$ in models computed using the same disk density distribution. In general, the height of the polarimetric Balmer jump decreases with increasing $T_{\rm eff}$ as the gas temperature in the disk increases and the absorptive opacity decreases. However, the changes in the Balmer jump are relatively small. For the optically thinner model, the largest decrease in the Balmer jump over a 2000 K increase in $T_{\rm eff}$ is roughly 10 %. In the optically thicker model, there was almost no change in the height of the Balmer jump over the same increase in $T_{\rm eff}$. While the

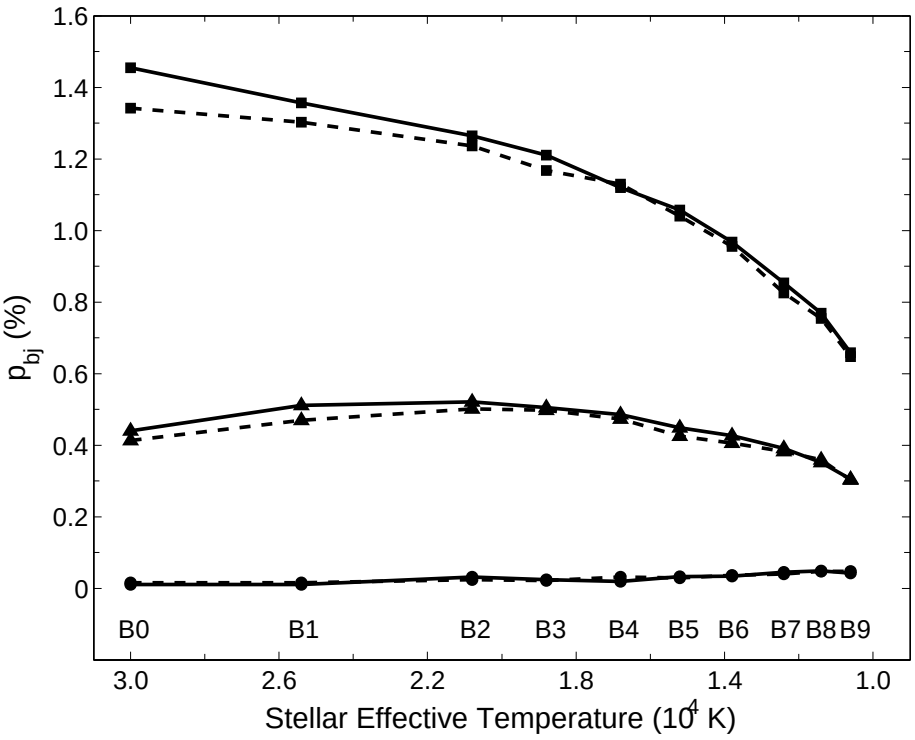

Figure 5.3: Polarimetric Balmer jumps for stars surrounded by circumstellar disks of gas while keeping hydrogen number density fixed in models using a pure hydrogen composition (dashed lines) and solar composition (solid lines). The disk density distributions have $n = 3.5$ and $\rho_0 = 1.0 \times 10^{-10}$ g cm^{-3} (squares), $\rho_0 = 2.5 \times 10^{-11}$ g cm^{-3} (triangles), and $\rho_0 = 6.25 \times 10^{-12}$ g cm^{-3} (circles). The mass densities of the solar composition models are adjusted to the fixed hydrogen number density. The system is viewed at an inclination of $75°$.

circumstellar disks around stars in low-metallicity environments are hotter, the resulting decrease in the HI absorptive opacity does not seem to be sufficient to cause an appreciable difference in the computed Balmer jump.

5.4 Non-axisymmetric Disk Density Perturbations

The outward flow of gas and angular momentum in a Keplerian disk is well-described by viscous transport (Lee et al., 1991; Papaloizou et al., 1992; Okazaki, 2001). This theoretical description of the gas dynamics adheres well to the observed kinematic properties of the disks of classical Be stars (Carciofi, 2011). Additionally, the viscous disk model accommodates the existence of non-axisymmetric distributions of gas arising in the form of one-armed oscillations (Okazaki, 1991). These density waves qualitatively

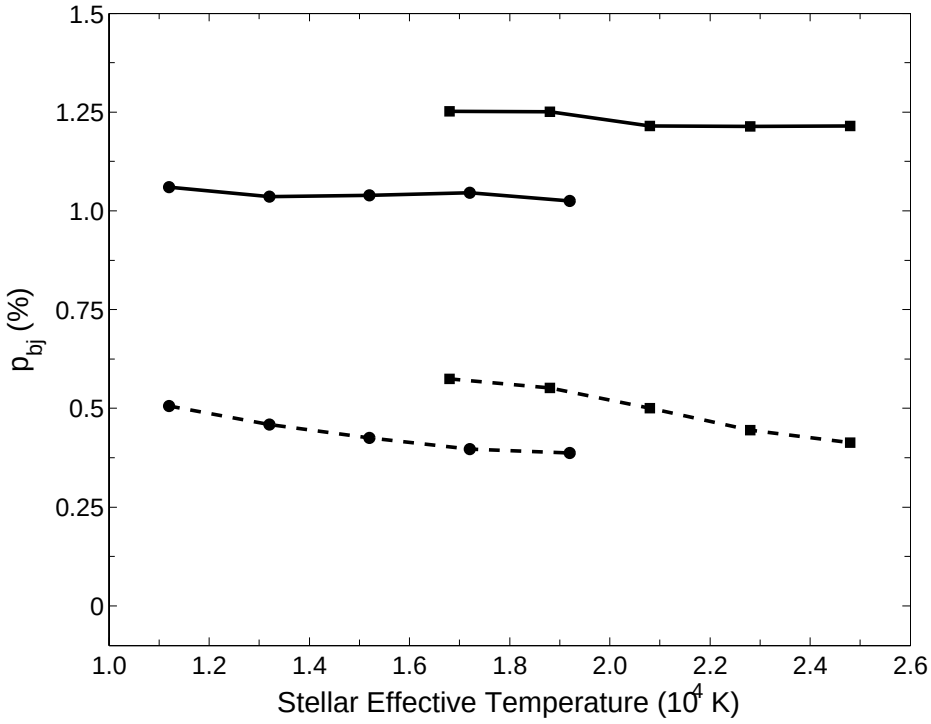

Figure 5.4: Polarimetric Balmer jumps for stars using the B2V (squares) and B5V (circles) stellar parameters and varying $T_{\rm eff}$. The disk density distributions are parametrized by $n = 3.5$ and $\rho_0 = 2.5 \times 10^{-11}$ g cm^{-3} (dashed lines) or $\rho_0 = 1.0 \times 10^{-10}$ g cm^{-3} (solid lines) and the systems are viewed at an inclination of 75°.

explain a frequently observed characteristic of classical Be stars: non-equal intensities in the components of double-peaked emission lines (Hanuschik et al., 1995; Okazaki, 1997). These asymmetries in line profile morphologies are commonly referred to as the V/R (violet-to-red) variability. The perturbation pattern in the disk comprises overdense and underdense regions of gas which produce emission excesses and deficits at wavelengths shifted by the motion of the gas with respect to the observer. As the wave precesses about the central star, the overdense and underdense regions oscillate from approaching to receding and the excess and deficit in line emission fluctuate about center of the line, producing cyclical V/R variations. The one-armed oscillation paradigm is consistent with observed timescales of periodic V/R variability in classical Be stars, which exist on timescales of a couple of years to ten years (Okazaki, 1997). Interferometric observations (Vakili et al., 1998; Berio et al., 1999) have yielded evidence of one-armed oscillations precessing in the prograde direction in the several classical Be stars.

One peculiarity is the occasional discrepancy in the V/R ratio of different emission lines observed contemporaneously. While most V/R asymmetric lines in a spectrum possess the same orientation, there have been reports of phase differences (Slettebak, 1982; Baade, 1985) and even complete V/R reversals (Clark & Steele, 2000). Wisniewski et al. (2007a) suggested that this phenomenon can be explained by the presence of a one-armed oscillation possessing a spiral-like shape and the knowledge that the physical sizes of line forming regions vary for different lines. Therefore, attributing some degree of helicity to the perturbation pattern, line forming regions of different radial extents may possess very different azimuthal morphologies. In a detailed modelling of the classical Be star ζ Tau, Carciofi et al. (2009) employed a global one-armed oscillation model with a spiral perturbation pattern to successfully reproduce the phase differences in V/R variable Hα and Brγ lines. Their result lends support to the idea that the one-armed oscillation pattern in the disks of classical Be stars may take on a spiral structure.

In this section, we evaluate the effect of global one-armed oscillations on the continuous linear polarization spectrum. As the distribution of the scattering material relative to the observer is fundamental to the measured polarization, properly accounting for non-axisymmetric distributions of gas may be important for attempting to derive physical properties from polarimetric observations of classical Be stars. Recall that the contribution to the polarization level from points that are separated azimuthally by 180° is equivalent. Hence, in the single-scattering limit where no absorption occurs, the polarization level remains unaffected by antisymmetric changes to the density distribution. However, when further effects are taken into consideration, such as stellar occultation, multiple-scattering and absorption/re-emission, the result will be variations in the polarization level.

5.4.1 Results and Discussion

We computed models that include global one-armed oscillations in the gas density distribution of the circumstellar disk. These models were constructed by applying a perturbation to the density distribution given by Equation 5.1. The thermal solution was calculated using the Sigut & Jones code for 36 azimuthal angles in equal intervals

from 0 to 2π. The computed atomic level populations and gas temperatures were then integrated to produce a steady-state three-dimensional model of the disk for which the Stokes parameters were then calculated using the Monte Carlo procedure. In the models presented here, the one-armed oscillation is confined to a region extending out to 10 stellar radii from the central star. We emphasize that the models presented in this section are *ad hoc*: our purpose is to represent plainly the geometric implications of the density waves such that they can characterize non-axisymmetric disks from a polarimetric perspective.

We present results for the pair of global oscillation models illustrated in Figure 5.5. The first perturbation pattern, shown in the top row of Figure 5.5 and hereafter referred to as the *simple oscillation model*, is characterized by diametrically-opposed overdense and underdense regions similar to the pattern given in Okazaki (1997). The second perturbation pattern, shown in the bottom row of Figure 5.5 and hereafter referred to as the *spiral oscillation model*, is characterized by a spiral shape similar to the pattern employed in Carciofi et al. (2009). The second and third columns of Figure 5.5 depict the gas density in the equatorial plane and the density-weighted gas temperature, respectively. The last column illustrates the change in gas temperature induced by the presence of the perturbation in the disk relative to an unperturbed model of equal average density. It is important to understand how the inclusion of the perturbation affects the gas density and temperature of the disk. Regions of enhanced or reduced density can affect the conditions for generating the polarization signature in multiple ways. Overdense regions in the disk can increase local opacities and shield parts of the disk to create cool regions of gas where absorption is elevated and scattering is reduced, while underdense regions can decrease local opacities to the point where neither absorption or scattering have an appreciable effect.

We introduce a phase parameter ϕ_p to express the azimuthal angle at which the system is being observed with respect to the perturbation pattern in the disk. We arbitrarily set $\phi_p = 0$ to coincide with the maximum amplitude in the perturbation pattern, and increase ϕ_p in the counter-clockwise direction. The minimum amplitude coincides with $\phi_p = \pi$ as the perturbations are antisymmetric. The ρ/ρ_0 patterns depicted in Figure 5.5 are consistent with those presented by Okazaki (1997) and Carciofi et al. (2009) which seem reasonably constrained by observations. The models possess the equiva-

lent mass of an unperturbed disk with density parameters $n = 3.5$ and $\rho_0 = 5.0 \times 10^{-11}$ g cm^{-3}. The models discussed were computed with a hydrogen-only composition; we computed the spiral model using a solar composition and found that the temperature structure did not differ appreciably.

Figure 5.6 shows the V-band polarization levels for the two disk oscillation models and provides a comparison to the polarization level of an unperturbed disk. The average polarization level of the perturbed disk is lower than the polarization level of the unperturbed disk, except for when the disk is viewed at an inclination that is close to pole-on (i.e. $i \lesssim 30^\circ$). For near edge-on disks, the variation in the continuum polarization level can exceed 20% of the average value in the simple oscillation model. In this model, the polarization minima occur at $\phi_p = pi/2$ and $3\pi/2$. Thus, the minimum polarization is produced by the disk when the axis along which the density maximum and minimum are situated is orthogonal to the observer's line-of-sight. As the disk is symmetric about this axis, the polarization level is equivalent at both phases. The polarization maxima occur at $\phi_p = 0$ (or 2π) and π. The most polarization is produced when the axis along which the density distribution is unperturbed is orthogonal to the observer's line-of-sight. At the phases where this occurs, the observer's line-of-sight can pass through either the overdense region (at $\phi_p = 0$) or the underdense region (at $\phi_p = \pi$). The difference between the polarization level at the two maxima exists because of the combined effects of absorption and stellar occultation of the disk. For the spiral oscillation model, the variation in the continuum polarization level is smaller owing to the more intricate configuration of the underdense and overdense regions.

Figures 5.7 and 5.8 show the Balmer jumps for the two disk oscillation models. Predictably, the Balmer jumps in the simple oscillation model follow the same variation pattern as the V-band polarization. For the spiral oscillation pattern, the maxima in the Balmer jump are out of phase with the V-band polarization maxima by about $\pi/4$. Of course, this is reflective of the fact that these two polarimetric features arise from different regions of the disk, thus resulting in different azimuthal morphologies at different phases. The Balmer jump arises from a smaller region within 6 R_*, while the V-band polarization arises from a larger region of the disk, out to about 10 R_* (Carciofi, 2011; Halonen & Jones, 2013). Plotting the Balmer jump against the V-band polarization in what is referred to as a BJV diagram (Draper et al., 2011), the phase

differences between the polarimetric features in the two oscillation models are clearly illustrated. While the simple oscillation model sketches straight lines on a BJV plot, the spiral oscillation model traces out discernible loops. We note that for prograde precession of the one-armed oscillation in the disk, the loops will proceed in a clockwise direction in the BJV diagram.

The physical implications of BJV loops in the context of disk growth and dissipation were considered in Halonen & Jones (2013). When the disk is undergoing such a transition, the BJV loop traces changes to the absorptive opacity and the number of scatterers owing to the addition or removal of gas in the disk. In the case of a precessing, spiral-like density wave, the loop in the BJV diagram appears because of geometric changes to the morphology of the scattering region. Despite the difference in the two scenarios, the principal interpretation of the loop given in Halonen & Jones (2013) is unchanged: a steeper slope in the BJV diagram reflects changes in the absorption imprint whereas a flatter slope reflects changes to the unattenuated polarization level. These changes affect the polarized light that is directed towards the observer as opposed to the total polarized light being produced by the disk, which remains unchanged. Given this explanation, cyclic variations in the polarimetric features owing to one-armed oscillations should provide crucial insight into the structure of the inner disk. We note that while the polarization variation arising from disk growth and dissipation and from a precessing density perturbation are qualitatively similar when plotted in a BJV diagram, the polarization angle varies only for the latter case in which the azimuthal morphology of the scattering medium changes as the perturbation precesses. The polarization angle remains constant during the formation and dissipation of the disk assuming symmetric addition and removal of gas. Thus, the two phenomenon will be discernible when the polarization is plotted in qu space, for example.

5.5 Summary

The Balmer jump is an emblematic feature of the polarization signature of classical Be stars and is an important tool for differentiating these objects from similar B-type emission stars. Understanding how this feature behaves is crucial for using it effec-

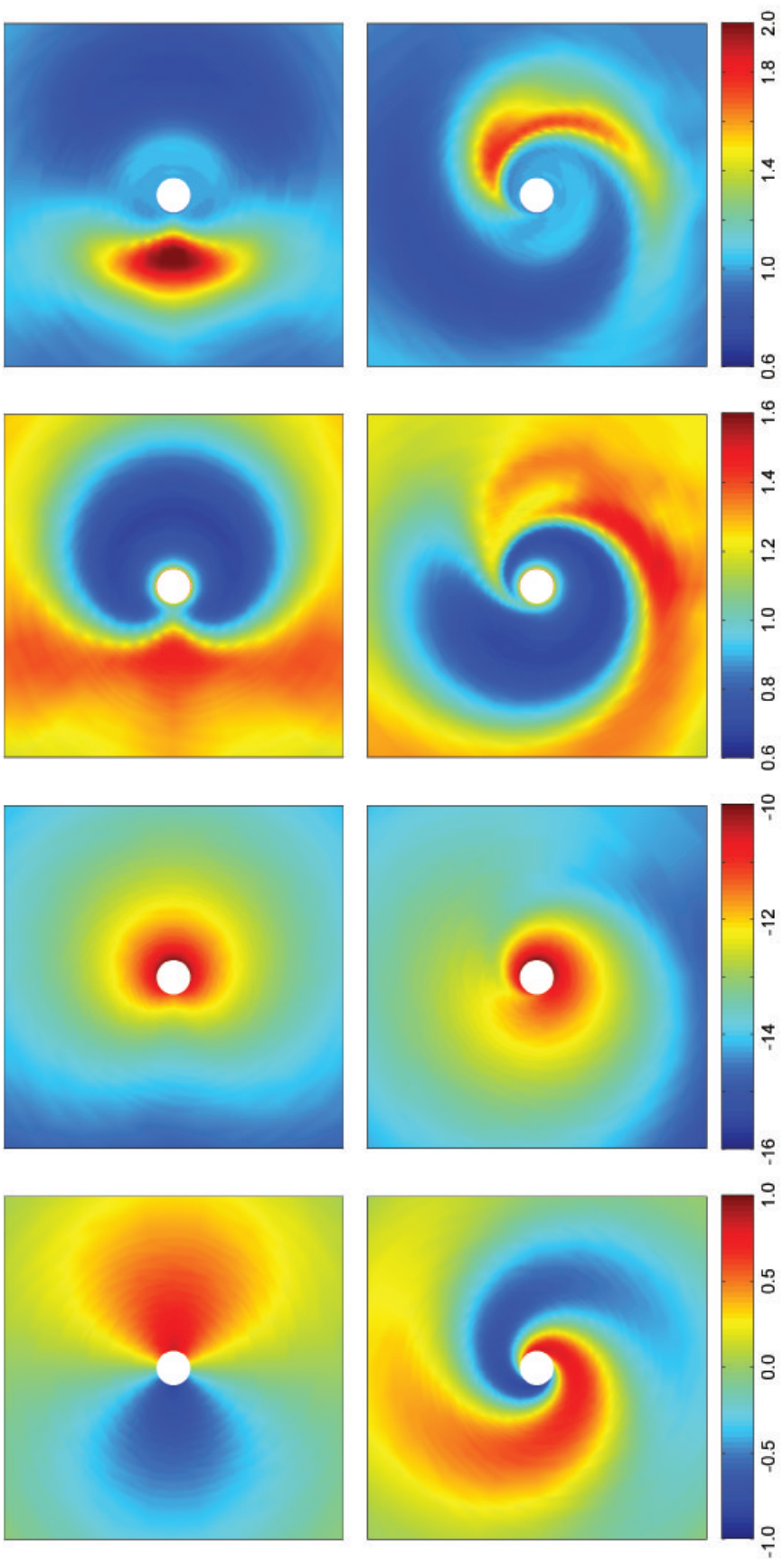

Figure 5.5: Properties of the models of one-armed oscillations in the circumstellar disk surrounding a B2V star. The disk density distribution is parametrized by $n = 3.5$ and $\rho_0 = 5.0 \times 10^{-11}$ g cm^{-3}. The squares are 20 by 20 stellar radii. First column (leftmost): density perturbation pattern ρ/ρ_0. Second column: equatorial logarithmic density distribution in the disk (g cm^{-3}). Third column: density-weighted gas temperature (10^4 K). Fourth column: ratio of the density-weighted gas temperature of the perturbed disk to that of a disk with an unperturbed density distribution.

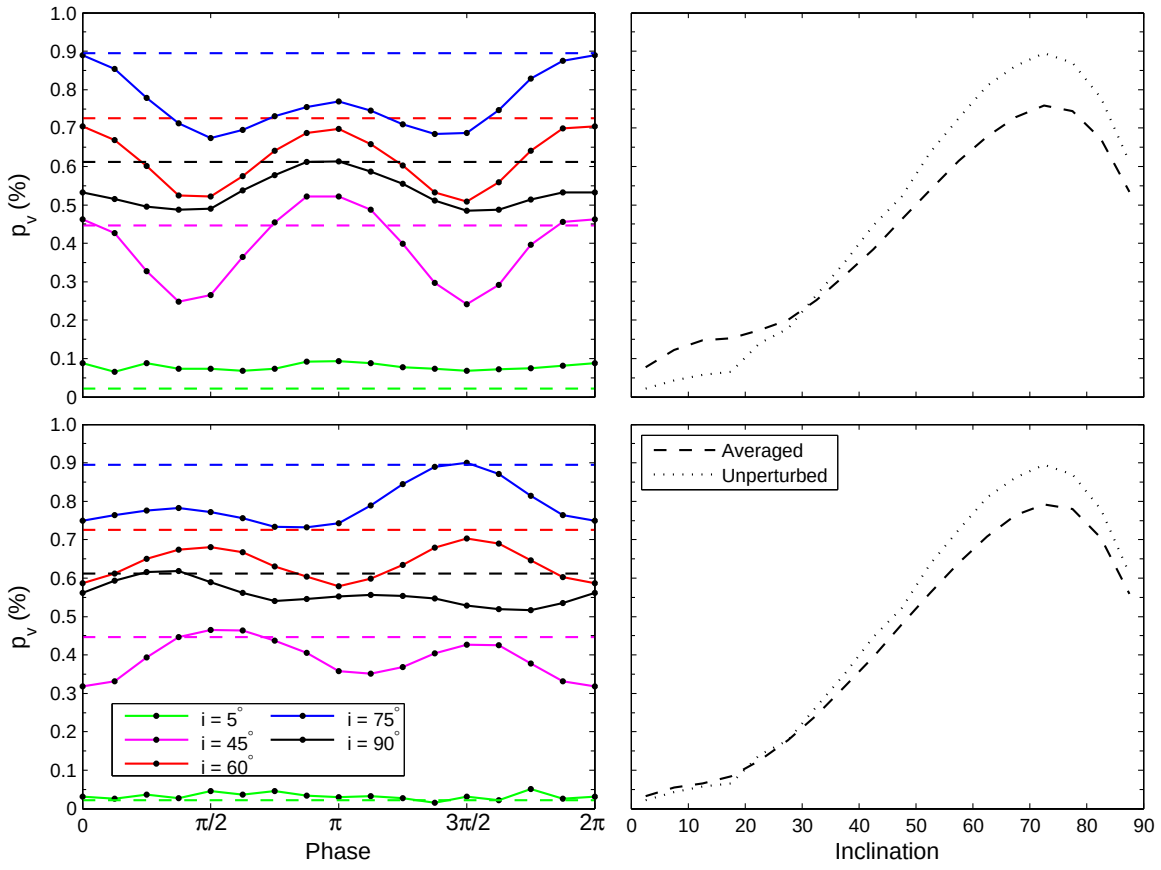

Figure 5.6: Left: variation in the V-band polarization level with changing phase for the simple oscillation model (top) and the spiral oscillation model (bottom). The solid lines show the fraction of linearly polarized light from the perturbed disk for the system viewed at inclination, plotted from top to bottom, $75°$(blue), $60°$(red), $90°$(black), and $45°$(magenta) and $0°$(green). The dashed lines show the V-band polarization level from unperturbed disk with the same density distribution. Right: average V-band polarization level for the perturbed disk and V-band polarization from an unperturbed disk with the same density distribution.

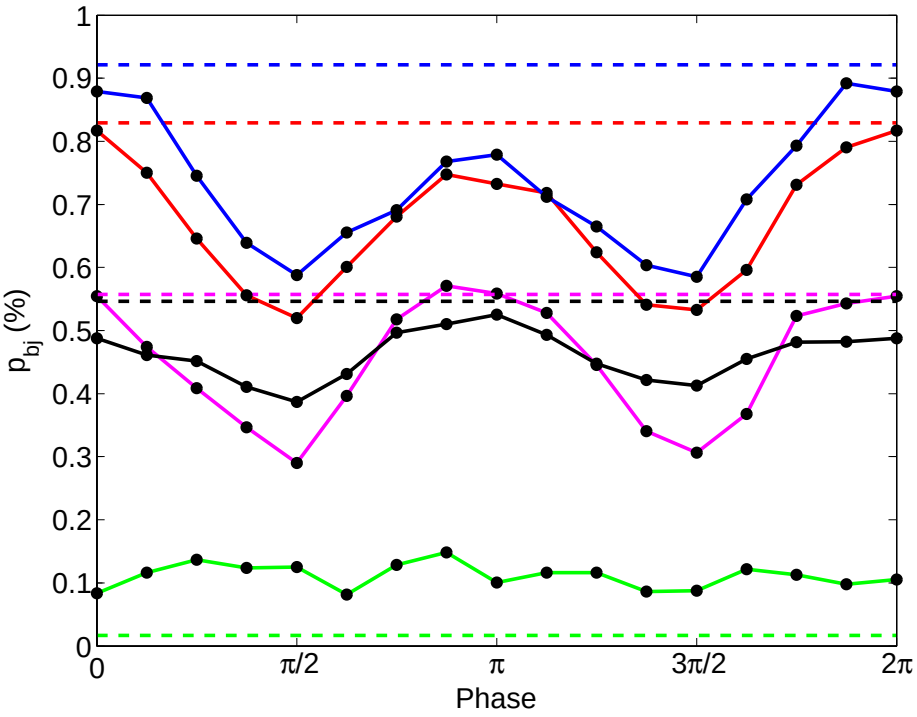

Figure 5.7: Variation in the V-band polarization with changing phase for the simple oscillation model. The solid lines show the fraction of linearly polarized light from the perturbed disk for the system viewed at inclination, plotted from top to bottom, $75°$(blue), $60°$(red), $45°$(magenta), and $90°$(black) and $0°$(green). The dashed lines show the V-band polarization level from unperturbed disk with the same density distribution.

tively in the study of classical Be stars. We have attempted to ascertain any inherent differences in the polarimetric Balmer jump due to the chemical properties of the system. Wisniewski et al. (2007b) proposed that an observed lower frequency of polarization Balmer jumps in low-metallicity environments could be explained by higher disk temperatures. Significant differences in the temperature of the circumstellar gas can affect the electron scattering and HI absorptive opacities. However, we find that the temperature differences owing to the presence of metals in the disk and to the intrinsic differences in the stellar $T_{\rm eff}$ cannot account for systemically lower Balmer jumps in low-metallicity environments. Wisniewski et al. also suggest that it might be harder to form massive disk systems in low metallicity environments. While we cannot address this point directly, we do point out that classical Be star disks do require sufficient density to produce a detectable wavelength-dependence from the hydrogen absorption signature. Thus, classical Be stars in low-metallicity environments may

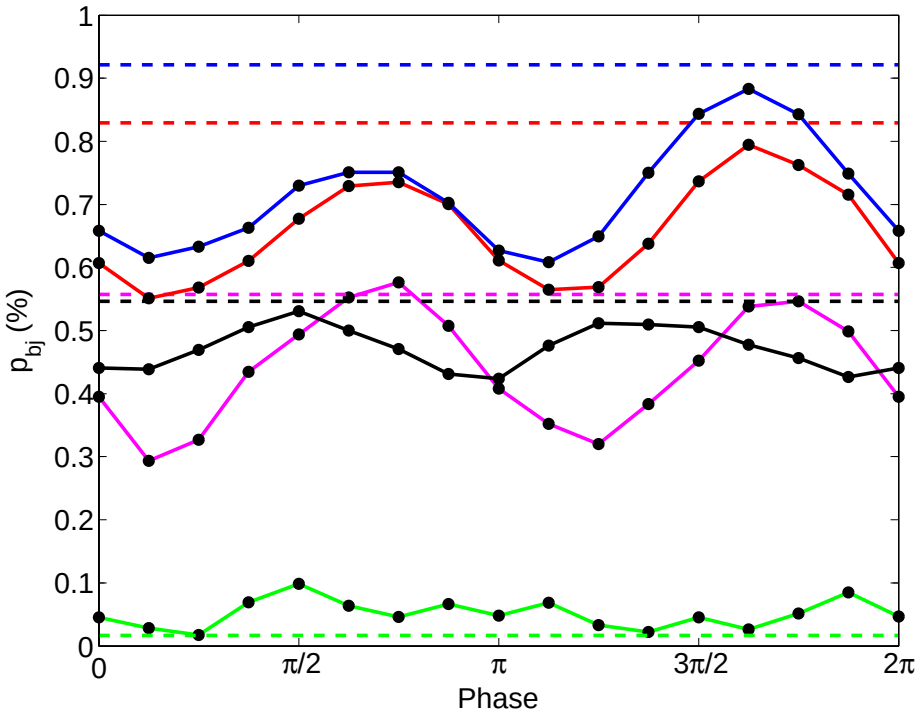

Figure 5.8: Variation in the V-band polarization with changing phase for the spiral oscillation model. The solid lines show the fraction of linearly polarized light from the perturbed disk for the system viewed at inclination, plotted from top to bottom, $75°$(blue), $60°$(red), $45°$(magenta), and $90°$(black) and $0°$(green). The dashed lines show the V-band polarization level from unperturbed disk with the same density distribution.

simply form optically thinner disks than their metal-rich counterparts, thus yielding detectable line emission while exhibiting a linear polarization signature largely unaffected by neutral hydrogen absorption. Clearly, further observations and further study are required to verify and explain the finding of Wisniewski et al.

We also investigated the variability that can occur in the linear polarization signature of classical Be star if the density distribution of the circumstellar gas is not axisymmetric. We have illustrated the qualitative periodic behaviour that we might expect to observe if a one-armed density wave is present in the disk. In particular, polarimetric features originating from different formation regions in the disk could provide key details for mapping the part of the disk close to the star. Few observational programs (McDavid et al., 2000; Carciofi et al., 2009) have investigated possible polarimetric variability in classical Be stars and any correlation it may have to other periodic features whose origins are well-explained by one-armed oscillations. As of

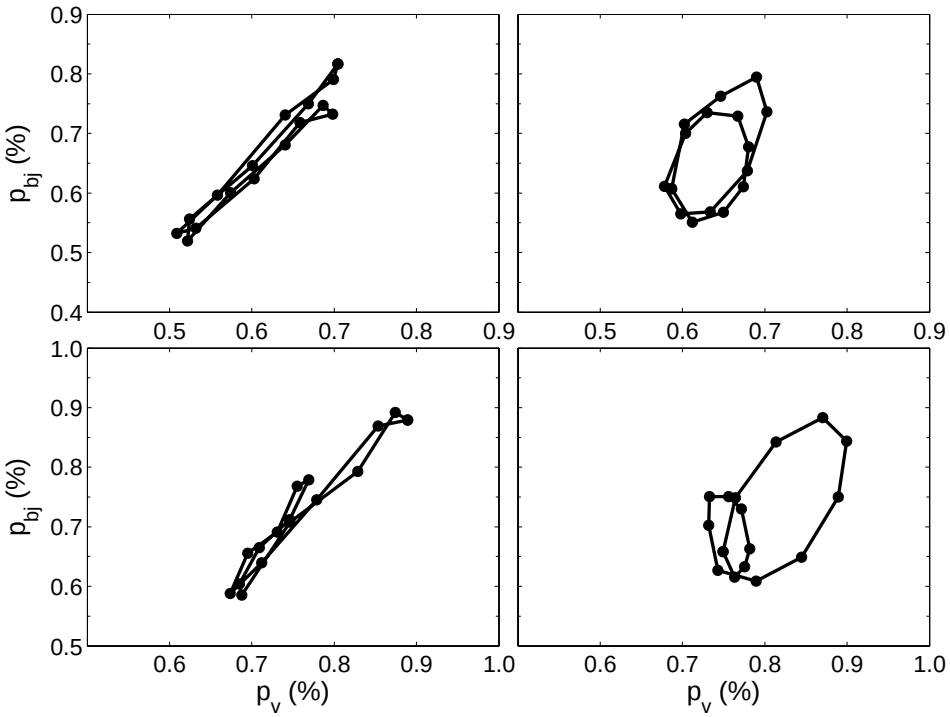

Figure 5.9: Balmer Jump vs. V-band polarization (BJV) diagrams for the disk global oscillation models. The plots on the left show the BJV diagrams for the simple oscillation model while the plots on the right show the BJV diagrams for the spiral oscillation model. The plots on top are for the system viewed at inclination 60° while those on the bottom are viewed at inclination 75°.

yet, no such polarimetric periodicity in classical Be stars has been rigorously demonstrated. It is possible, as Carciofi et al. suggest, that the global oscillation model is a poor predictor of the inner disk geometry, or that mass outbursts that feed the disk disrupt the geometric structure of the inner disk. However, the potential insight that can be gained from variability in the continuum linear polarization signature of classical Be stars suggests further observational study is worthwhile. Good temporal resolution of the polarimetric features paired with reliable hydrodynamical models of one-armed oscillations may be instrumental for determining the geometric nature of the inner region of the circumstellar disks.

Bibliography

Ahmed, A., & Sigut, T. A. A. 2012, ApJ, 744, 191

Baade, D. 1985, A&A, 148, 59

Berio, P., et al. 1999, A&A, 345, 203

Carciofi, A. C., & Bjorkman, J. E. 2006, ApJ, 639, 1081

Carciofi, A. C., Okazaki, A. T., le Bouquin, J.-B., Stefl, S., Rivinius, Th., Baade, D., Bjorkman, J. E., & Hummel, C. A. 2009, A&A, 504, 915

Carciofi, A. C. 2011, in IAU Symp. 272, Active OB Stars: Structure, Evolution, Mass Loss, and Critical Limits, ed. C. Neiner et al. (Cambridge: Cambridge Univ. Press), 325

Clark, J. S., & Steele, I. A., 2000, A&AS, 141, 65

Cox, A.N. 2000, Allen's Astrophysical Quantities, (4th ed.; New York: Springer)

Coyne, G.V., & Kruszewski, A. 1969, AJ, 74, 528

Draper, Z.H., Wisniewski, J.P., Bjorkman, K.S., Haubois, X., Carciofi, A.C., Bjorkman, J.E., Meade, M.R., & Okazaki, A. 2011, ApJ, 728, 40

Fabregat, J., & Torrejón, J. M. 2000, A&A, 357, 451

Halonen, R. J., Mackay, F. E., & Jones, C. E. 2013, ApJS, 204, 11

Halonen, R. J., & Jones, C. E. 2013, ApJ, 765, 17

Hanuschik, R. W., Hummel, W., Dietle, O., & Sutorius, E. 1995, A&A, 300, 163

Jones, C. E., Sigut, T. A. A., & Marlborough, J. M. 2004, MNRAS, 352, 841

Kurucz, R. F. 1993, Kurucz CD-ROM No. 13. Cambridge, Mass: Smithsonian Astrophysical Observatory

Lee, U., Osaki, Y., & Saio, H. 1991 MNRAS, 250, 432

Maeder A., & Meynet, G. 2001, A&A, 373, 555

Maeder, A., Grebel, E. K., & Mermilliod, J.-C. 1999, A&A, 346, 559

Mathew, B., Subramaniam, A., & Bhatt, B. C. 2008, MNRAS, 388, 1879

McDavid, D., Bjorkman, K. S., Bjorkman, J. E. & Okazaki, A. T. 2000, in IAU Coll. 175, The Be Phenomenon in Early-Type Stars, ed. Smith, M. A., Henrichs, H. F., & Fabregat, J. (San Francisco: ASP), 460

Okazaki, A. T. 1991, PASJ, 43, 75

Okazaki, A. T. 1997, A&A, 318, 548

Okazaki, A. T. 2001, PASJ, 53, 119

Owocki, S. P. 2006, in Stars with the B[e] Phenomenon, ed. M. Kraus, & A.S. Miroshnichenko, vol. 355 of Astronomical Society of the Pacific Conference Series, 219

Papaloizou, J. C., Savonije, G. J., & Henrichs, H. F. 1992, A&A, 265, 45

Porter, J. M. 1999, A&A, 348, 512

Porter, J. M. & Rivinius, T. 2003, PASP, 115, 1153

Sigut, T. A. A., & Jones, C. E. 2007, ApJ, 668, 481

Slettebak, A. 1982, ApJS, 50, 55

Townsend, R. H. D., Owocki, S. P., & Howarth, I. D. 2004, MNRAS, 350, 189

Trundle, C., Dufton, P. L., Hunter, I., et al. 2007, A&A, 471, 625

Waters, L. B. F. M. 1986, A&A, 162, 121

Waters, L. B. F. M., Coté, J., & Lamers, H. J. G. L. M. 1987, A&A, 185, 206

Wisniewski, J.P. & Bjorkman, K. S. 2006, ApJ, 652, 458

Wisniewski, J. P., Bjorkman, K. S., Magalhaes, A. M., Bjorkman, J. E., Meade, M. R., Pereyra, A. 2007, ApJ, 671, 2040

Wisniewski, J. P., Kowalski, A. F., Bjorkman, K. S., Bjorkman, J. E., Carciofi, A. C. 2007, ApJ, 656, 21

Vakili, F., Mourard, D., Stee, P. H., et al. 1998, A&A, 335, 261

Zellner, B. H. & Serkowski, K. 1972, PASP, 84, 619

Chapter 6

Conclusions

6.1 Introduction

When we committed ourselves to studying the intrinsic linear polarization of classical Be stars, we were motivated by the tantalizing notion of using polarimetry to explore the dynamical nature of their circumstellar envelopes. Because the polarization originates directly from the scattering of light in the gaseous circumstellar environment, analysis of its variability over time can potentially provide crucial insight into the evolution of the scattering material. The initial plan for this thesis was conceived with the primary goal of acquiring a greater physical understanding of the continuum linear polarization signature that characterizes these intriguing objects. Moreover, we aspired to increase the visibility of polarization in the field of classical Be star research and to provide a computational tool capable of interpreting polarimetric observations. We achieved our objectives for this project with the successful development of a procedure for computing the Stokes intensities from models of classical Be stars and subsequent detailed analysis of the properties of the continuous polarimetric spectra predicted from our computational simulations. In accomplishing these goals, we have established the groundwork for conducting further research which may prove to be pivotal in refining our understanding of classical Be stars.

We begin this closing chapter by reiterating the salient findings from the three scientific publications that have arisen from this project to date. Next, we discuss our future priorities for this ongoing research project and we enumerate the major forth-

coming improvements to our Monte Carlo radiative transfer code. Finally, we conclude this thesis with some final remarks on the key accomplishments of our work.

6.2 Summary

The foundation of this project was the development of a computational radiative transfer code, MCTRACE, that simulates the propagation of photons through the circumstellar environment using Monte Carlo techniques. Complemented by a non-LTE radiative transfer code which supplies the thermal structure and atomic populations of the gas in the disk, our procedure calculates the Stokes intensities for models of classical Be stars. We employed our radiative transfer procedure to investigate in detail the continuum linear polarization signature of these objects.

In Chapter 3, we assessed the effects of several improvements on Poeckert & Marlborough's (1978a) single-scattering plus attenuation technique for calculating the intrinsic polarization levels of classical Be stars. We found that improvements to the sampling of the disk density and the inclusion of a self-consistent calculation of the thermal structure for the gas in the disk yield polarization levels that differ from the levels expected by Poeckert & Marlborough. In addition, we evaluated the importance of including multiple-scattering in calculating the Stokes intensities and predicting the continuum linear polarization in classical Be stars. Our Monte Carlo procedure naturally allows for multiple scatterings of photons as they propagate through the circumstellar environment. We confirmed that accounting for multiple-scattering is crucial for correctly predicting the fraction of linearly polarized light emerging from the optically thick gaseous disks and that predictions from single-scattering approaches must be viewed with caution.

In Chapter 4, we investigated the intrinsic continuum linear polarization from axisymmetric density distributions of gas surrounding classical Be stars during the formation and dissipation of their circumstellar disks. In particular, we emphasized the utility of polarimetric measurements as diagnostics for modelling the evolution of these systems. By showing that the principal features of the polarimetric spectrum originate from different regions of the disk, we highlighted the capability of spectropolarimetric observations to trace physical changes in the disk on critical scales.

We developed models that approximated disk formation and dissipation in representative fashion and illustrated how the polarimetric properties of these systems can have a pivotal role in characterizing global changes in the distribution of gas in the circumstellar disk. This work represents a strong argument for assiduous polarimetric monitoring of active classical Be star systems.

In Chapter 5, we reported on the effects of a pair of disk properties on the continuum linear polarization signature of classical Be stars. First, we investigated the effect of including metallicity in computing the thermal structure of the circumstellar gas on the resulting polarimetric Balmer jump. We found that, despite hotter average disk temperatures in low-metallicity environments, the temperature change alone cannot account for large differences in the Balmer jumps between low-metallicity and solar-metallicity stellar populations. Second, we investigated the effect of including a global one-armed oscillation in the gas density distribution of the modelled disk. We found that a non-axisymmetric perturbation pattern yields discernible variations in the predicted polarization level which can help characterize the dynamical nature of the gas near the star.

6.3 Future Directions

We have made important progress in enhancing our understanding of the polarimetric signature of classical Be stars and its diagnostic potential for investigating the physical and dynamical nature of these objects. In the wake of this thesis, we envision several extensions to this work which we believe will have further important scientific impact. In the following paragraphs, we outline four of the key priorities for the future of this research project.

1. *The observation and modelling of classical Be stars with polarimetry.*

   One of our initial goals for this project was to provide our research group, as well as the research community in general, with a computational code capable of predicting the polarimetric features of classical Be stars. With our Monte Carlo code ready and available for use, we are tasked with spearheading an observing campaign dedicated to obtaining high temporal resolution polarimetric

measurements of specific classical Be stars, ideally those that exhibit photometric variability indicative of disk formation and dissipation or spectroscopic V/R variability indicative of a global disk oscillation. Using polarimetric observations, we can study the dynamical properties of the disks on a physical scale that is difficult to achieve with other observing techniques.

2. *The study of the spectropolarimetric line profiles of classical Be stars.*

   Until now, our primary focus has been investigating the continuous polarimetric features of classical Be stars. However, the depolarizing effect of bound-bound transitions on the polarimetric spectrum may also yield important diagnostics of disk properties (for example Poeckert & Marlborough, 1977, 1978a,b). The spectropolarimetric line profiles of classical Be stars have not been studied with modern radiative transfer codes. We are planning to make the necessary modifications to our Monte Carlo radiative transfer code to account for the effect of bound-bound transitions on the continuum and to compute the spectropolarimetric line profiles. This important addition will enable us to further probe the physical conditions of the disk through the modelling observational data from high-resolution spectropolarimetry,

3. *The use of hydrodynamical computational models.*

   The use of hydrodynamical calculations can provide a more sophisticated approach for analyzing the observable effects that arise owing to disk growth and dissipation or precessing, one-armed oscillations. At present, the coupling of radiative transfer calculations with smoothed particle hydrodynamics code works well for modelling radiation hydrodynamics (for example Acreman et al., 2010). We intend to combine smoothed particle hydrodynamic simulations for the circumstellar gas (for example Okazaki et al., 2002) with our radiative transfer codes to model the temporal evolution of classical Be star disks and predict the observable characteristics of different dynamical scenarios.

4. *The improvement of the Monte Carlo radiative transfer code.*

   We are motivated to increase the robustness of our Monte Carlo radiative transfer code and improve on particular simplifying assumptions made during its

development. Along with the inclusion of bound-bound transitions, there are a number of extensions to MCTRACE that we are planning to implement. We enumerate some of the anticipated additions to our code:

- *Gravitational Darkening* — We will include the effect of gravitational darkening in the photoionizing radiation field of the central star. Accounting for the effects of gravitational darkening in rapidly-rotating stars is important for correctly computing the thermal structure of the circumstellar disks of classical Be stars and making accurate predictions of their observational properties (McGill et al., 2011, 2013).
- *Interferometric Polarimetry* — We can adapt the work of Mackay et al. (2009) to MCTRACE to predict the Stokes visibility amplitudes. The use of interferometric polarimetry to study extended circumstellar environments is a novel approach that has the potential to provide significant insight regarding the nature of objects like classical Be stars.
- *Photon Peeling* — We will improve the efficiency of the Monte Carlo method with the implementation of a photon peeling scheme (for example Yusef-Zadeh et al., 1984), which should accelerate the convergence of the Stokes intensities.
- *Dust Scattering* — We will expand the code to compute the Stokes intensities that arise from circumstellar environments in which electron scattering is not the only polarigenic mechanism. In particular, we can easily modify the scattering matrix to account for the scattering of photons off of dust particles. This will allow us to model the circumstellar environments of other celestial objects such as Herbig Ae/Be stars.

6.4 Final Remarks

A scientific white paper on stellar polarimetry submitted to the 2010 Astronomy and Astrophysics Decadal Survey stated the following:

> "The field of stellar polarimetry is currently driven by observation. Rapid advances in numerical modeling techniques are necessary to enable a full

> understanding of the data and make predictions that can be tested with future observations." (Hoffman et al., 2009)

With recent advances in observing techniques (see proceedings from the 2011 workshop on stellar polarimetry Hoffman et al., 2012), sophisticated computational tools are needed to take advantage of the potential scientific insight that can be gained from modelling high-resolution polarimetric observations. In the case of classical Be stars, there are presently few non-LTE radiative transfer codes capable of producing realistic models of the circumstellar disks that are readily available for interpreting the data obtained from spectropolarimetry. In our view, this is a pressing issue that is limiting our efforts to attain the detailed description of the circumstellar environment required to address the deficiencies in our understanding of the dynamical nature of classical Be stars.

We have endeavoured to address the shortage of sophisticated computational modelling tools. With the introduction and the continuing development of our Monte Carlo radiative transfer code, we are providing the community a tool which is capable of producing testable predictions and interpreting observations. We hope that the availability of our code will encourage astronomers to dedicate increased time and effort to probing classical Be stars with polarimetry.

In this thesis, we demonstrated how the distinct linear polarization signature produced from the scattering and absorption of light in the circumstellar envelopes of classical Be stars can be used to study these intriguing objects. Our investigation focused on a desire to improve our understanding of the physical conditions in which the characteristic polarimetric features arise. Furthermore, we showed how the polarized light can be a diagnostic of the changing physical properties of an evolving disk. As the mechanism(s) leading to disk formation remains unidentified, we contend that our work represents a compelling argument for the polarimetric monitoring of classical Be stars on a range of timescales. At the very least, we hope that our work will inspire an enhanced appreciation for the diagnostic potential of the linear polarization signature for investigating the circumstellar environments of classical Be stars and for studying astrophysical phenomena in general.

Bibliography

Acreman, D. M., Harries, T. J., & Rundle, D. A. 2010, MNRAS, 402, 1143

Hoffman, J. L. et al. 2009, White Paper to the Stars and Stellar Evolution Science Frontiers Panel of the Astro2010 Decadal Survey

Hoffman, J. L, Bjorkman, J. & Whitney, B. 2012, Stellar Polarimetry: From Birth to Death, (New York: AIP)

Mackay, F. E., Elias, N. M., Jones, C.E., & Sigut, T.A.A. 2009, ApJ, 704, 591

McGill, M. A., Sigut, T. A. A. & Jones, C. E. 2011, ApJ, 743, 111

McGill, M. A., Sigut, T. A. A. & Jones, C. E. 2013, ApJS, 204, 2

Poeckert, R., & Marlborough, J.M. 1977, ApJ, 218, 220

Poeckert, R., & Marlborough, J.M. 1978, ApJ, 220, 940

Poeckert, R., & Marlborough, J.M. 1978, ApJS, 38, 229

Okazaki, A. T., Bate, M. R., Ogilvie, G. I., & Pringle, J. E. 2002, MNRAS, 337, 967

Yusef-Zadeh, F., Morris, M., & White, R. L. 1984, ApJ, 278, 186

Curriculum Vitae

Name:	Robbie J. Halonen
Post-Secondary Education and Degrees:	The University of Western Ontario London, Ontario 2008 - 2013 Ph.D. Astronomy
	The University of Western Ontario London, Ontario 2007 - 2008 M.Sc. Astronomy
	The University of Western Ontario London, Ontario 2003 - 2007 B.Sc. Honours Specialization in Astrophysics
Honours and Awards:	William H. Wehlau Award 2010
	NSERC Alexander Graham Bell Canada Graduate Scholarship (CGS D) 2008-2011
	NSERC Alexander Graham Bell Canada Graduate Scholarship (CGS M) 2007-2008
	Ontario Graduate Scholarship (declined) 2007, 2009
	Maude Holt Kingston Gold Medal in Astronomy 2007
	NSERC Undergraduate Student Research Award 2005, 2006, 2007

Related Work Experience:

Teaching Assistant
The University of Western Ontario
2007 - 2012

Research Assistant
The University of Western Ontario
2007 - 2013

Summer Research Assistant
Laurentian University
2005, 2006

Publications:

Refereed Publications

Halonen, R. J. & Jones, C. E. *On the Intrinsic Continuum Linear Polarization of Classical Be Stars: The Effects of Metallicity and One-Armed Density Perturbations*, 2013, ApJS, accepted

Halonen, R. J. & Jones, C. E. *On the Intrinsic Continuum Linear Polarization of Classical Be Stars during Disk Growth and Dissipation*, 2013, ApJ, 765, 17

Halonen, R. J., Mackay, F. E., & Jones, C. E. *Computing the Continuum Polarization from Thomson Scattering in Gaseous Circumstellar Disks*, 2013, ApJS, 204, 11

Halonen, R. J., Jones, C. E., Sigut, T. A. A., Zavala, R. T., Tycner, C.. Levine, S. E., Luginbuhl, C. B., Vlieg, N., & Vrba, F. J. *Infrared Excess in the Be Star δ Scorpii*, 2008, PASP, 120, 498

Conference Proceedings

Halonen, R. J., & Jones, C. E. *Probing the Circumstellar Disk Structure of Be Stars with Polarimetry*, 2012, in Circumstellar Disks at High Resolution, ed. A. Carciofi and Th. Rivinius, ASPC, 464, 125 (Contributed talk)

Halonen, R. J., & Jones, C. E. *The Polarization Signature from Circumstellar Disks*, 2011, in Stellar Polarimetry: From Birth to Death, ed. J. L. Hoffman, J. Bjorkman and B. Whitney, AIPC, 1429, 263 (Poster presentation)

Halonen, R. J., Mackay, F. E., Jones, C. E., & Sigut, T. A. A. *Investigating the Continuum Linear Polarization of Be Stars*, 2011, in Active OB Stars: Structure, Evolution, Mass Loss and Critical Limits, ed. C. Neiner, G. Wade, G. Meynet and G. Peters, IAUS, 272, 394 (Poster presentation)

Halonen, R. J., Jones, C. E., & Sigut, T. A. A. *Studying the Physical Conditions in Be Star Disks Using non-LTE Radiative Transfer Codes*, 2010, in The Interferometric View on Hot Stars, ed. Th. Rivinius and M. Curé, RMxAC, 38, 85 (Contributed talk)

Further Contributions

Halonen, R. J., & Jones, C. E. *The Polarization Signature from Multiple Scattering in Classical Be Stars*, 2011, Canadian Astronomical Society AGM, London, Ontario (Poster presentation)

Jones, C. E., Mackay, F. E., Elias, N. M. & **Halonen, R. J.** *Full-Stokes Interferometric Polarimetry: New Insights for Classical Be Stars*, 2011, Canadian Astronomical Society AGM, London, Ontario (Poster presentation)

Halonen, R. J., Jones, C. E., & Sigut, T. A. A. *Using Non-LTE Radiative Transfer to Model Classical Be Stars*, 2009, Colloquium at Hokkaido University, Sapporo, Japan (Oral presentation)

Halonen, R. J., Jones, C. E., Sigut, T. A. A. & Carciofi, A. C. *Exploring the Physical Conditions in Be Star Disks Using Different Computational Techniques*, 2009, Canadian Astronomical Society AGM, Toronto, Ontario (Poster presentation)

McGill, M., **Halonen, R. J.**, Jones, C. E., & Sigut, T. A. A. *Modeling the Hydrogen Infrared Lines of the Be Star Gamma Cassiopeia*, 2007, Canadian Astronomical Society AGM, Kingston, Ontario (Poster presentation)